Modelling progressive failure of good quality to massive rock masses

By

Hossein Rafiei Renani

A thesis submitted in partial fulfillment of the requirements for the degree of

Doctor of Philosophy

in

GEOTECHNICAL ENGINEERING

Department of Civil and Environmental Engineering
University of Alberta

Abstract

The behavior of excavations in rock masses with different degrees of fracturing can be fundamentally different, yet commonly used constitutive models and failure criteria assume similar failure mechanisms and strength relationships. This work was dedicated to evaluating current methods and developing improved approaches to modelling the behavior of good quality to massive rock masses with Geological Strength Index (GSI) greater than 60. Starting with the simplest case of intact rock, the well-established Hoek-Brown criterion was compared with the recently proposed Christensen criterion. Results of triaxial compression, triaxial extension, and polyaxial compression tests on different rock types were used for quantitative comparison. It was shown that while the Christensen criterion has several attractive characteristics and has been successfully applied to other materials, on average it leads to 65% higher errors compared to Hoek-Brown criterion when applied to intact rock due to mathematical limitations on the slope of failure envelope.

The behavior of a good quality rock mass with GSI≈60 was examined using the measured displacements around a deep shaft. While a single three-dimensional numerical model could not accurately match the readings of all extensometers, the results of using strain softening material with empirically estimated parameters gave a reasonable match to measurements of two extensometers. Higher readings of the third extensometers could be reproduced with a weaker model which provided a possible range of in situ parameters. A two-dimensional model with longitudinal displacement profile was also used for back analysis. While this model gave apparently better overall match to measurements of all extensometers, it was shown to be the result of compromising three-dimensional effects

around an advancing face. It was also shown that longitudinal displacements profile may not adequately capture three-dimensional effects in an anisotropic in situ stress fields.

The progressive failure of brittle rocks was studied using the results of damage-controlled tests on samples of granite and limestone under triaxial compression. It was confirmed that increasing damage causes degradation of cohesion and mobilization of friction. Furthermore, while cohesion degradation appears independent of confining stress, mobilized friction angle is reduced at higher confinements. Theoretical Cohesion-Weakening Friction-Strengthening (CWFS) models were proposed capturing the progressive failure in the laboratory and in situ. The proposed model closely matched the laboratory stress-strain curves. The model also predicted the in situ behavior of four tunnels in a massive rock mass with GSI≈100. It was shown that the proposed model eliminated the problematic characteristics of the current CWFS model. General guidelines were given for estimating the parameters of the proposed CWFS model for practical applications.

The data base of observed pillar behavior in hard rock mines was used to validate the developed modelling approach. The documented behavior of 85 pillars in two mines was used to examine the accuracy of the proposed model for rock masses with GSI≈80. It was shown that the model could separate stable pillars from unstable/failed pillars. While pillars with width-to-height ratio, W/H<2 showed peak strength at relatively low strains and subsequent strain softening behavior, wider pillars could continue to sustain increased stresses at higher strains. The model also captured the observed mechanism of pillar failure in situ starting from minor spalling to slabbing, formation of hour glass shaped pillars and final shear failure. It was shown that current perfectly-plastic and strain softening models can significantly overestimate the strength of deep pillars while empirical strength formulas systematically underestimate the strength of wide pillars.

Acknowledgements

This thesis would not have been possible without the contributions of so many people who inspired and supported me through different stages of life. My deepest gratitude goes to my family who gave me their unconditional love and support.

I would like to thank my supervisor, Dr. Derek Martin, for his vote of confidence. I feel deeply privileged to be among those who completed their research under his supervision. Through hours of deep discussions, he gave me a new perspective on rock mechanics. He presented me with real challenges and gave me the freedom to look for answers and when I could not go any farther, he was an incredible source of new ideas to help me break through scientific obstacles.

I also wish to express my gratitude to the following individuals:

- Dr. Evert Hoek for his support and contributions to our research on failure criteria.
- Dr. David Potyondy for many discussions on frontiers of discontinuum models.
- Mr. Richard Hudson for his contributions to our back analysis program.

Finally, I would like to thank Atomic Energy Limited Canada (AECL) for carrying out innovative tests and providing data which continues to enhance our understanding of rock behavior. Financial support of the Natural Sciences and Engineering Research Council of Canada (NSERC), the Canadian Nuclear Waste Management Organization (NWMO), and the Swedish Nuclear Fuel and Waste Management Company (SKB) is also greatly appreciated.

Table of Contents

List of Tables

List of Figures

Chapter 1

Introduction

Design of safe and functional structures such as tunnels, slopes, dams, and underground storage facilities requires knowledge of strength of the material in which they are constructed. Since the inception of rock mechanics as a new discipline in 1960's, determination of rock mass strength has been the primary focus of researchers in this field. Despite all the efforts and contribution made since then, accurate prediction of rock mass strength remains one of the most challenging tasks for rock engineers. It may be surprising to outsiders why this seemingly simple problem has not been completely solved by now. After all, estimating the strength of other materials frequently encountered in engineering design such as steel and concrete is quite straightforward.

The behavior of rock masses is more complex than other engineering materials for two main reasons. First, the basic component of rock mass, intact rock has a more complex microstructure than a manufactured material such as steel for example. Geometrical and mechanical heterogeneity of intact rock microstructure manifests itself by a complex macroscopic mechanism of failure. The second source of complex behavior is the existence of discontinuities with various lengths and directions within the rock mass. These structural features not only affect the overall strength of rock mass but also contribute to local discontinuous deformations.

Over the past few decades, numerous laboratory and in situ tests have been carried out on rocks to study the process of deformation and failure under different loading conditions. Subsequently, material models have been proposed to capture the observed behavior. Such models can then be used in analytical or numerical analyses to predict the behavior of rock engineering structures.

The Hoek-Brown criterion is perhaps the most commonly used model for rock masses. This criterion can be used to determine the strength of rock mass with varying degrees of fracturing. The first step in using the model is to use laboratory test results for intact rock to determine the parameters for intact rock. The next step is to quantify rock mass quality using the Geological Strength Index, GSI which ranges from zero for a completely disintegrated rock mass to 100 for a fracture free rock mass. The value of GSI is finally used in a series of empirical equations to determine the extent by which rock mass fractures degrade the strength of intact rock.

1.1.   Problem statement

While the current approach to estimating rock mass strength using Hoek-Brown criterion can theoretically be used for all rock masses with GSI from zero to 100, it has shown to be more reliable and accurate when applied to average quality rock masses where interlocking between angular blocks of rock governs rock mass strength. The behavior of poor quality rock masses with GSI lower than about 30 may be better captured using classical soil mechanics concepts and Mohr-Coulomb model. The strength of massive sparsely fractured rock masses with GSI higher than about 90 can also be better studies using brittle failure models.

This thesis is focused on modelling the behavior of good quality to massive rock masses with GSI greater than 60. It aims at detailed evaluation of existing modelling approaches used for such rock masses. It involves addressing a wide range of questions such as:

- Are the commonly used material models theoretically plausible when applied to the simplest case of intact rock under uniaxial and triaxial stresses?
- Are the existing intact rock models in close agreement with the results of laboratory tests?
- To what extent current models can capture the in situ behavior of rock masses with different levels of fracturing?
- How is it possible to eliminate the deficiencies of current methods and develop improved modelling approaches with enhanced theoretical basis and accuracy?

1.2.   Finding a solution

The basic prerequisite of a reliable rock mass model is to accurately capture the behaviour of the ideal rock mass with no fractures, i.e., intact rock. The results of uniaxial, triaxial and polyaxial tests on laboratory specimens of intact rock can be used for evaluation of different strength criteria. The results of tests on four different rock types under different loading conditions were used to examine the commonly used Hoek-Brown criterion as well as a more recent criterion proposed by Christensen (1997) as a comprehensive model for all materials. The results of quantitative comparisons between the two criteria were further investigated analytically to provide a clear and conclusive picture of the fundamental characteristics of each strength criterion.

The next step in this study was evaluating the current modeling approaches when applied to in situ behavior of average quality rock masses. The results of displacement measurements around a deep circular shaft excavated in a rock mass with GSI of 62 were used for back analysis. Two and three dimensional analyses using perfectly-plastic and strain softening models were carried out to predict the displacements and zone of failure around the shaft. The parameters and results obtained from current empirical modeling approaches and back analysis were compared. The merits of using a two dimensional model along with

longitudinal displacement profiles to capture three dimensional effects around an advancing excavation were also studied.

While the results of standard laboratory tests and in situ measurements provide invaluable information about the behavior of intact rock and rock mass, they provide little if any information about the relationship between damage increments and cohesive and frictional components of strength. Damage-controlled tests which consist of a series of loading-unloading cycles present an opportunity to examine how each damage increment affect cohesion and friction angle. The results of damage-controlled tests carried out on samples of Lac du Bonnet granite and Indiana limestone at different levels of confining stress were used to explore the process of brittle failure in detail. Theoretical models were proposed to describe cohesion degradation and friction mobilization for the laboratory samples.

Excavations at the Underground Research Laboratory (URL) in Manitoba are close to an ideal case to study the behavior of a massive sparsely fractured rock mass with GSI of 90 to 100. The current Cohesion-Weakening Friction-Strengthening model (CWFS) proposed for modeling brittle failure at the URL was examined at a fundamental level under uniaxial and triaxial loading conditions. An improved theoretically plausible in situ brittle failure model was proposed. Four excavations at the URL, namely Mine-by, TSX, ESS (M1) and ESS (U1) were used as case study to verify the proposed modeling approach.

The final piece of the thesis deals with in situ behavior of rock masses with GSI of about 80. Such rock masses are typically encountered in hard rock pillars. Empirical pillar strength formulas were reviewed and a new semi-analytical formula based on the effect of size and shape on pillar strength was proposed. The proposed in situ brittle failure model was used to capture progressive failure of hard rock pillars. Documented behavior of pillars at the Elliot Lake and Selebi-Phikwe mines were used to verify the modeling approach. The effect of pillar width-to-height ratio on strength and deformability of pillars were explored. Stress-path at the wall and core of pillars was examined to study the effect of rock mass model on the overall pillar behavior. Pillar strength curves from empirical and numerical were compared and implications on pillar design were discussed. A pillar strength formula based on the results of the proposed modeling approach was presented for practical applications.

1.3. Organization of thesis

This thesis examines current methods of modelling the behaviour of good quality rock masses with GSI greater than 60 and provides new insight and improved modelling approaches. Chapter 2 deals with the strength characteristics and failure criteria for intact rock. Results of laboratory tests on different rock type under various loading conditions are used to examine two failure criteria on a fundamental level.

Monitoring the in situ behavior of rock mass around excavations offers invaluable information for modelling and calibration. Chapter 3 describes the process of back analysis of displacements around a deep shaft at an average quality rock mass using two- and three-dimensional models. The model parameters obtained from empirical estimation and back

analysis are compared and the current approach to displacement back analysis using two-dimensional models is challenged.

The progressive process of brittle failure can be studied using the results of damage-controlled laboratory tests and field observations in high in situ stress environments. Chapter 4 presents the results of such tests on Lac du Bonnet granite and Indiana limestone. Theoretical models for brittle failure are proposed and verified using in situ observations around different underground excavations in a massive rock mass. Guidelines are given for estimating the parameters of the proposed model.

The process of progressive failure can also be observed in hard rock pillars. Chapter 5 presents different approaches for modelling the behavior of pillars in good quality rock masses. Empirical methods are reviewed and a new semi-analytical pillar strength formula is suggested. The progressive failure model developed in the previous chapter is used to predict the behavior of pillar of various width-to-height ratios at two different mines. The results of empirical and numerical models were compared with in situ observations of pillar behavior.

A discussion and summary of the thesis is presented in Chapter 6.

Chapter 2

Application of the Christensen failure criterion to intact rock[1]

2.1. Introduction

Failure of rocks is considered to occur or be initiated at the peak strength (Jaeger and Cook, 1979). Hence, determination of strength of rock under different loading conditions is of great importance in the design of rock structures. While the rock mechanics literature is rich with numerous failure criteria and comparative studies (see, e.g., Colmenares and Zoback, 2002; Benz and Schwab, 2008; Rafiei, 2011), only two relatively old criteria with very simple equations namely, the Mohr-Coulomb and the Hoek-Brown criteria are most frequently used in rock engineering practice (Al-Ajmi and Zimmerman, 2005; Benz et al., 2008). In other words, most of the recently proposed criteria are of academic interest only and have not been suitable for practical applications either because of their complex forms which could not be conveniently used in analysis or involving too many parameters which could not be easily determined. Therefore, in spite of having so many criteria, there is still a great need to find new criteria which could be used in real-world applications. The suitable criterion for practical rock engineering purposes should satisfy the following conditions:

a) It should have a relatively simple mathematical form which can be understood and trusted by practitioners and can be conveniently implemented in numerical analysis by experts
b) It should have a small number of parameters which can be determined from relatively easy and well-established tests
c) It should give good agreement with the experimentally determined strength values of rocks under different loading conditions

Recently, a new failure criterion was introduced to the rock mechanics community and it was suggested to be probably "an answer to true representative modeling of intact rock failure" (Hammah and Carvalho, 2011). The criterion was initially introduced by Christensen in 1997, and has been described in several publications (Christensen, 1997, 2000, 2004, 2005, 2006a&b, 2007).

---

[1] A version of this chapter is published as a paper by the journal of Geotechnical and Geological Engineering:
Rafiei Renani, H., Martin, C.D. (2016), Application of the Christensen Failure Criterion to Intact Rock, Geotech Geolog Eng, 34, 297-312.

This criterion satisfies the first two conditions outlined above. It has a simple mathematical form expressed in terms of stress invariants which can be conveniently implemented in numerical methods. It also has only two parameters, the uniaxial compressive and tensile strength, which can be determined from the well-established tests. Unfortunately, Hammah and Carvalho (2011) did not apply the Christensen criterion to rock failure data. The objective of this study was to evaluate the accuracy of the Christensen criterion in prediction of rock strength and examine whether it satisfies the third condition.

A comprehensive set of strength data for four rock types under a wide range of loading conditions is compiled and the Christensen criterion is used to fit the data. As a first step, only the strength of intact rock is considered in this study and no attempt has been made to deal with the complex behavior of rock masses. In order to put the accuracy of the Christensen criterion into perspective, the well-established Hoek-Brown criterion is also applied to the same strength data. Consistent with approach taken by Christensen (2004) and Hoek and Brown (1980), only the peak strength corresponding to ultimate failure is considered in this paper and no attempt has been made to address the crack initiation or unstable crack growth thresholds.

In the next sections, a complete description of the Christensen criterion and its mathematical components are presented. The results of the application of the criterion to intact rock data are given, and the overall consistency of the Christensen criterion with observed failure characteristics of rock material is examined. Finally, the applicability of the Christensen criterion for rock failure is discussed.

2.2. The Christensen criterion

In this section, the Christensen criterion and its components are introduced. The criterion has two parameters, and is proposed for failure of homogeneous isotropic materials with uniaxial compressive strength equal to or greater than the tensile strength. The criterion was developed using the mechanics sign convention for stresses, and for the purposes of this paper has been modified to the geomechanics sign convention, i.e, compression positive.

In order to fully understand the Christensen criterion, the complete derivation of the criterion is presented. In addition, explicit equations for strength under general and special loading conditions are derived.

2.2.1. Derivation of the main parabolic criterion

The general form of a failure criterion is:

$$f\left(\sigma_{ij}\right) = 0$$

(2.1)

where σ_{ij} represents the six components of the stress tensor specifying the magnitude and direction of principal stresses relative to the coordinate system. For isotropic material, strength is independent of the direction. Hence, the failure criterion can be expressed only in terms of the magnitude of the principal stresses:

$$f(\sigma_1, \sigma_2, \sigma_3) = 0 \tag{2.2}$$

where σ_1, σ_2, σ_3 and are the major, intermediate and minor principal stresses, respectively. The principal stresses can also be expressed in terms of the stress invariants which are more convenient for analytical and numerical implementations:

$$f(I_1, J_2, J_3) = 0 \tag{2.3}$$

where I_1 is the first invariant of the stress tensor, J_2 is the second invariant of the deviatoric stress tensor, and J_3 is the third invariant of the deviatoric stress tensor given by:

$$I_1 = (\sigma_1 + \sigma_2 + \sigma_3) \tag{2.4}$$

$$J_2 = \frac{1}{6}\left[(\sigma_1 - \sigma_2)^2 + (\sigma_2 - \sigma_3)^2 + (\sigma_3 - \sigma_1)^2\right] \tag{2.5}$$

$$J_3 = \left(\sigma_1 - \frac{I_1}{3}\right)\left(\sigma_2 - \frac{I_1}{3}\right)\left(\sigma_3 - \frac{I_1}{3}\right) \tag{2.6}$$

Using the polynomial expansion and terminating at the second order terms, Eq. (2.3) can be expressed as:

$$a_0 + a_1 I_1 + a_2 I_1^2 + a_3 J_2 = 0 \tag{2.7}$$

where a_0, a_1, a_2 and a_3 are constants. Note that J_3 is eliminated in Eq. (2.7) because it is a third order term. In Eq. (2.7), the parameter a_0 merely establishes a datum and can be chosen arbitrarily. Considering the fact that homogeneous isotropic materials do not fail under hydrostatic compression (Christensen, 1997), the parameter a_2 must be equal to zero. Hence, Eq. (2.7) can be re-written as:

$$a_1 I_1 + a_3 J_2 = 1 \tag{2.8}$$

By satisfying Eq. (2.8) for uniaxial compression and tension conditions, the two remaining constants can be easily found as:

$$a_1 = \frac{1}{\sigma_c} - \frac{1}{\sigma_t} \tag{2.9}$$

$$a_3 = \frac{3}{\sigma_c \sigma_t}$$

(2.10)

where σ_c and σ_t are the absolute values of uniaxial compressive and tensile strength. Hence, the final criterion expressed in terms of principal stresses can be given by:

$$\left(\frac{1}{\sigma_c} - \frac{1}{\sigma_t}\right)(\sigma_1 + \sigma_2 + \sigma_3) + \left(\frac{1}{\sigma_c} \cdot \frac{1}{\sigma_t}\right)\left\{\frac{1}{2}\left[(\sigma_1 - \sigma_2)^2 + (\sigma_2 - \sigma_3)^2 + (\sigma_3 - \sigma_1)^2\right]\right\} = 1$$

(2.11)

This is the main parabolic part of the failure criterion proposed by Christensen (1997). However, the first term on the left hand side of Eq. (2.11) has the opposite sign from that originally proposed. This is because of the different sign conventions adopted in mechanics and geomechanics where compressive stresses are considered negative in the mechanics sign convention and positive in the geomechanics sign convention.

The criterion derived above bears some similarities to criteria based on elastic energy considerations (Christensen, 2004). The first and second terms on the left hand side of Eq. (2.11) are directly related to volumetric and distortional energy terms, respectively. For the case of $\sigma_c = \sigma_t$, the first term vanishes and the criterion is reduced to the von Mises criterion which is based on the concept of maximum distortional energy.

2.2.2.   Explicit forms of the criterion

The criterion proposed by Christensen provides an implicit relationship between the principal stresses at failure. However, derivation of an explicit form is useful in the application of the criterion to measured strength data.

In the general case of a polyaxial state of stress where the three principal stresses are different, solving Eq. (2.11) for σ_1 gives two roots. The root with the higher value is by definition the major principal stress:

$$\sigma_1 = \frac{1}{2}\left[(\sigma_2 + \sigma_3) + (\sigma_c - \sigma_t) + \sqrt{(\sigma_c + \sigma_t)^2 + 6(\sigma_2 + \sigma_3)(\sigma_c - \sigma_t) - 3(\sigma_2 - \sigma_3)^2}\right]$$

(2.12)

Eq. (2.12) can be used in analysis of the results of polyaxial tests.

In a triaxial state of stress, two principal stresses are equal to the confining pressure p, and the third principal stress is equal to the axial stress σ_{ax}. For triaxial compression tests, the axial stress is higher than the confining pressure, $\sigma_1 = \sigma_{ax}$ and $\sigma_2 = \sigma_3 = p$. Hence, Eq. (2.12) reduces to:

$$\sigma_1 = \sigma_3 + \frac{1}{2}\left[(\sigma_c - \sigma_t) + \sqrt{(\sigma_c + \sigma_t)^2 + 12\sigma_3(\sigma_c - \sigma_t)}\right]$$

(2.13)

For triaxial extension tests on the other hand, the confining pressure is higher than the axial stress, $\sigma_1 = \sigma_2 = p$ and $\sigma_3 = \sigma_{ax}$. Hence, Eq. (2.12) gives:

$$\sigma_1 = \sigma_3 + \left[(\sigma_c - \sigma_t) + \sqrt{(\sigma_c - \sigma_t)^2 + 3\sigma_3(\sigma_c - \sigma_t) + \sigma_c\sigma_t}\right]$$

(2.14)

In a biaxial state of stress, one of the principal stresses is zero. By putting $\sigma_3 = 0$ in Eq. (2.12), the strength can be calculated as:

$$\sigma_1 = \frac{1}{2}\left[\sigma_2 + (\sigma_c - \sigma_t) + \sqrt{(\sigma_c + \sigma_t)^2 + 6\sigma_2(\sigma_c - \sigma_t) - 3\sigma_2{}^2}\right]$$

(2.15)

2.2.3.   Tension cut-off

Although the Christensen parabolic criterion derived above has some similarities with the elastic energy concept, it is simply based on a polynomial expansion of stress invariants up to the second order terms and satisfies uniaxial compression and tension conditions. This approach leads to a problem under tensile stress. For materials with $\sigma_c > 2\sigma_t$, which includes all rock types, Eq. (2.11) leads to tensile stresses higher than the tensile strength of the material. Hence, a tension cut-off is required in these cases:

$$\sigma_3 = -\sigma_t$$

(2.16)

This expression for the tension cut-off is also different from the one originally proposed (Christensen, 2004) because the largest principal tensile stress according to the geomechanics sign convention is σ_3 while σ_1 is the largest tensile stress in the mechanics sign convention.

2.2.4.   Brittle to ductile transition

In the context of the Christensen criterion, brittle and ductile behaviors are closely related to the ratio of uniaxial compression strength to tensile strength. Materials with similar uniaxial compression and tension strengths such as steel are considered ductile while materials with uniaxial compression strength much higher than uniaxial tensile strength such as rocks may show brittle behavior (Christensen, 2005).

The brittle to ductile transition criterion is defined by a plane in principal stress space which connects the three points in each principal stress plane where the main failure surface given

by Eq. (2.11) intersects the tension cut-off (Christensen, 2005). For example, the coordinate of the point of intersection in the $\sigma_2 - \sigma_1$ plane can be found by putting $\sigma_2 = -\sigma_t$ in Eq. (2.15) which gives $\sigma_1 = \sigma_c - 2\sigma_t$. The plane of brittle to ductile transition which encompasses the three intersection points can be given by (Christensen, 2005):

$$\left(\sigma_1 + \sigma_2 + \sigma_3\right) = \sigma_c - 3\sigma_t \tag{2.17}$$

Again, there is an opposite sign in this equation compared to the one originally proposed because of different sign conventions. According to the Christensen criterion, for a given material, the brittle or ductile behavior depends only on the volumetric stress, and there is a threshold of volumetric compressive stress above which the behavior is completely ductile.

The Christensen failure surface in three-dimensional principal stress space for a typical rock material with $\sigma_c/\sigma_t = 12$ is shown in Fig. 2.1a. The main parabolic surface and the three tension cut-off planes which have truncated the surface can be observed. Fig. 2.1b shows the biaxial plane section of the failure surface where one of the principal stresses is zero. It can be observed that the tension cut-off in effect eliminates tensile stresses higher than the tensile strength. In addition, the trace of the brittle to ductile transition plane passes through the points of intersection of the parabolic surface and the tension cut-off. The section of the failure surface in the triaxial plane, where two principal stresses are equal is shown in Fig. 2.1c. It is worth noting that the trace of the brittle to ductile transition plane does not pass through the points of intersection of the main surface and the tension cut-off except for the case of biaxial planes. According to Figs. 2.1b and c, the mode of failure in most of the compressive region is ductile. More specifically, it can be observed that the predicted mode of failure in triaxial compression tests is ductile failure. Fig. 2.1d shows the cross section of the failure surface in the π-plane. It can be observed that the Christensen criterion gives circular sections because the third invariant of the deviatoric stress tensor which is related to the Lode angle and the angular coordinate in the π-plane is eliminated in Eq. (2.8). Therefore for each value of the first stress invariant, the second invariant of the deviatoric stress tensor which is directly related to the radial coordinate in the π-plane is constant and independent of the angular coordinate producing circular cross sections.

2.3. The Hoek-Brown criterion

This criterion was first proposed for the failure of intact rock and rock masses by Hoek and Brown (1980). Since then, it has undergone several stages of development (Hoek, 1983, 1990; Hoek et al., 1992; Hoek and Brown, 1997; Hoek et al., 2002) and has been widely used in rock engineering. The latest version of the criterion known as the generalized Hoek-Brown criterion can be expressed as (Hoek et al., 2002):

$$\sigma_1 = \sigma_3 + \sigma_c \left(m \frac{\sigma_3}{\sigma_c} + s \right)^a \tag{2.18}$$

where m, s, and a are the parameters of this criterion, and σ_c is the uniaxial compressive strength of intact rock. For an undamaged intact rock, $s = 1$ and $a = 0.5$, resulting in a two-parameter criterion.
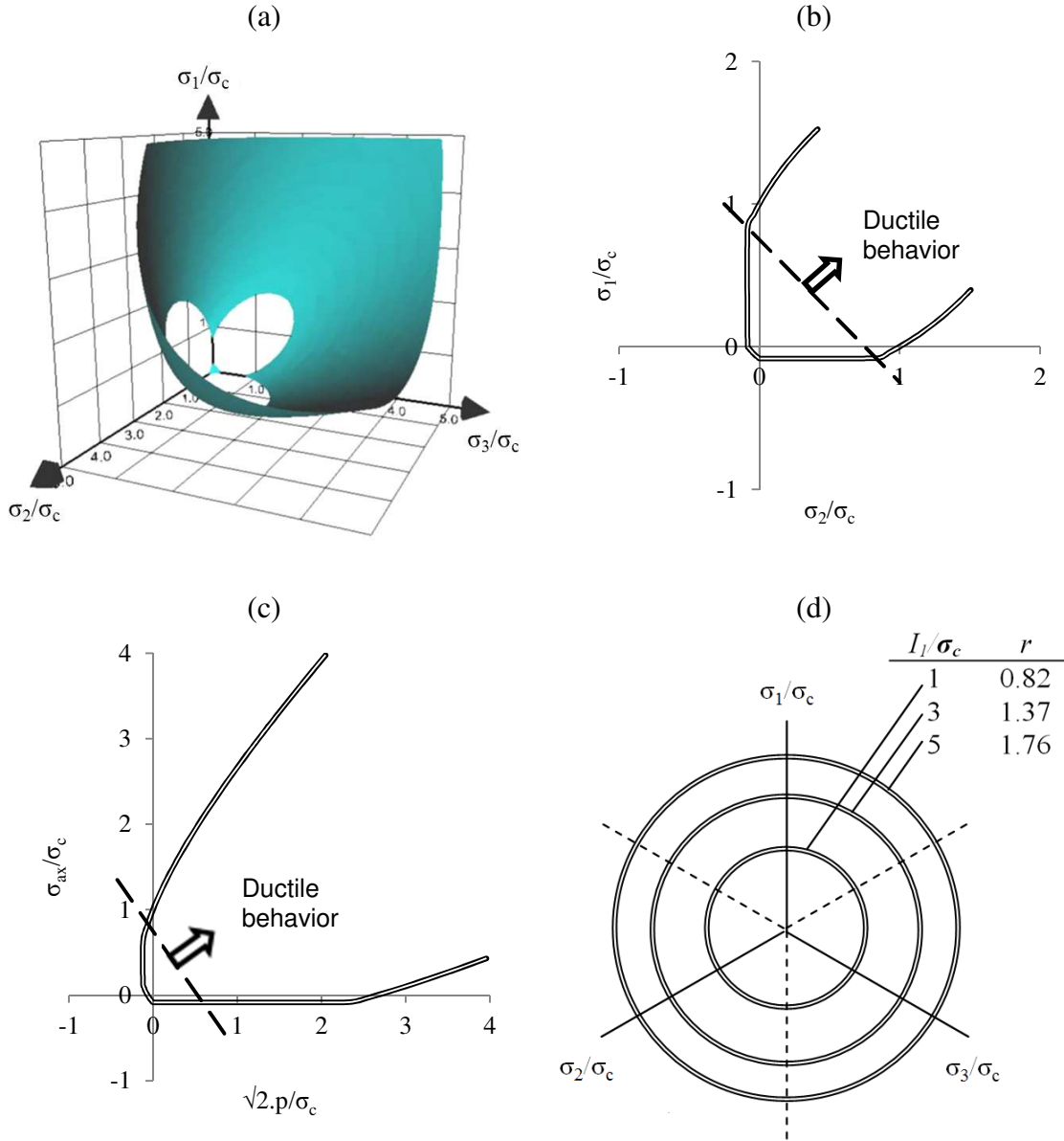
Fig. 2.1 The Christensen failure envelopes for a material with $\sigma_c/\sigma_t = 12$ in (a) three-dimensional principal stress space, (b) the biaxial plane $\sigma_3 = 0$, (c) the triaxial plane $\sigma_2 = \sigma_3 = p$, (d) the π-plane (the radius r of the circles is given for different values of I_1/σ_c)

To make it consistent with the Christensen criterion, it is useful to express the Hoek-Brown parameter m is terms of σ_c andσ_t. By putting $\sigma_1 = 0$ into Eq. (2.18), the absolute value of tensile strength for intact rock can be given by:

$$\sigma_t = \frac{\sigma_c}{2}\left|m - \sqrt{m^2 + 4}\right|$$

(2.19)

Hence, the parameter m for intact rock can be expressed as:

$$m = \frac{\sigma_c}{\sigma_t} - \frac{\sigma_t}{\sigma_c}$$

(2.20)

The Hoek-Brown criterion is fundamentally different from the Christensen criterion. While the Christensen criterion is proposed for all homogeneous isotropic materials with uniaxial compressive strength equal to or greater than the tensile strength, the Hoek-Brown criterion is specifically proposed for rocks. In addition, the intermediate principal stress has never appeared in any versions of the Hoek-Brown criterion proposed by the original developers (Hoek, 1983, 1990; Hoek et al., 1992; Hoek and Brown, 1980, 1997; Hoek et al., 2002). However, the intermediate principal stress is present in the equations of the Christensen criterion.

Some researchers (e.g, Benz et al., 2008; Pan and Hudson, 1988; Priest, 2005; Zhang and Zhu, 2007) have proposed modified version of the Hoek-Brown criterion to take into account the effect of the intermediate principal stress. However, the authors consciously decided to use the original form given in Eq. (2.18) partly because this form is in keeping with the first premise of simplicity and is most frequently-used for practical purposes. As it will be shown in the subsequent sections, this decision will not change the final outcome of this study.

2.4. Analysis of strength data

In order to examine the applicability of any criterion to rock materials, it is crucial to utilize a reliable set of strength data for a wide range of loading conditions. In this study, four data sets obtained from high quality laboratory tests are compiled. The tests have been carried out on intact rock specimens under different states of stress including uniaxial tension, uniaxial compression, triaxial compression, triaxial extension, and polyaxial compression. While there is no comprehensive set of data for strength of rock masses under these varying loading conditions, only the results of tests on intact rock have been used in this study. As it will be shown in the following sections, these data are sufficient to explore the merit of the Christensen criterion for rock material.

Two general scenarios are followed in the following analyses. In the first scenario, no fitting process is involved and the measured values of uniaxial compressive and tensile strength are used to predict the failure envelopes. This approach examines how accurate the failure criteria are when only the measured values for the parameters σ_c and σ_t are used. In the second scenario, date fitting analysis using the Least Squares Method is involved to find the optimized values for parameters σ_c and σ_t which best fit the data and minimizes the model errors. In this approach, the ultimate capacity of the criteria to fit the data is examined. These two approaches are complementary and provide a complete picture of both criteria.

In order to quantify the accuracy of the criteria, it is necessary to use an error index. In this study, the Root Mean Squared Error (RMSE) in the prediction of the major principal stresses at failure is selected as the error index:

$$RMSE = \sqrt{\frac{1}{n}\sum_{i=1}^{n}\left(\sigma_{1,i}^{p} - \sigma_{1,i}^{m}\right)^{2}}$$

(2.21)

Where $\sigma_{1,i}^{p}$ and $\sigma_{1,i}^{m}$ are the predicted and measured values of σ_1 for i'th data, respectively, and n is the number of data points.

2.4.1. Application of the criteria to synthetic rock

Nguyen et al. (2011) prepared a granular synthetic rock which shows the main characteristics of real rocks such as cohesion, friction, and dilation. However, the synthetic rock had incredibly low strength and rigidity. A comprehensive and careful testing program was carried out on samples of the synthetic rock. The triaxial compression and extension test results are used in this study. More details about the testing procedure are given by Nguyen et al. (2011).

The measured average values of uniaxial compressive and tensile strength for the synthetic rock are 0.57 and 0.07 MPa, respectively (Nguyen et al., 2011). Fig. 2.2 shows the Christensen and Hoek-Brown failure envelopes with these measured values for the parameters. It can be observed that the Christensen failure envelope is more accurate for triaxial compression while the Hoek-Brown envelope is more accurate for triaxial extension. However, both criteria have overestimated the strength of the synthetic rock.

If only the results of triaxial compression tests are used for determination of the parameters of the two criteria, the obtained values of uniaxial compressive and tensile strength are 0.56 and 0.12 MPa for the Christensen criterion and 0.57 and 0.18 MPa for the Hoek-Brown criterion. It can be observed that the obtained values for uniaxial compressive strength are very close to the measured values while the obtained values for uniaxial tensile strength are much higher than the measured value.

Using results of triaxial extension tests for determination of the parameters, the obtained values of uniaxial compressive and tensile strength are 0.38 and 0.07 MPa for the Christensen criterion and 0.53 and 0.10 MPa for the Hoek-Brown criterion. It can be observed that for the Christensen criterion, the obtained value for uniaxial tensile strength is very close to the measured value while the obtained value for the uniaxial compressive strength is much less than the measured value. On the other hand, for the Hoek-Brown criterion, the obtained value for uniaxial tensile strength is slightly higher than the measured value and the obtained values for uniaxial compressive strength is slightly less than the measured value.
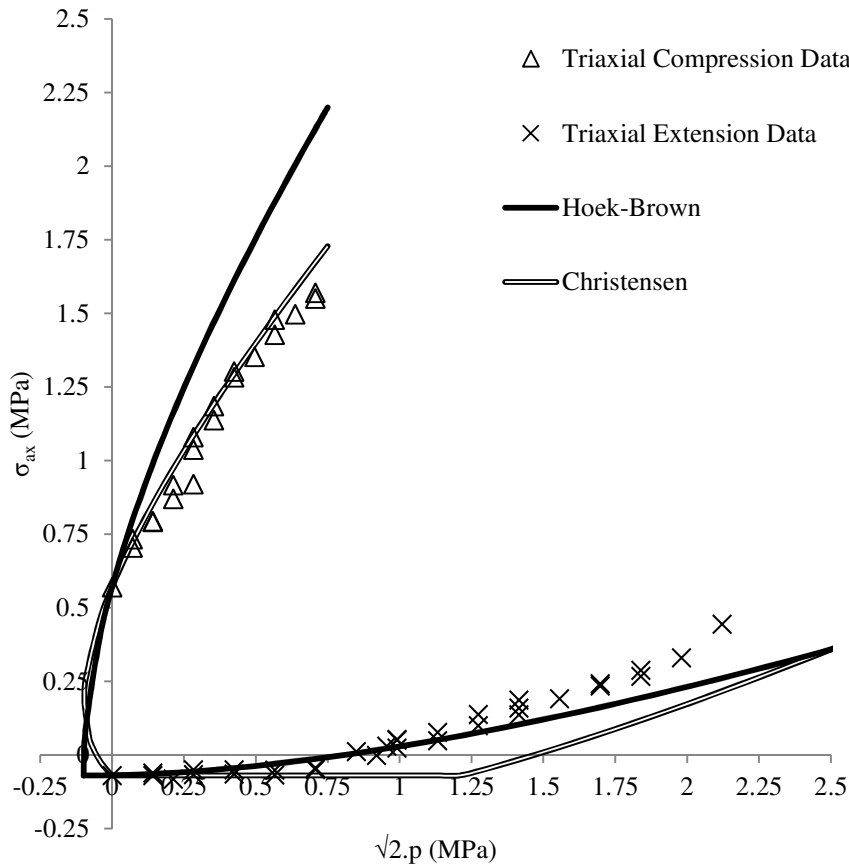
Fig. 2.2 The failure envelopes based on the measured values of the uniaxial compressive and tensile strength for the synthetic rock compared to the measured triaxial and extension dataset

If the results of both triaxial compression and extension tests are used, the obtained values of uniaxial compressive and tensile strength are 0.43 and 0.07 MPa for the Christensen criterion and 0.52 and 0.11 MPa for the Hoek-Brown criterion. It can be observed that for the Christensen criterion, the obtained value for uniaxial tensile strength is very close to the measured value while the obtained values for uniaxial compressive strength is much less than the measured value. On the other hand, for the Hoek-Brown criterion, the obtained

value for uniaxial tensile strength is higher than the measured value and the obtained values for uniaxial compressive strength is slightly less than the measured value. The failure envelopes fitted to the results of both triaxial compression extension tests are shown in Fig. 2.3.

Table 2.1 gives a summary of the results of the analyses on the synthetic rock. It can be observed that the Christensen criterion gives more accurate estimates of the uniaxial tensile strength. However, in all cases, the Hoek-Brown criterion gives closer estimates of the uniaxial compressive strength and lower values of RMSE.
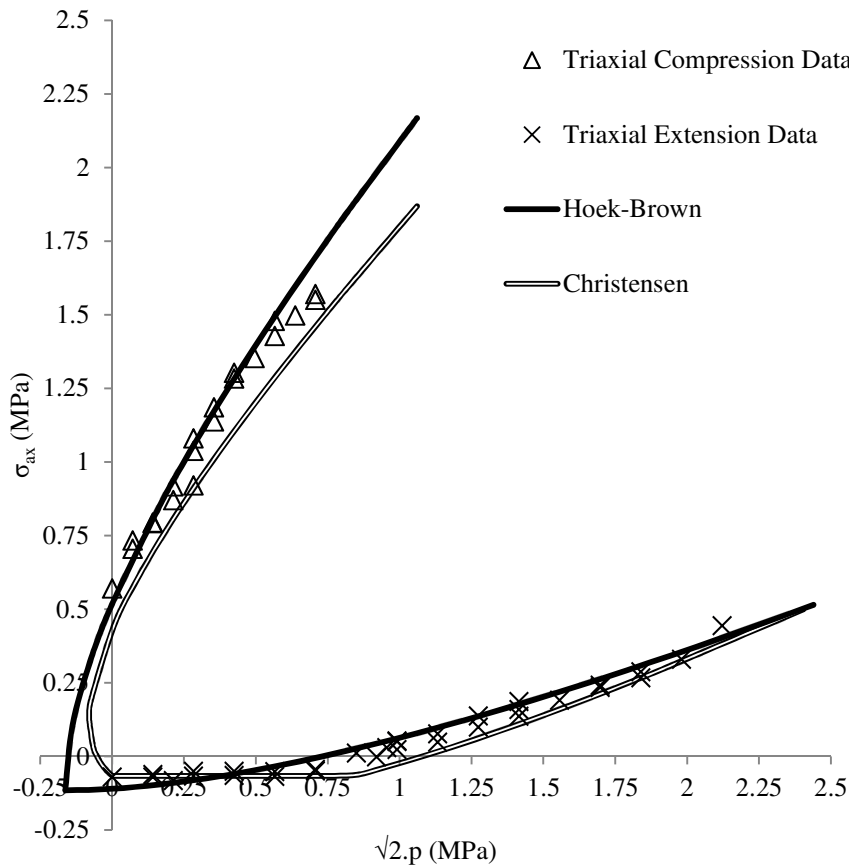
Fig. 2.3 The failure envelopes fitted to the results of both triaxial compression and extension tests for the synthetic rock

2.4.2.   Application of the criteria to chert dyke

Although the strength data for the synthetic rock were comprehensive and reliable, analyses were also carried out using careful triaxial compression tests on a highly siliceous fine grained rock known as chert dyke (Hoek, 1965). This material was chosen because it is free

from major geological features and is close to an ideal isotropic elastic solid (Hoek, 1965). More details about the testing procedure are given by Hoek (1965).

Table 2.1 The results of application of failure criteria for the synthetic rock

Scenario	Christensen criterion			Hoek-Brown criterion		
	σ_c (MPa)	σ_t (MPa)	RMSE (MPa)	σ_c (MPa)	σ_t (MPa)	RMSE (MPa)
Using measured parameters	0.57	0.07	0.30	0.57	0.07	0.26
Fitting to triaxial compression data	0.56	0.12	0.23	0.57	0.18	0.11
Fitting to triaxial extension data	0.38	0.07	0.14	0.53	0.10	0.11
Fitting to compression and extension data	0.43	0.07	0.13	0.52	0.11	0.09

The measured values of uniaxial compressive and tensile strength for the chert dyke are 586 and 34.5 MPa, respectively (Hoek, 1965). Fig. 2.4a shows the Christensen and Hoek-Brown failure envelopes with these measured values for the parameters. It can be observed that the Christensen failure envelope significantly underestimates the triaxial strength of the chert dyke while the Hoek-Brown envelope gives a good fit to the measured data.
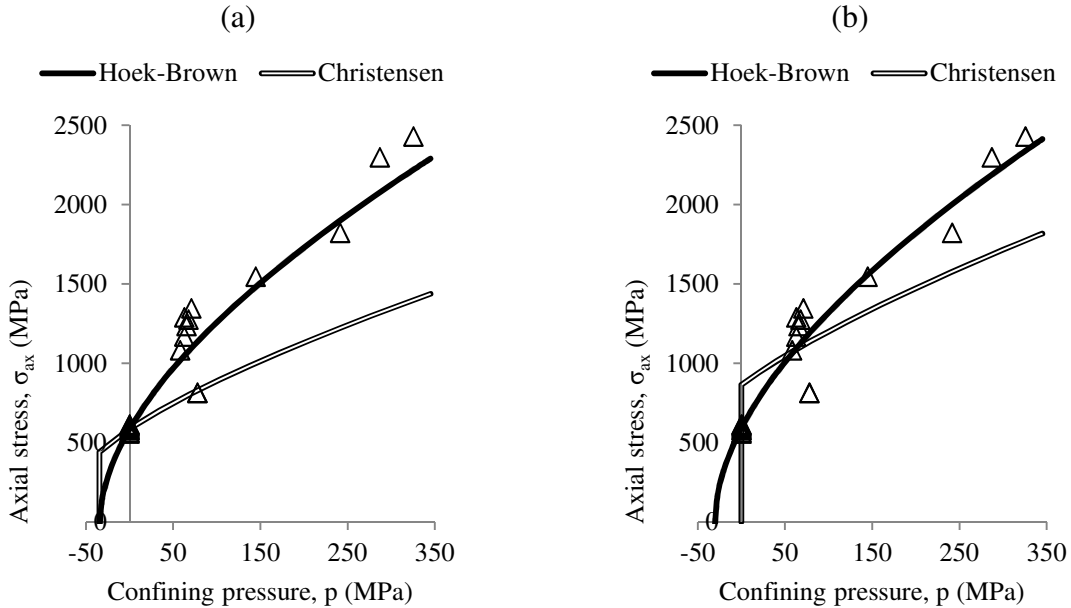
Fig. 2.4 The failure envelopes for the chert dyke (a) using the measured values, (b) optimized for the uniaxial compressive and tensile strength

Using the results of triaxial compression tests, the obtained value of uniaxial compressive strength for the Christensen criterion is 865 MPa while the obtained tensile strength is zero. For the Hoek-Brown criterion, the obtained values of uniaxial compressive and tensile strength are 591 and 30.7 MPa, respectively. Fig. 2.4b shows the Christensen and Hoek-

Brown failure envelopes with these optimized values for the parameters. It can be observed that the Hoek-Brown envelope essentially has not changed. On the other hand, although the Christensen envelope is closer to the measured values, it still underestimates the triaxial compressive strength significantly. The surprising points are the zero values of uniaxial tensile strength obtained from the fitting process and the low slope of the failure envelope.

Table 2.2 provides a summary of the results of analyses on the chert dyke. It can be observed that in both scenarios, the Hoek-Brown criterion gives more accurate estimates of the uniaxial compressive and tensile strengths. In addition, the RMSE values for the Christensen criterion are more than double the values for the Hoek-Brown criterion.

Table 2.2 The results of application of failure criteria for chert dyke

Scenario	Christensen criterion			Hoek-Brown criterion		
	σ_c (MPa)	σ_t (MPa)	RMSE (MPa)	σ_c (MPa)	σ_t (MPa)	RMSE (MPa)
Using measured parameters	586.2	34.5	440.2	586.2	34.5	161.3
Fitting to triaxial compression data	864.6	0.0	306.7	590.9	30.7	151.4

2.4.3.   Application of the criteria to Carrara marble

The next set of data used in this study was obtained from careful triaxial extension tests on Carrara marble which captured the hybrid fracture and transition from extension fracture to shear fracture (Ramsey and Chester, 2004). The marble is a relatively homogeneous and isotropic material with extremely low porosity and little crystal-lattice preferred orientation (Ramsey and Chester, 2004). More details about the testing procedure are given by Ramsey and Chester (2004).

The measured values of uniaxial compressive and tensile strength for the Carrara marble are 94 and 6.9 MPa, respectively (Haimson and Chang, 2000; Howarth and Rowlands, 1987). Fig. 2.5a shows the Christensen and Hoek-Brown failure envelopes with these measured values for the parameters. It can be observed that the Hoek-Brown criterion underestimates the triaxial extension strength and the Christensen criterion significantly overestimates it.

 Using the results of triaxial extension tests, the obtained values of uniaxial compressive and tensile strength are 70 and 8.5 MPa for the Christensen criterion and 119 and 13.2 MPa for the Hoek-Brown criterion. Fig. 2.5b shows the Christensen and Hoek-Brown failure envelopes with these optimized values for the parameters. It can be observed that in this case, the Christensen envelope is closer to the measured data points. However, it should be noted that the slope of the Hoek-Brown envelope in intermediate to high ranges of confining pressure is very similar to that of the data points. However, the slope of the Christensen envelope in that range is not representative of the data points and it will underestimate the strength at high levels of confining pressure not included in this data set.

(a)

(b)
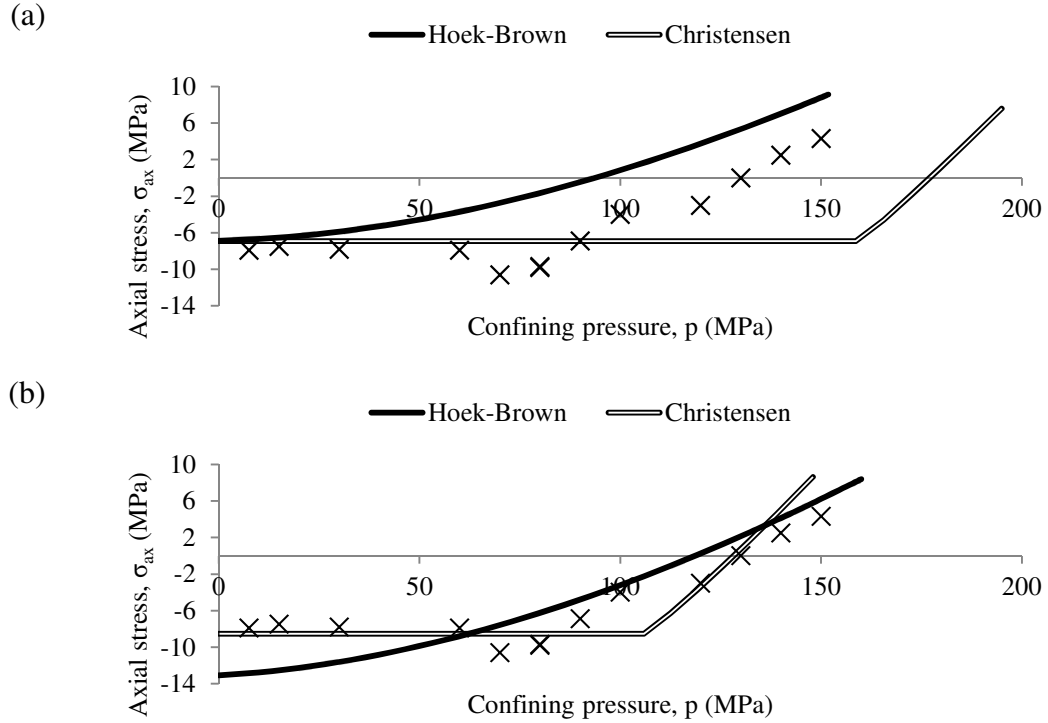
Fig. 2.5 The failure envelopes for the Carrara marble (a) using the measured values, (b) optimized for the uniaxial compressive and tensile strengths

Table 2.3 gives a summary of the results of the analyses on the Carrara marble. It can be observed that in the first scenario, the Christensen criterion gives higher values of RMSE. However, in the second scenario, the Christensen criterion gives more accurate estimates of the uniaxial compressive and tensile strengths and slightly lower values of RMSE compared to the Hoek-Brown criterion.

Table 2.3 The results of application of failure criteria for Carrara marble

Scenario	Christensen criterion			Hoek-Brown criterion		
	σ_c (MPa)	σ_t (MPa)	*RMSE* (MPa)	σ_c (MPa)	σ_t (MPa)	*RMSE* (MPa)
Using measured parameters	93.6	6.9	49.8	93.6	6.9	38.6
Fitting to triaxial extension data	70.3	8.5	10.1	118.6	13.2	11.4

2.4.4. Application of the criteria to Westerly granite

The final set of data used in this study is obtained from careful polyaxial tests on Westerly granite (Haimson and Chang, 2000) to explore the accuracy of the Christensen criterion in polyaxial states of stresses where the intermediate principal stress varies between the major

and minor principal stresses. The important properties of the granite include very low porosity, high strength, and almost complete linear elasticity, homogeneity, and isotropy (Krech et al., 1974). More details about the testing procedure are given by Haimson and Chang (2000).

The measured values of uniaxial compressive and tensile strength for the Westerly granite are 201 MPa and 12 MPa, respectively (Johnson et al., 1987; Krech et al., 1974). Fig. 2.6 shows the Christensen and Hoek-Brown failure envelopes with these parameters. As expected, the Christensen criterion is capable of producing the strengthening effect of the intermediate principal stress while the Hoek-Brown criterion ignores this effect. Although both criteria considerably underestimate the strength of Westerly granite, the predictions of the Christensen criterion are less accurate than those of the Hoek-Brown criterion.
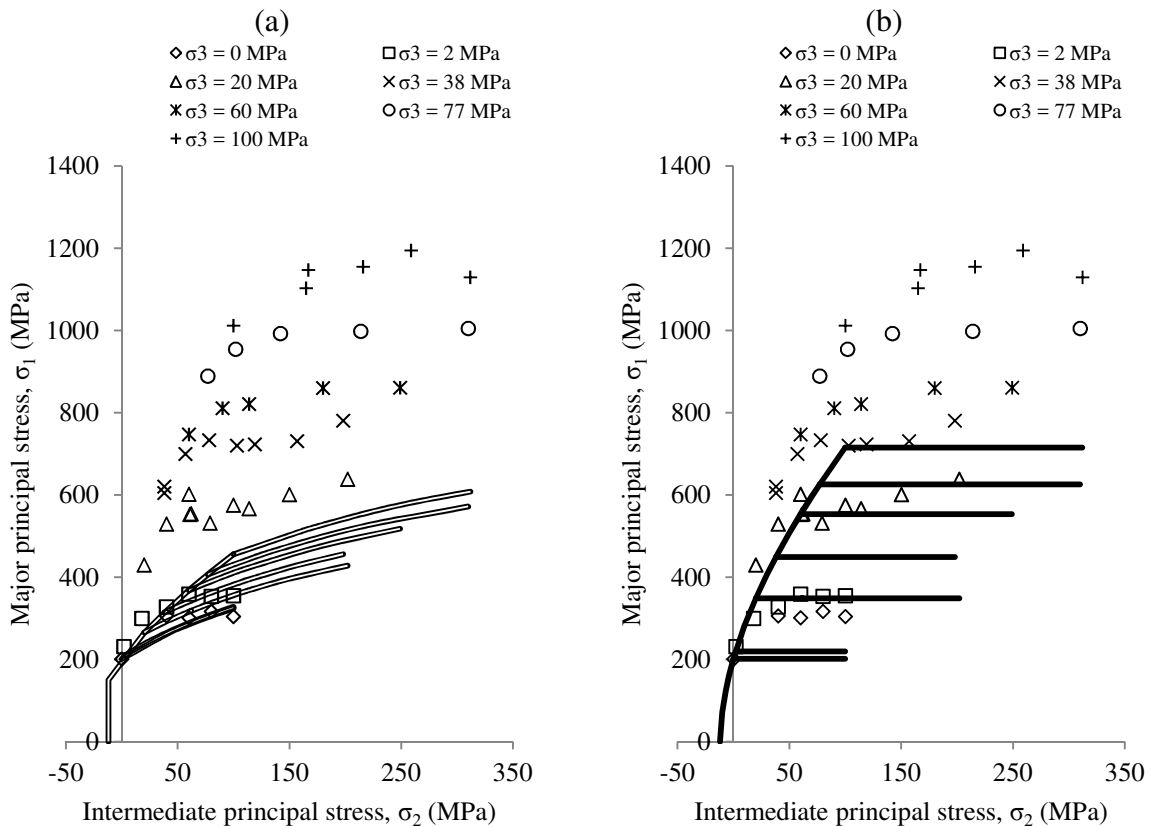
Fig. 2.6 The failure envelopes for Westerly granite based on measured values of uniaxial compressive and tensile strength using (a) the Christensen criterion, (b) the Hoek-Brown criterion, compared to the measured polyaxial dataset

If the polyaxial strength data are used for determination of the parameters, the obtained value of uniaxial compressive strength for the Christensen criterion is 453 MPa while the obtained tensile strength is zero as in the case of chert dyke. For the Hoek-Brown criterion,

the obtained values of uniaxial compressive and tensile strength in this case are 292 and 9.2 MPa, respectively. Fig. 2.7 shows the Christensen and Hoek-Brown failure envelopes with these parameters. It can be observed that although the Hoek-Brown criterion does not capture the strengthening effect of the intermediate principal stress, it provides a high slope for the triaxial compression condition and gives a reasonable average strength at each level of minor principal stress. On the other hand, the Christensen criterion shows a very poor fit to the measured data. Again, the zero values of uniaxial tensile strength obtained from the fitting process and the low slope of the triaxial failure envelope are worth noting.
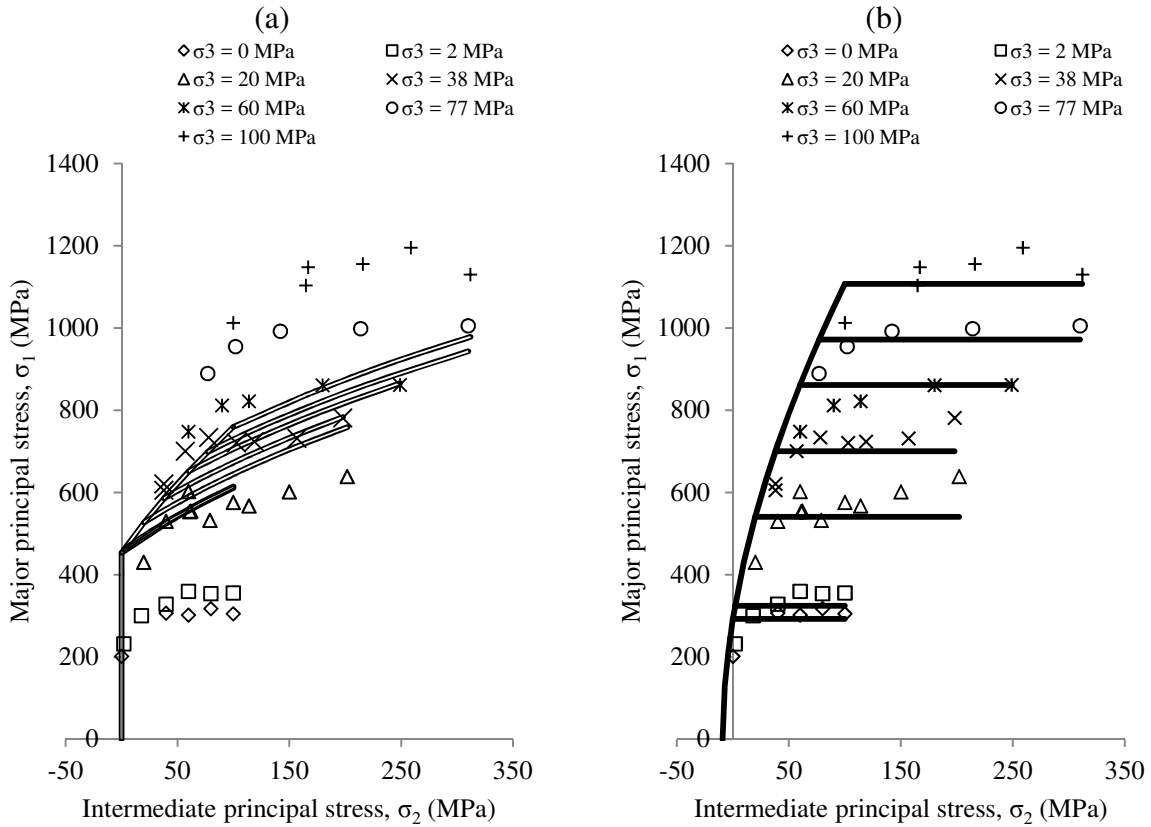
Fig. 2.7 The failure envelopes for Westerly granite fitted to the results of polyaxial tests using (a) the Christensen criterion, (b) the Hoek-Brown criterion

Table 2.4 gives a summary of the results of the analyses on the Westerly granite. It can be observed that in both scenarios, the RMSE values for the Christensen criterion are higher than those for the Hoek-Brown criterion. In addition, the obtained values of uniaxial compressive and tensile strength for the Hoek-Brown criterion are more accurate.

Table 2.4 The results of application of failure criteria for Westerly granite

Scenario	Christensen criterion			Hoek-Brown criterion		
	σ_c (MPa)	σ_t (MPa)	*RMSE* (MPa)	σ_c (MPa)	σ_t (MPa)	*RMSE* (MPa)
Using measured parameters	201	12.0	345	201	12.0	262
Fitting to polyaxial data	453	0.0	169	292	9.2	53

2.5. Discussion

The average values of RMSE under different scenarios for each rock type are given in Table 2.5. The results show that for all rock types, the RMSE values of the Christensen criterion are higher than those of the Hoek-Brown criterion. On average, the Hoek-Brown criterion is 65% more accurate than the Christensen criterion. In addition, in all cases except for the triaxial extension of the Carrara marble, the values of the uniaxial compressive strength obtained from the fitting analyses for the Hoek-Brown criterion were more accurate than those for the Christensen criterion.

Table 2.5 The average error values for the Christensen criterion, $RMSE_{Ch}$ and the Hoek-Brown criterion, $RMSE_{HB}$

Rock type	$RMSE_{Ch}$ (MPa)	$RMSE_{HB}$ (MPa)	$\dfrac{RMSE_{Ch}}{RMSE_{HB}}$
Synthetic rock	0.20	0.14	1.40
Chert dyke	373.4	156.3	2.38
Carrara marble	29.9	25.0	1.19
Westerly granite	257.0	157.5	1.63
		Average	**1.65**

However, the results for tensile strength are more complicated. For the synthetic rock and Carrara marble, the values of tensile strength for the Christensen criterion obtained from the analyses of data were more accurate. In contrast, the fitting analyses of the results of tests on chert dyke and Westerly granite led to zero values of tensile strength for the Christensen criterion.

Another notable point is the low slope of the Christensen failure envelopes obtained for the chert dyke, Carrara marble and Westerly granite. In order to find the reason for the obtained zero values for the tensile strength and the low slopes of the failure envelopes, it is useful to derive expressions for the slopes of the failure envelopes.

The slope of failure envelope in triaxial compression can be obtained from Eq. (2.13) as:

$$\frac{d\sigma_1}{d\sigma_3} = 1 + \frac{3(\sigma_c - \sigma_t)}{\sqrt{(\sigma_c + \sigma_t)^2 + 12\sigma_3(\sigma_c - \sigma_t)}}$$

(2.22)

It can be observed that, as expected, the slope of this failure envelope decreases with increasing minor principal stress. The initial slope at $\sigma_3 = 0$ can be calculated as:

$$\left(\frac{d\sigma_1}{d\sigma_3}\right)_{\sigma_3=0} = 1 + 3\frac{(\sigma_c / \sigma_t - 1)}{(\sigma_c / \sigma_t + 1)}$$

(2.23)

Obviously, the initial slope increases with an increasing ratio of uniaxial compressive strength to tensile strength. However, the limit of the initial slope as this ratio tends to infinity is 4.

Following the same procedure, the slope of the failure envelope in triaxial extension can be calculated from Eq. (2.14) as:

$$\frac{d\sigma_1}{d\sigma_3} = 1 + \frac{3(\sigma_c - \sigma_t)}{2\sqrt{(\sigma_c - \sigma_t)^2 + 3\sigma_3(\sigma_c - \sigma_t) + \sigma_c\sigma_t}}$$

(2.24)

and the initial slope at $\sigma_3 = 0$ is given by:

$$\left(\frac{d\sigma_1}{d\sigma_3}\right)_{\sigma_3=0} = 1 + \frac{3}{2}\frac{(\sigma_c / \sigma_t - 1)}{\sqrt{(\sigma_c / \sigma_t - 1)^2 + \sigma_c / \sigma_t}}$$

(2.25)

In the case of triaxial extension, the limit of the initial slope as the uniaxial compressive to tensile strength ratio tends to infinity is 2.5.

Hence, regardless of the ratio of uniaxial compressive strength to tensile strength, the initial slope of the Christensen failure envelope is always less than 4 in triaxial compression and less than 2.5 in triaxial extension. However, as it was shown in Figs. 2.4 and 2.7 for chert dyke and Westerly granite, the measured strength data can be along a curve with much higher slopes. In these cases, the Christensen criterion cannot capture the trend of data.

In order to put the problem in context, it is useful to determine the slope of the well-established Hoek-Brown failure envelope. The initial slope of the Hoek-Brown envelope for intact rock at $\sigma_3 = 0$ in triaxial compression and extension states of stress can be calculated from Eq. (2.18) as:

$$\left(\frac{d\sigma_1}{d\sigma_3}\right)_{\sigma_3=0} = 1 + \frac{m}{2}$$

(2.26)

22

Substituting Eq. (2.20) into Eq. (2.26) gives:

$$\left(\frac{d\sigma_1}{d\sigma_3}\right)_{\sigma_3=0} = 1 + \frac{1}{2}\left[\frac{\sigma_c}{\sigma_t} - \frac{\sigma_t}{\sigma_c}\right]$$

(2.27)

Hence, there is no mathematical upper bound for the initial slope of the Hoek-Brown criterion.

Table 2.6 shows the calculated values of initial slope for the Christensen and Hoek-Brown criteria using the σ_c and σ_t values obtained from fitting to all strength data for each rock type. It can be seen that for the cases of chert dyke and Westerly granite, the Christensen criterion has reached the maximum values of 4 and 2.5 for triaxial compression and extension, respectively. On the other hand, the Hoek-Brown criterion has been able to produce the high initial slopes of 10.65 and 16.89 required to fit the data for the chert dyke and Westerly granite, respectively. This explains the significantly lower error values of the Hoek-Brown criterion for these rocks (Table 2.5).

Table 2.6 The initial slope of the best fit failure envelopes for different rock types

Rock type	Christensen criterion		Hoek-Brown criterion
	Triaxial compression	Triaxial extension	Triaxial compression & extension
Synthetic rock	3.16	2.35	3.47
Chert dyke	**4.00**	**2.50**	10.65
Carrara marble	3.35	2.39	5.55
Westerly granite	**4.00**	**2.50**	16.89

The reason for obtaining zero values of tensile strength from fitting analyses of the strength data for chert dyke and Westerly granite is closely related to the limitation of the slope of the failure envelope for the Christensen criterion. While no tensile strength data for these rock types are used in the fitting analyses, the criterion tries to reproduce the trend of data with high slopes by decreasing the value of the tensile strength to zero. As discussed, even a tensile strength of zero, equivalent to an infinite ratio of uniaxial compressive strength to tensile strength, is not sufficient to produce the required high slopes of the failure envelopes. The reason why this problem is not encountered in fitting the triaxial compression data for the synthetic rock is that the Christensen criterion is able to reproduce the required slope for that weak material. However, this is not the case for many real rock types simply because of the inherent limitations in the formulation.

As noted above, for the synthetic rock and Carrara marble, the values of tensile strength for the Christensen criterion obtained from the analyses of data were more accurate than those of the Hoek-Brown criterion. This is because of the tension cut-off which implies the determination of tensile strength based on a few data in the tensile region rather than the whole data set. In other words, since two fitting process are required for the Christensen criterion, one for the linear tension cut-off part and one for the main parabolic part, the

tensile strength obtained from the fitting process is quite accurate provided that enough data are available in the tensile region.

The results of analysis of data for Westerly granite shows an interesting point about how the Christensen and Hoek-Brown criteria handle the effect of intermediate principal stress in polyaxial loading condition. As mentioned before, while the intermediate principal stress is included in the equations of the Christensen criterion, the original form of Hoek-Brown criterion used in this study does not take into account the effect of intermediate principal stress. Considering that the strength data for Westerly granite (Fig. 2.7) clearly show the significant effect of intermediate principal stress on strength, it may be concluded that the Christensen criterion has an obvious advantage and can better fit the polyaxial data. However, as shown in Fig. 2.7, this is not the case.

Similar results have been reported by Colmenares and Zoback (2002) who conducted a comprehensive comparative study between seven different failure criteria. They showed for example that the criteria such as Mohr-Coulomb or Hoek-Brown which are independent of the intermediate principal stress can better predict the polyaxial strength of some rocks compared to the criteria which do take into account the effect of intermediate principal stress such as the Dracker-Prager (1952) or Mogi (1971) criteria.

The key to understanding the reason for such seemingly surprising outcome lies in the way different criteria deal with the intermediate principal stress. The Christensen or Dracker-Prager criteria, for example, are expressed solely in terms of the stress invariants I_1 and J_2, and the σ_2 term is included in these invariants. For such criteria, the cross sections of the failure surface in the π-plane are circles. However, it is long-established that the experimentally determined π-plane representations of failure surfaces for rocks are triangular with smoothly rounded edges (e.g., Kim and Lade, 1984). As an example, π -plane representations of the results of polyaxial tests carried out by Mogi (1971) on samples of Mizuho trachyte are presented in Fig. 2.8. It shows the experimental envelope as well as the circumscribed and inscribed Christensen envelopes fitted to triaxial compression and extension data, respectively. It can be seen that the data points are aligned on a rounded triangular failure envelope and the Christensen criterion with circular cross sections cannot adequately reproduce the trend of data.

Finally, the reliability of the brittle to ductile transition condition for the Christensen criterion should be examined. As described in Section 2.2, according to the Christensen criterion the brittle or ductile behavior of a given material depends only on the volumetric stress, and there is a threshold of volumetric compressive stress above which the behavior is completely ductile. As an example, Fig. 2.1b showed that for a typical rock material with $\sigma_c/\sigma_t = 12$, the predicted mode of failure in triaxial compression with confining pressure from zero to infinity is ductile failure. In other words, the Christensen criterion makes no provision for the brittle failure of rock under compressive stress.
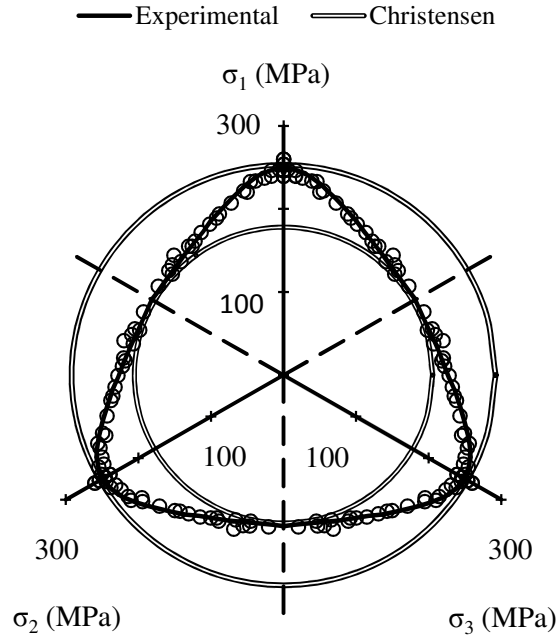
Fig. 2.8 The results of polyaxial test on Mizuho trachyte at I_1 = 506 MPa, experimental envelope (rounded triangular) and the Christensen envelopes (circular)

However, this contradicts the observed behavior of rocks. By studying the failure characteristics of different rock types, Mogi (1971) showed that as long as the ratio of σ_1/σ_3 at failure is less than about 3.4, brittle failure occurs in triaxial compression. In other words, the brittle to ductile transition threshold of rock materials depends on the ratio of principal stresses rather than on the volumetric stress, and brittle failure is the dominant mode of failure in triaxial compression with low to intermediate levels of confining pressure.

As an example, the results of triaxial tests carried out by Schwartz (1964) on Indiana limestone are shown in Fig. 2.9. The measured values of uniaxial compressive and tensile strength for this rock are 41.4 and 2.5 MPa, respectively. It can be observed that the brittle to ductile transition line proposed by Mogi (1971) accurately predicts the brittle and ductile failure of Indiana limestone. On the other hand, the brittle to ductile transition condition proposed by Christensen predicts ductile mode of failure in triaxial compression with confining pressure greater than zero. Contrary to the experimental observations, the Christensen criterion makes no provision for the brittle failure of rocks under compressive stresses.

The reason for this contradiction may be attributed to different definitions of brittle and ductile failure. The brittle failure in the context of the Christensen criterion is closely related to tensile failure and the intersection of the tension cut-off with the main failure surface. However, brittle failure in rock mechanics is related to post-failure strain softening behavior in compressive stress fields.
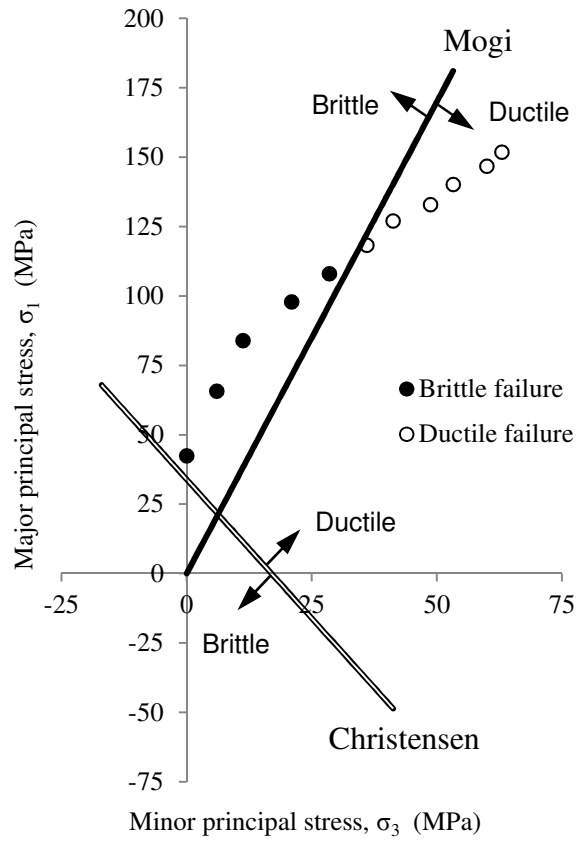
Fig. 9 The results of triaxial test on Indiana limestone, observed behavior of rock and the brittle to ductile transition lines proposed by Mogi and Christensen

2.6. Conclusions

The Christensen criterion was discussed in detail and explicit equations were derived for biaxial, triaxial compression, triaxial extension, and polyaxial loading conditions. The results laboratory tests on a synthetic rock, chert dyke, Carrara marble and Westerly granite were used to evaluate the accuracy of the Christensen criterion compared to the well-established Hoek-Brown criterion.

On average, the Christensen criterion led to 65% higher errors compared to the Hoek-Brown criterion. The slope of the Christensen failure envelope was found to be significantly lower than the experimental data. It was proved that the maximum initial slope for the Christensen failure envelope is 4 in triaxial compression and 2.5 in triaxial extension. However, the initial slopes of over 16 were produced by the Hoek-Brown criterion to replicate the trend of experimental data.

Although the intermediate principal stress appears in the equations of the Christensen criterion, it did not fit the polyaxial strength data of Westerly granite as well as the Hoek-Brown criterion which does not take into account the effect of intermediate principal stress.

The reason for such phenomenon was discussed in terms of the circular cross sections of the Christensen failure surface in the π-plane which is inconsistent with the smooth triangular shapes obtained from experiments.

The brittle to ductile transition condition predicted by the Christensen criterion was also found to be inconsistent with the observed behavior of rocks. It was concluded that the Christensen criterion has some inherent mathematical characteristics which limits its potential for predicting the strength of rocks in compression.

References

Al-Ajmi, A. M., Zimmerman, R. W. (2005), Relation between the Mogi and the Coulomb failure criteria, Int. J. Rock. Mech. Min. Sci., 42, 431–439.

Benz, T., Schwab, R. (2008), A quantitative comparison of six rock failure criteria, Int. J. Rock. Mech. Min. Sci., 45, 1176–1186.

Benz, T., Schwab, R., Kauther, R. A., Vermeer, P. A. A. (2008), Hoek–Brown criterion with intrinsic material strength factorization, Int. J. Rock. Mech. Min. Sci., 45(2), 210–22.

Christensen, R. M. (1997), Yield functions/failure criteria for isotropic materials, In: Proceedings of Mathematical, Physical and Engineering Sciences, Vol. 453, London: The Royal Society, p. 1473-1491.

Christensen, R. M. (2000), Yield functions, damage states and intrinsic strength, Math. Mech. Solids, 5,285-300.

Christensen, R. M. (2004), A two property yield, failure (fracture) criterion for homogeneous, isotropic materials, J. Eng. Mater. Tech., 126, 45-52.

Christensen, R. M. (2005), Exploration of ductile, brittle failure characteristics through a two parameter yield/failure criterion, Mater. Sci. Eng. A, 394, 417-424.

Christensen, R. M. (2006a), Yield Functions and Plastic Potentials for BCC Metals and Possibly Other Materials, J. Mech. Mater. Structs.,1,183-200.

Christensen, R. M. (2006b), A comparative evaluation of three isotropic, two property failure theories, J. Appl. Mech., 73, 852-859.

Christensen, R. M. (2007), A comprehensive theory of yielding and failure for isotropic materials, J. Eng. Mater. Tech., 129, 173-181.

Colmenares, L. B., Zoback, M. D. (2002), A statistical evaluation of intact rock failure criteria constrained by polyaxial test data for five different rocks, Int. J. Rock. Mech. Min. Sci., 39, 695–729.

Drucker, D., Prager, W. (1952), Soil mechanics and plastic analysis or limit design. Quart Appl Math, 10:157–165.

Haimson, B., Chang, C. (2000), A new true triaxial cell for testing mechanical properties of rock, and its use to determine rock strength and deformability of Westerly granite, Int. J. Rock. Mech. Min. Sci., 37, 285–296.

Hammah, R. E. Carvalho, J. L. (2011), An introduction to the Christensen criterion – An answer to true, representative modelling of intact rock yielding/failure?, In: CD-Rom Proceedings of the International Symposium on Rock Slope Stability in Open Pit Mining and Civil Engineering, Vancouver, BC.

Hoek, E. (1965), Rock fracture under static stress conditions, Ph.D. thesis, The Faculty of Engineering, Univ. of Cape Town, South Africa.

Hoek, E. Brown, E. T. (1980), Empirical strength criterion for rock masses, J. Geotech. Eng. Div., ASCE 106(GT9), 1013-1035.

Hoek, E. (1983), Strength of jointed rock masses, 23rd Rankine Lecture, Géotech, 33(3), 187-223.

Hoek, E. (1990), Estimating Mohr-Coulomb friction and cohesion values from the HoekBrown failure criterion, Int. J. Rock Mech. Min. Sci. Geomech. Abst, 12(3), 227-229.

Hoek, E. Wood, D. Shah, S. (1992), A modified Hoek-Brown criterion for jointed rock masses, In: Proc. Rock Characterization Symp., Int. Soc. Rock Mech.: Eurock '92, J. Hudson ed, 209-213, London: British Geotechnical Society.

Hoek, E. Brown, E. T. (1997), Practical estimates of rock mass strength, Int. J. Rock. Mech. Min. Sci., 34, 1165-1186.

Hoek, E. Carranza-Torres, C. and Corkum, B (2002), Hoek-Brown failure criterion – 2002 Edition, In: Proceedings of NARMS-TAC Conference, Toronto, ON, p. 267-273.

Howarth, D. F. Rowlands, J. C. (1987), Quantitative assessment of rock texture and correlation with drillability and strength properties, Rock. Mech. Rock. Eng., 20, 57-85.

Jaeger, J. C. Cook, N. G. W. (1979). Fundamentals of rock mechanics. 3rd edition, London: Chapman and Hall.

Johnson, B. Friedman, M. Hopkins, T. W. (1987), Strength and microfracturing of Westerly granite extended wet and dry at temperatures to 800°C and pressures to 200 MPa, In: Proceedings of the 28th U.S. Symposium on Rock Mechanics (USRMS), Tucson, AZ, p. 399-412.

Kim, M. K., Lade, P. V. (1984), Modelling Rock Strength in Three Dimensions, Int. J. Rock Mech. Min. Sci., 21, 21-33.

Krech, W. W. Henderson, F. A. and Hjelmstad, K. E. (1974), A standard rock suite for rapid excavation research, Bureau of Mines Report of Investigations No. 7865, 29 p.

Mogi, K. (1971), Fracture and flow of rocks under high triaxial compression, J. Geophys. Res., 76, 1255–1269.

Nguyen, Si-H. Chemenda, A. I. Ambre, J. (2011), Influence of the loading conditions on the mechanical response of granular materials as constrained from experimental tests on synthetic rock analogue material, Int. J. Rock Mech. Min. Sci., 48, 103-115.

Pan, X. D., Hudson, J. A. (1988), A simplified three dimensional Hoek–Brown yield criterion. In: Romana M (ed) Rock mechanics and power plants. Rotterdam: Balkema, , pp 95–103.

Priest, S. D. (2005), Determination of shear strength and three-dimensional yield strength for the Hoek–Brown yield criterion. Rock. Mech. Rock. Eng. 38(4), 299–327.

Rafiei, H. (2011), New empirical polyaxial criterion for rock strength, Int. J. Rock. Mech. Min. Sci., 48, 922–931.

Ramsey, J. M. Chester, F. M. (2004), Hybrid fracture and the transition from extension fracture to shear fracture, Nature, 428, 63-66.

Zhang, L., Zhu, H. (2007), Three-dimensional Hoek–Brown strength criterion for rocks, J. Geotech. Geoenvir. Eng. ASCE. 133(9), 1128–1135.

Chapter 3

Back-analysis of rock mass displacements around a deep shaft using two- and three-dimensional continuum modeling [2]

3.1. Introduction

Predicting the behavior of rock masses is a necessary part of rock engineering design. Over the years, various empirical and numerical approaches have been developed to address the problem. Discontinuum modeling approaches emphasize the fractured nature of rock masses and can capture the discontinuous displacement fields resulting from relative movement of individual blocks. On the other hand, continuum modeling approaches consider the rock mass as an equivalent continuum with degraded mechanical properties due to the presence of fractures.

Back analysis procedures can be divided into two main categories of inverse and direct approaches (Cividini et al. 1981). In the inverse approach, the governing equations of the problem are inverted so that the model response is given and model parameters are calculated. While this approach can be more computationally efficient, the inverse equations can only be obtained for relatively simple problems where the material behavior and specified model response are straightforward. In addition, this approach needs fundamental change to the numerical codes which is not usually possible. In the direct approach, however, a series of ordinary analyses are carried out without need for any changes into the numerical code. In addition, there is no limitation in terms of the complexity of the problem in the direct approach. While the trial and error process for adjusting the model and parameters in the direct approach can be more computationally intensive, it is a more comprehensive and flexible methodology (Gioda and Maier 1980; Miranda et al. 2011; Sakurai and Takeuchi 1983). Therefore, the direct approach is widely used for back analyses of real-world engineering problems.

The first step in the back analysis is to choose between continuum and discontinuum models. Although from physical point of view, the discontinuum models can represent the fractured nature of rock masses more realistically, the number of input parameters required

---

for these analyses including the mechanical properties of intact rock as well as the location, orientation, spacing and mechanical properties of the joints is very large. This in turn significantly increases the uncertainties in the model and the none-uniqueness of the solution. From computational point of view, it is also not feasible to incorporate all the joints in the discontinuum analyses and a vast majority of the joints are filtered subjectively (e.g. Vardakos et al. 2007). In addition, while the assumptions in two dimensional discontinuum analyses such as those regarding the orientation of joints or incorporating three-dimensional effects are seldom valid/verified, three dimensional discontinuum analyses involve prohibitively long run times. Therefore, discontinuum models are not generally recommended for back analysis (e.g. Yazdani et al. 2012).

On the other hand, continuum analyses require smaller number of parameters which means less uncertainty. In addition, three dimensional models can be solved in a reasonable time period. Keeping in mind the importance of three dimensional effects (as always a portion of the response prior to installation of instrumentation is lost and should be accurately taken into account) and manageable run time (as many trial and errors are required to adjust the model parameters), continuum models can be used more effectively and efficiently in the back analysis of closely jointed rock masses where the overall behavior rather than local structurally controlled responses is concerned.

Recent high quality laboratory and extensometer data collected for a deep shaft project provided an opportunity to examine the ability of current continuum-based models and methods for predicting and back-analyzing the rock mass behavior. In the following sections, the back analysis methodology for the shaft response using direct procedure is presented. The measured displacements are processed and numerical analyses are carried out. The numerical codes FLAC3D (Itasca Inc. 2009) based on Finite Difference Method (FDM) and Phase2 (Rocsceince Inc. 2011) based on Finite Element Method (FEM) were used in this study. Comparison has been made between the obtained rock mass parameters from the back analysis and those estimated from current empirical methods.

3.2. Project description

A shaft is currently being excavated to a depth of more than 2 km beneath the ground surface. As with all projects at this depth there is a strong reliance on empirical methods and data obtained from borehole characterization techniques to forecast the rock mass response during shaft sinking. At strategic depths borehole multipoint extensometers were installed to monitor the rock mass response around the 10 m diameter circular shaft. The extensometer data used in this paper was obtained at the depth of 1172 m. The rock formation at this depth was composed of Cretaceous volcanic sediments. The laboratory mechanical properties of the intact rock from this formation were obtained from 32 uniaxial compression tests, 29 triaxial compression tests and 8 Brazilian indirect tension tests. The intact rock parameters including the uniaxial compressive strength σ_{ci}, Young's modulus E and Poisson's ratio ν from the uniaxial tests, Hoek-Brown parameter m_i from the triaxial tests, and tensile strength σ_t from the Brazilian tests are shown in Table 3.1.

Characterization of the rock mass was carried out using the Geological Strength Index (GSI) system. The value of GSI obtained for the formation was 62. The hydraulic fracturing and over-coring methods were used to determine the in situ stress field at the site. The obtained magnitude and orientation of the in situ principal stresses are shown in Table 3.2.

Table 3.1 Mechanical properties of intact rock in the formation

Parameters	σ_{ci} (MPa)	E (GPa)	v	m_i	σ_t (MPa)
Values	104	42	0.21	30	5.9

Table 3.2 In situ stress field at the formation

In situ stress component	Magnitude (MPa)	Orientation
Major in situ principal stress, σ_1	32	Vertical
Intermediate in situ principal stress, σ_2	26	North-South
Minor in situ principal stress, σ_3	16	East-West

The shaft was sunk using a full face drill-and-blast method and a Galloway Stage. The advance length in each excavation round was 3.0 m and every round took about 24 hours. The sequence for each round was drilling, blasting, ventilation, mucking, and shotcrete. The final concrete liner was poured every four rounds when the face has advanced about 12 m and sufficient time is allowed for the rock mass to respond to the excavation.

Shaft instrumentation included monitoring the radial displacements using four multipoint extensometers. The azimuth of extensometers (Ext.) 1, 2, 3, and 4 was 60, 227, 317, and 170 degrees from the North, respectively. Each extensometer has six anchor points at distances of 0.5, 1.0, 1.5, 2.0, 4.0, and 6.1 m from the reference head at the borehole collar. The extensometers were installed at a distance of 1 m from the face of the shaft. The holes for the extensometers were drilled using a jack-leg drill, and were grouted in place using a modified grout mix that could develop 2 MPa compressive strength after a few hours of curing.

Real time logging systems were installed to record the measurements every 5 minutes so that data could be collected during the entire sinking cycles. After installation of the extensometers, drilling for the next round of excavation started. The first blast occurred 22 hours after installation which allowed sufficient time for the grout to cure and for the anchor points to attach to the rock. The second blast occurred about 26 hours after the first blast. The extensometers were left in place just prior to the final liner being poured over the top of the instrumentation. Fig.3.1 shows the configuration of the problem in the three stages of extensometer installation, after the first blast and after the second blast. The layout of extensometers in the horizontal plane is illustrated in Fig. 3.2.
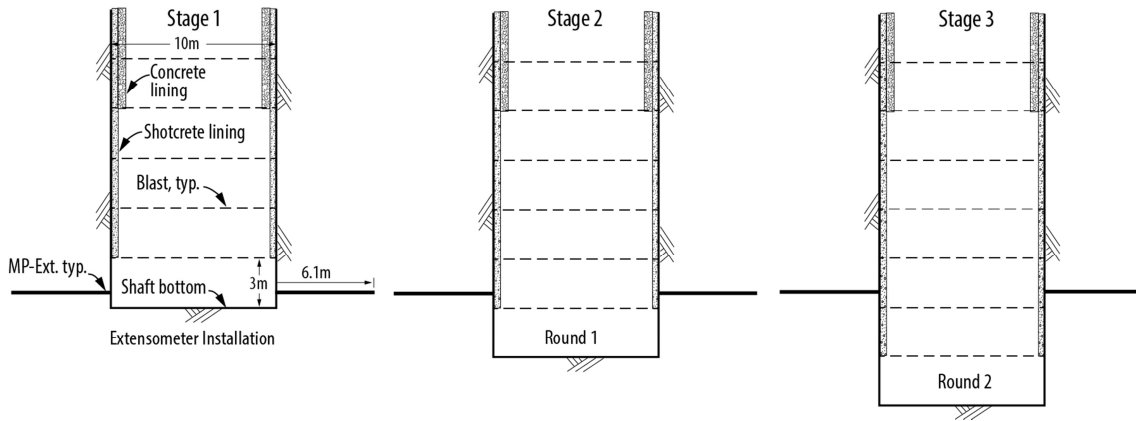
Fig. 3.1 Installation of multipoint extensometers (MP-Ext) and subsequent shaft advances of Rounds 1 and 2
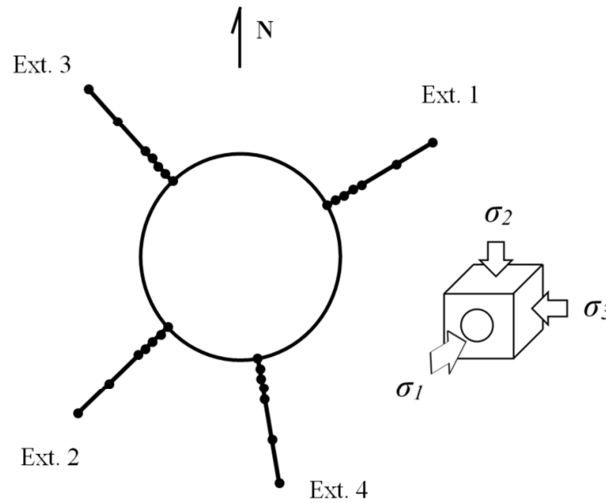
Fig. 3.2 The layout of instrumentation in the shaft

3.3. Extensometer measurements, interpretation and processing

The displacement relative to the deep 6.1m anchor points for each extensometer is shown in Fig. 3.3. The first hours after installation of extensometers is the time when the grout is curing and the displacements recorded in that time period are not reliable. It can be observed that Ext. 2, 3, and 4 show significant displacements into the shaft within the first two hours of measurements. All the anchor points of Ext. 1 show no displacement before the first blast except the 0.5 m anchor point which indicates significant contraction. Before the first blast, no displacement is anticipated from theoretical point of view as the geometry and loading condition has not changed. However, the relative displacement at the reference head (0.0 m), during this period is 0.2, 1.7, 3.9, and 0.3 mm for Ext. 1, 2, 3, and 4 respectively.
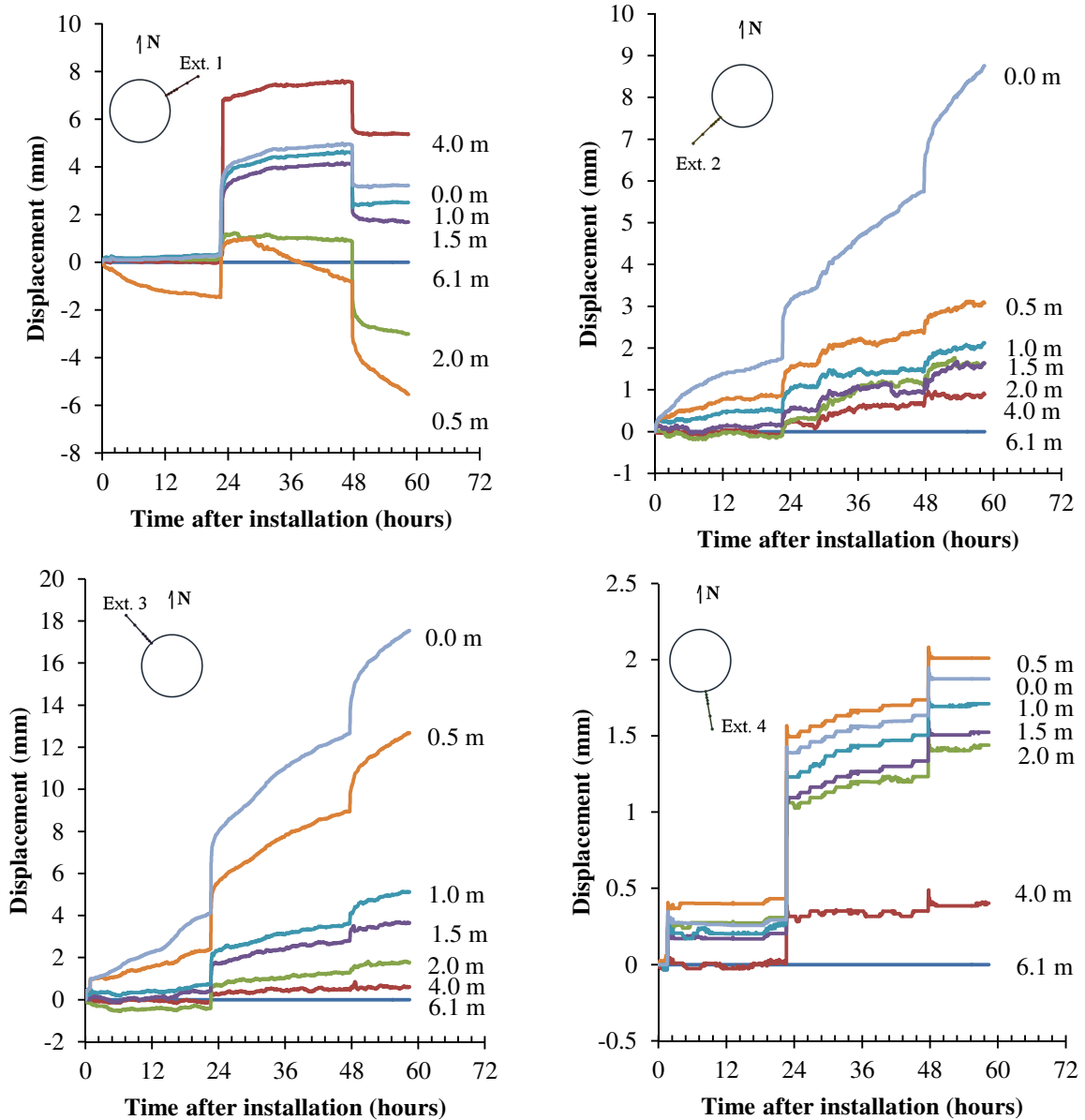
Fig. 3.3 Recorded displacements for each anchor point, relative to the 6.1-m-deep extensometer in the four multipoint extensometers

After the first blast at 22 hours, all the extensometers indicate a sharp increase of displacement into the shaft, which is expected. However, the 4.0 m deep anchor point of Ext. 1 shows about two times the displacement recorded for the reference head at the borehole collar. A few hours after the first blast, the 0.5 m anchor point in Ext. 1 again starts to record contractive displacements.

Following the second blast in 48 hours, Exts. 2, 3, and 4 indicate additional displacement toward the shaft, which is also expected. However, all the anchor points of Ext. 1 now show very similar amount of increase in contractive displacement.

Another important point about the recorded displacements shown in Fig. 3.3 is the time dependent response. It can be observed that Ext. 2 and 3 show very significant time dependent behavior after each blasting which does not come to equilibrium in 24 hours. However, Ext. 1 and 4 generally show very minor amount of time dependent displacement. It is also interesting to note that the Ext. 2 and 3 which indicate significant time dependent response happen to be on the west side of the shaft while the Ext. 1 and 4 recording negligible time dependent behavior are on the east side.

The main potential sources of time dependent response for the shaft were considered as thermal effects, creep of the intact rock, and gradual slip along the joints. While the initial rock temperature at the 1172 m depth of the instrumentation section had been about 57 °C, the shaft temperature at the time of excavation was 31 °C. Hence, the rock mass experiences a cooling trend. However, it can be intuitively observed that a decrease of temperature inside the shaft should result in outward displacement of the shaft wall while the time dependent behavior recorded by Ext. 2 and 3 indicate inward displacements. In addition, the thermal effects should influence the displacements in all directions while only the extensometers in the west side of the shaft showed a time-dependent response. Preliminary thermo-mechanical analyses confirmed that not only the time dependent displacement due to thermal cooling should be in outward direction but also the magnitude of the displacement due to thermal cooling is much lower than those recorded. Creep of intact rock was another potential source of time dependent response. However, nature of the formation and laboratory tests on intact specimens did not provide any evidence for creep behavior of this rock type. A possible explanation for the recorded time-dependent behavior may be the gradual slip along the joint due to activities inside the shaft.

Since continuum modeling was chosen in this study for the back analysis to evaluate the global elasto-plastic characteristics of rock mass rather than the time dependent behavior or movement along individual joints, it was necessary to pre-process the extensometer measurements and filter the time dependent effects. Fig. 3.4 shows the processed displacement profiles which exclude the time dependent deformations.

It can be readily observed that the displacement profile obtained for Ext. 1 shows significant scatter when compared to the other extensometers.   In addition the displacements caused by the second round blast are less than those associated with the first round blast. Hence, it was concluded that the results from Ext. 1 are unreliable and excluded from the back analysis. The displacement profiles for Ext. 2 and 3 follow a typical trend for an elasto-plastic medium with a low slope at the deep elastic region and high slope at the plastic region in the vicinity of the shaft. The displacement profile for Ext. 4 closely follows a linear trend except within the 0.5 m of the shaft boundary.
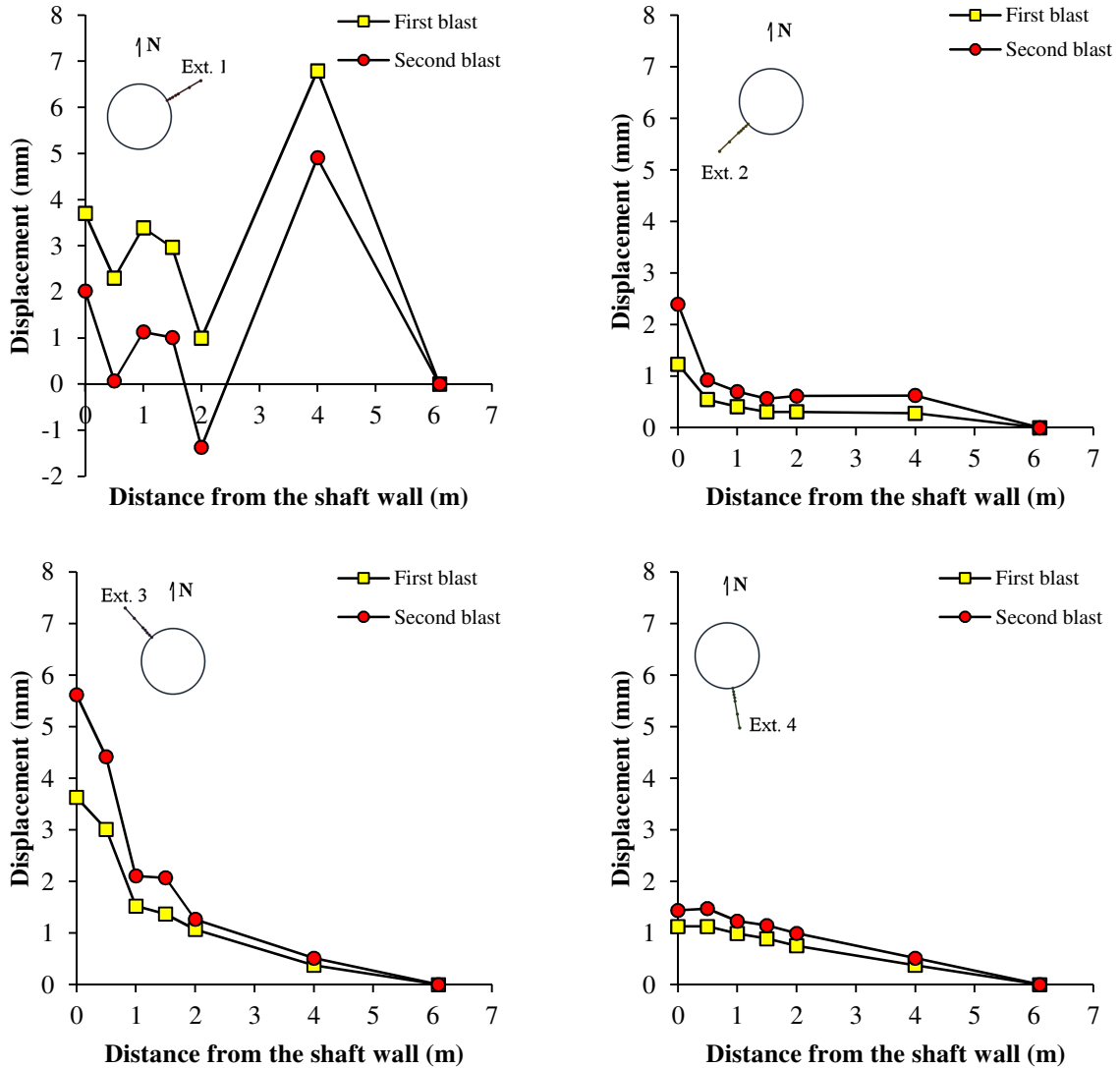
Fig. 3.4 The processed displacement profiles for different extensometers

3.4. Back analysis of the shaft response

Direct approach of back analysis along with a continuum representation of the rock mass was used in this study. In the direct approach, an error function is defined and minimized in an iterative process by adjusting the model parameters. The process starts with an "initial guess", initial set of parameters which will be subsequently adjusted. A good initial guess can lower the number of required trial and errors thereby increasing the efficiency of the back analysis process. Root Mean Squared Error (RMSE) in prediction of displacements was used in this study as the error function to be minimized. Empirical relationships were used to provide a good starting point for the back analysis process.

3.4.1.   Orientation of maximum horizontal stress

The in-situ stress measurements indicated the maximum horizontal stress was oriented approximately North-South. Such an orientation implies that the maximum elastic radial displacements in the shaft would also be oriented North-South and the maximum plastic radial displacements would be found in the East-West regions of the shaft. Inspection of Ext. 2, 3 and 4, tends to support this general trend. If the direction of the maximum horizontal stress was exactly North-South, symmetry implies that only a quarter of the problem domain, say the North-East quarter, needs to be modeled. In the quarter model, Ext. 2 and 3 are at Azimuths 047° and 043°, respectively. The angular separation of only 4° for Ext. 2 and 3 implies that the displacements based on quarter symmetry models should be very similar.   However, inspection of Ext. 2 and 3 reveals that the deformations recorded by Ext. 3 are more than two times the deformations recorded by Ext. 2. This implies that North-South orientation of the maximum horizontal is likely inaccurate.

Preliminary sensitivity analyses using a simple elasto-plastic two dimensional model showed that by rotating the maximum horizontal stress from Azimuth 000 to Azimuth 010, the radial displacement trends were in better agreement with trends from Ext. 2 and 3. This rotation of 10 degrees is well within the confidence of the in-situ stress measurements. Hence, this modified direction of in situ principal horizontal stresses was used in the analyses discussed in the following sections.

3.4.2.   Three dimensional back analysis using FLAC3D

Capturing the three-dimensional effects of face advancement on the measured displacements requires a three-dimensional numerical tool that can track the staging sequences used during shaft construction. FLAC3D (Itasca Inc. 2009) is a widely used FDM code for geotechnical engineering analyses which offers sufficient flexibility for simulating the various construction stages. The numerical simulation followed the actual shaft-sinking sequence. Sensitivity analyses showed that the shotcrete support and final concrete lining did not influence the radial displacements and the extent of plastic zone. Hence, the support was excluded from the back-analyses to increase the computational efficiency. In addition, it is well known that the results from numerical plasticity analysis are mesh dependent. For our analysis, the mesh size was selected based on computational efficiency and a series of sensitivity analyses to insure the accuracy of 98% for elastic solutions. A minimum element size of 13 cm was used in the radial direction for all analyses when evaluating the results from various model input parameters.

In order to extract the data from the numerical analysis and compare it to the extensometer measurements, two corrections need to be applied. The first temporal correction is necessary to remove the displacements that occur before the installation of the extensometers. Hence, the displacements in the numerical model at the time of extensometer installation should be recorded and subtracted from the displacements at the subsequent stages. The second spatial correction is necessary to respect the fact that the

extensometers only record the change in length rather than the absolute deformation. Considering the deepest extensometer anchor as the reference point, the displacement at this anchor points should be recorded and subtracted from the displacements recorded by the other anchor points. It should be emphasized that both of these correction are necessary and should be applied in order.

Empirical guidelines and relationships provide a good starting point for choosing the material model and associated parameters. Based on the suggestion of Hoek and Brown (1997) for average quality rock masses, a strain-softening model was assumed for the post-peak behavior. The Mohr-Coulomb material model was adopted for the rock mass with the rock mass modulus estimated from the relationship proposed by Hoek and Diederichs (2006), and the Poisson's ratio estimated from the guidelines by Hoek and Brown (1997). The peak strength parameters including cohesion, friction angle and tensile strength were obtained from the generalized Hoek-Brown criterion (Hoek et al. 2002) using the mechanical parameters of the intact rock given in Table 3.1 and the GSI value of 62 for the rock mass. The dilation angle for average quality rock masses is estimated as 25% of the peak friction angle (Hoek and Brown 1997).

The residual strength parameters are suggested to be estimated based on a reduced GSI value. Cai et al. (2007) proposed a negative exponential function for estimation of the residual GSI value. According to this relationship, the residual GSI for the formation is estimated as 44% of the peak GSI value. This value was used for estimation of the residual strength parameters. The mechanical parameters of rock mass including modulus of deformation E_m, Poisson's ratio v_m, peak cohesion c_p, peak friction angle φ_p, tensile strength σ_{tm}, residual cohesion c_r, residual friction angle φ_r, and dilation angle ψ_m estimated from the empirical methods are given in Table 3.3. The FLAC3D model with this set of parameters is referred to as the model I in this paper.

Table 3.3 Mechanical properties of rock mass for the formation estimated from the empirical methods and back analysis

Model	Reasonable match	Parameters							
		E_m(GPa)	v_m	c_p(MPa)	φ_p(deg)	σ_{tm}(MPa)	c_r (MPa)	φ_r (deg)	ψ_m (deg)
Model I	Ext. 2, 4	24	0.25	5.7	48	0.2	3.3	38	12
Model II	Ext. 3	27	0.25	5.5	40	2.0	0.9	39	15
Model III	Ext. 2, 3, 4	27	0.25	6.0	43	2.0	0.8	41	17

Fig. 3.5 shows the displacement profiles, yielded elements and contours of plastic shear and tensile strains for model I. It can be observed that there is fairly good agreement between the measured and calculated displacement profiles for Ext. 2 and 4. However, the displacements measured by Ext. 3 are significantly underestimated by the numerical model.
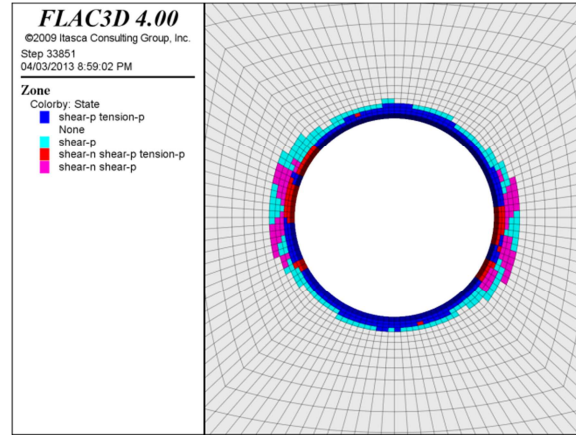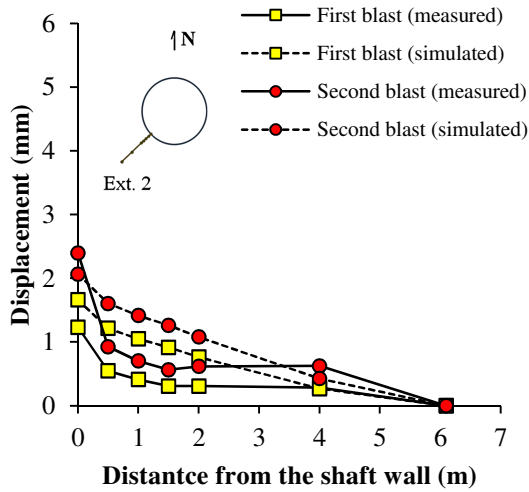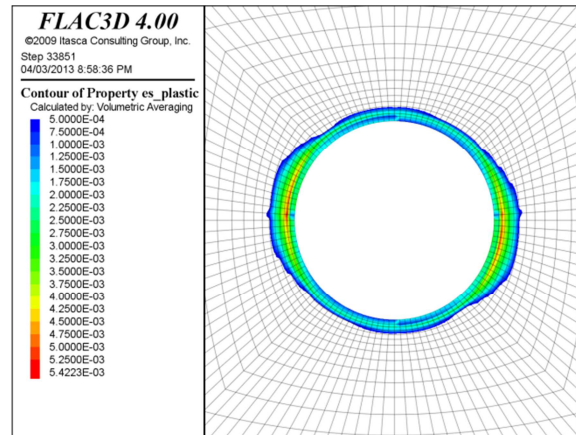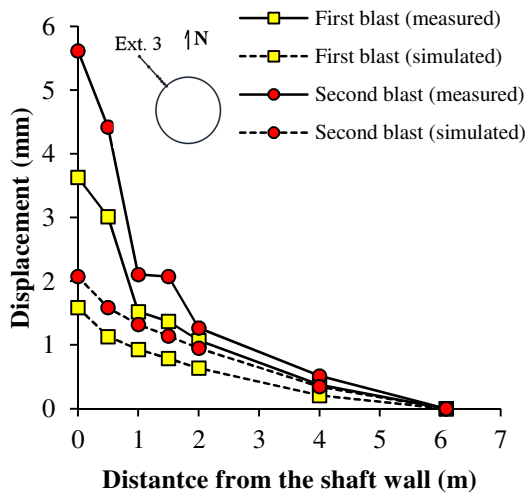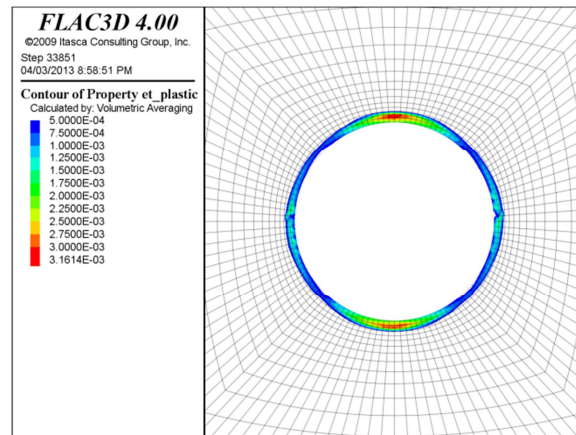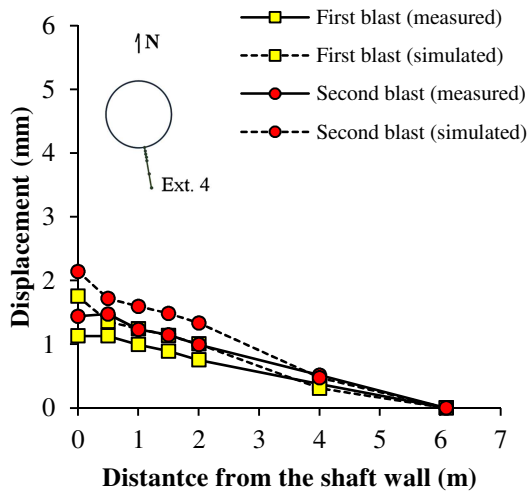
Fig. 3.5 Displacement profiles, yielded elements, and shear and tensile plastic strains for the FLAC3D model I

Contours of yielded element indicate that the maximum thickness of plastic zone is 1.0 m in the direction of minor horizontal stress and minimum thickness of plastic zone is 0.7 m in the direction of maximum horizontal stress. However, the contours of plastic shear and tensile strains indicate that the overall maximum and minimum thickness of plastic zone are 0.9 and 0.4 m in the directions of minimum and maximum horizontal stresses, respectively.

In the following numerical back analyses, the mechanical parameters of the rock mass given in Table 3.3 were optimized to achieve reasonable agreement with the measurements from all three extensometers. However, all the attempts were not completely successful because the displacements recorded with Ext. 3 were much higher than those recorded by the other extensometers and the numerical models were not able to able to reproduce that amount of difference. As a result, the models which gave fairly good match with Ext. 2 and 4 significantly underestimated the displacements for Ext. 3 and those which gave good match to Ext. 3 significantly overestimated the displacements for the other extensometers.

While it was not possible to match the displacements of all the extensometers with a single set of parameters, it was decided to determine the possible range in input parameters. Since model I with the empirically estimated parameters provided reasonable match to Ext. 2 and 4, more focus was given to the measurements of Ext. 3 in the subsequent back analysis to find the set of parameters giving a reasonable match to these data.

The FLAC3D model matching the measurements of Ext. 3 is referred to as the model II in this paper and the parameters are given in Table 3.3. The corresponding displacement profiles, yielded elements, and the plastic shear and tensile strains are shown in Fig. 3.6. While this model provided a reasonable match to the Ext. 3 displacements, it significantly overestimated the displacements for Ext. 2 and 4. Developing a fit to the large displacements near the tunnel profile resulted in a larger plastic zone relative to model I. It is also worth noting that the extent to plastic zone indicated by the contour of yielded elements is larger than that obtained by considering the contour of plastic shear and tensile strains. While the minimum thickness of plastic zone in the direction of major horizontal stress is 2.2 m based on the contour of yielded elements, contours of plastic strains indicate the lower value of 1.7 m. For comparison, the results of three dimensional back analysis with the finite element code ABAQUS is given in Appendix A.

3.4.3.   Two dimensional back analysis using Phase2

Two dimensional plane-strain analyses are often used to avoid the difficulties with three dimensional modeling. For the problem of an advancing tunnel or shaft, the convergence-confinement method (e.g. Hoek and Brown 1980; Carranza-Torres and Fairhurst 2000) is frequently used to capture the three dimensional effects. The main component of this approach which introduces three dimensional effects into the two dimensional analyses is Longitudinal Displacement Profile (LDP). This profile shows the relative convergence into the opening (the ratio of current convergence to the final convergence) as a function of the distance from the excavation face to the point of interest.
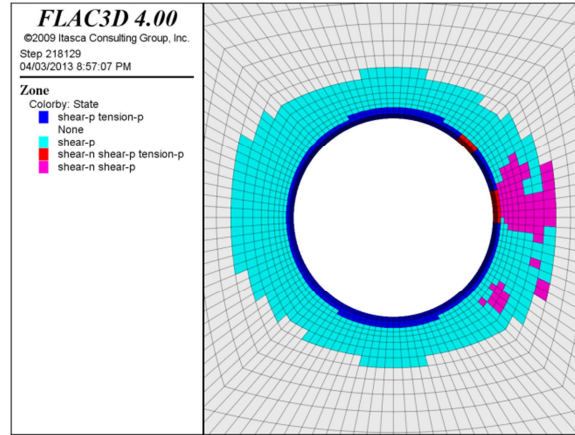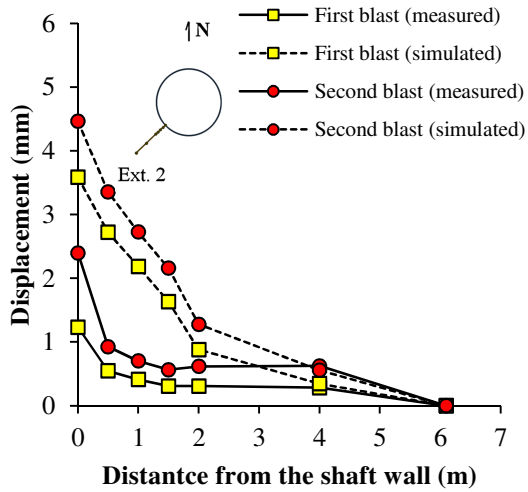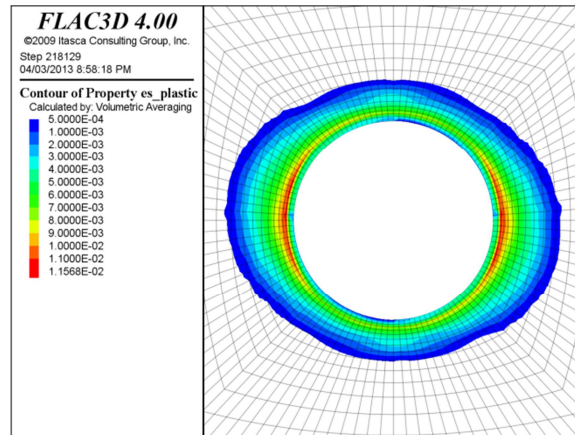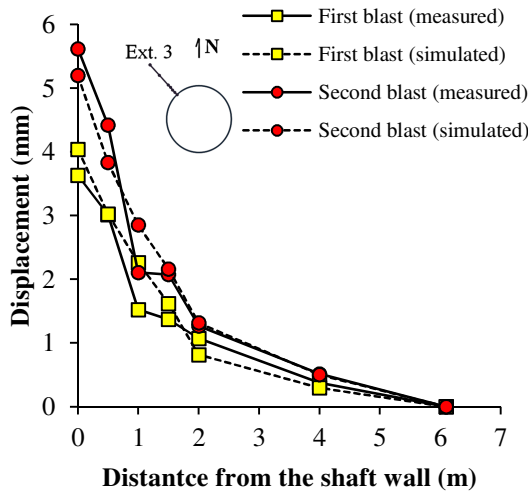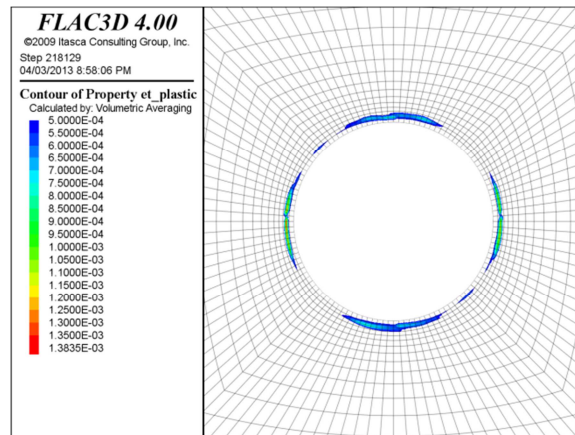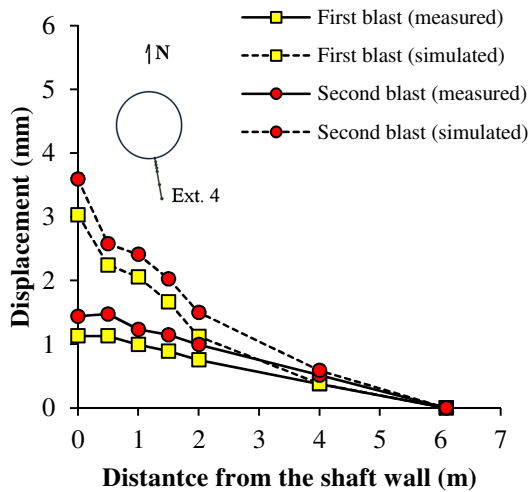
Fig. 3.6 Displacement profiles, yielded elements, and shear and tensile plastic strains for the FLAC3D model II

Several equations have been proposed to describe the LDP for advancing excavations (e.g., Panet 1995; Unlu and Gercek 2003). A more recent set of equations for LDP was developed by Vlachopoulos and Diederichs (2009) based on the results of axisymmetric numerical analyses:

$$\begin{cases} u^* = \dfrac{u}{u_{max}} = u_0^* \exp(X^*) & \text{if } X^* \leq 0 \ (\text{in the rockmass}) \\[4mm] u^* = \dfrac{u}{u_{max}} = 1 - (1 - u_0^*) \exp\left(-\dfrac{3X^*}{2R^*}\right) & \text{if } X^* > 0 \ (\text{in the excavation}) \end{cases}$$

(3.1)

with

$$u_0^* = \frac{u_0}{u_{max}} = \frac{1}{3}\exp\left(-0.15R^*\right)$$

(3.2)

$$X^* = \frac{X}{R}$$

(3.3)

$$R^* = \frac{R_p}{R}$$

(3.4)

where u is the inward radial displacement at the distance of X from the excavation face, u_0 is the displacement at the excavation face (X=0), u_{max} is the maximum displacement far away from the excavation face, u^* is the relative convergence, R is the radius of excavation and R_p is the maximum radius of plastic zone far away from the face (Fig. 3.7).
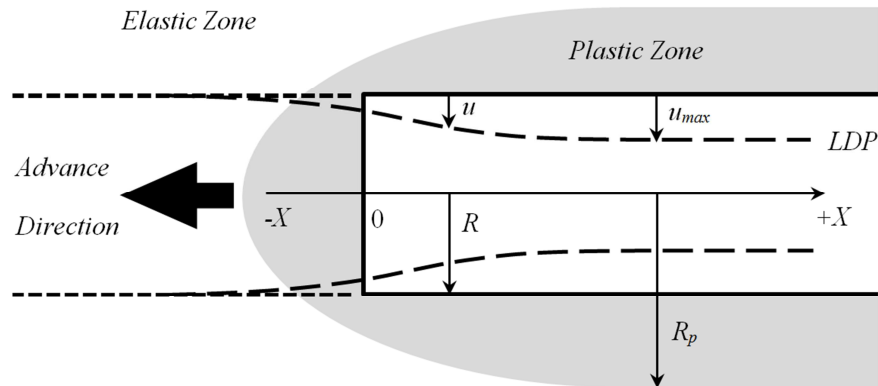
Fig. 3.7 Longitudinal Displacement Profile (LDP) and associated parameter

In this section, the LDP methodology in conjunction with two dimensional modelling using the FEM code Phase2 (RocScience Inc. 2011), was used to back analysis the shaft response. The first step in the analysis was to determine the relative convergence at stage (1) the time

of extensometer installation, stage (2) after the first blast, and stage (3) after the second blast. It can be observed from Eqs. (3.1-3.4) that in order to use the LDP proposed by Vlachopoulos and Diederichs (2009), the maximum radius of plastic zone should be determined. However, it is not exactly known at the beginning of back analysis and an initial assumption is required. Based on the results of trial three dimensional analyses, the thickness of plastic zone is expected to be between 1 and 4 m. Hence, the ratio of plastic zone radius to shaft radius, R^* is between 1.2 to 1.8. Considering the distances of 1, 4, and 7 m from the shaft face at the time of extensometer installation, after the first blast and after the second blast, the ratio of the distance from the face to the shaft radius, X^* is 0.2, 0.8, and 1.4, respectively.

Table 3.4 shows the relative convergence at different stages determined using the Eqs. (3.1-3.4) for LDP proposed by Vlachopoulos and Diederichs (2009). It can be observed that development of larger plastic zones retard the displacement response. The average amounts of convergence at the time of extensometer installation, after the first blast and after the second blast are 40, 67, and 82% of the final convergence, respectively.

Table 3.4 Relative convergence at different stages of analysis based on the LDP proposed by Vlachopoulos and Diederichs (2009)

Stage	Thickness of plastic zone (m)				Average (m)
	1	2	3	4	
(1) Ext. installation, X/R=0.2	0.44	0.41	0.39	0.37	0.40
(2) After the first blast, X/R=0.8	0.73	0.69	0.65	0.62	0.67
(3) After the second blast, X/R=1.4	0.87	0.84	0.80	0.77	0.82

There are two general methods to model the excavation sequence and obtain the ground characteristic curve using two dimensional analyses (e.g. Hoek et al. 2008; Vlachopoulos and Diederichs 2009). Traction relaxation method is a technique in which the tractions on the boundary of excavation are progressively reduced from the in situ values to zero. Another option is the core replacement method in which the Young`s modulus of an inclusion inside the opening is progressively reduced from the initial value to zero. In both cases, the load on the excavation boundary gradually decreases and the convergence progressively increases so that the ground characteristic curve can be determined. The core replacement method is often preferred (e.g. Hoek et al. 2008) due to its ability to better capture the evolution of stresses and development of plastic deformations around non-circular excavations. This method was used in this study.

Different stages of analysis were defined in Phase2 with varying value of Young's modulus for the core inside the shaft. The steps corresponding to extensometer installation, the first blast, and the second blast were determined based on the relative convergences given in Table 3.4. Since the thickness of plastic zone and in turn the relative convergence from the LDP is dependent on the material properties, these values were updated in each trial and error process of back analysis. It was observed that the relative convergence at each step varies for different points along the shaft boundary due to the anisotropic in situ stress field.

Hence, the reference head of Ext. 3 was considered as the main reference point while trying to keep the relative convergence at other points close to the prescribed values.

The mechanical parameters obtained from back analysis using Phase2 are given in Table 3.3 and is referred to as the model III in this paper. The corresponding displacement profiles and contour of yielded elements are shown in Fig. 3.8. It can be observed that this model gives reasonable match to the measurements of all extensometers by slightly overestimating the convergence for Ext. 2 and underestimating the displacements for Ext. 3. Regarding the extent of plastic zone, it is worth noting that the yield symbols show about the length of one element smaller plastic zone relative to the contour of plastic elements. The difference was significant for the preliminary models with triangular elements and graded mesh because the size of elements at the boundary of elastic and plastic zones was relatively large. For the final model with quadrilateral elements and radial mesh, the difference was negligible and the average thickness of plastic zone varies between 1.4 and 2.3 m.

Maximum thickness of plastic zone: 2.3 m
Minimum thickness of plastic zone: 1.4 m
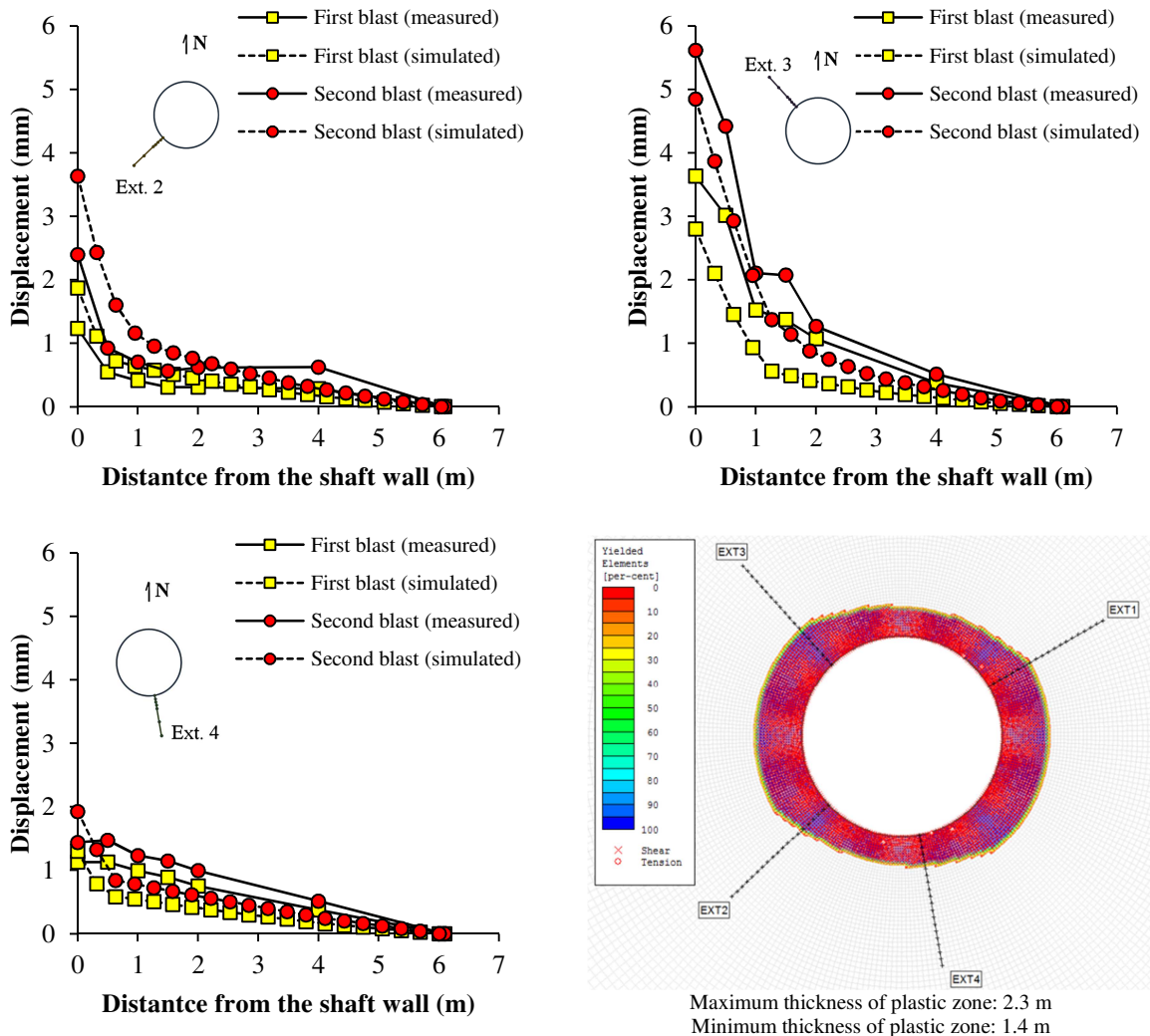
Fig. 3.8 Displacement profiles and equivalent plastic strain for the Phase2 model III

3.5. Discussion

The parameters and results of different numerical models were presented in the previous section. It was shown that the FLAC3D model with the empirically derived strain-softening parameters given in Table 3.3 (model I) gives satisfactory match to the measurements of Ext. 2 and 4 while significantly underestimating the measurements of Ext. 3. Putting more emphasis on Ext. 3, the FLAC3D model with parameters given in Table 3.3 (model II) gives a good fit to the measurements of this extensometer while significantly overestimating the displacements for the other extensometers. The two dimensional Phase2 model with the parameters given in Table 3.3 (model III), however, gives a reasonable match to the measurements of all extensometer. This match is judged acceptable by simply comparing the measured extensometers results with the model results. It is clear from these analyses that the best-fit model parameters are constrained primarily by the number of extensometers used in the back analysis. When limiting the acceptability of the back analysis to the radial displacements the comparison of the predicted and measured is straightforward. However, when combining the extent of the plastic zone and the displacements from each of the models, deciding on an acceptable solution is less clear.

Table 3.5 shows the maximum thickness of plastic zone and displacement of the reference head at the borehole collar measured and simulated for different extensometers. The FLAC3D model I gives the lowest thickness of plastic zone along with lower displacements sufficient to match the measurements of Ext. 2 and 4. The FLAC3D model II shows a much larger plastic zone necessary to cause larger displacements recorded by the Ext. 3. The Phase2 model III indicated an intermediate extent of plastic zone.

Table 3.5 The maximum thickness of plastic zone and displacement of the reference head measured and simulated for different extensometers

Method/Matched Extensometers	Maximum plastic zone (m)	Ext. 2 (mm)		Ext. 3 (mm)		Ext. 4 (mm)	
		1st blast	2nd blast	1st blast	2nd blast	1st blast	2nd blast
Measured	-	1.23	2.40	3.63	5.62	1.13	1.43
Model I/Ext2,4	1.0	1.66	2.06	1.59	2.07	1.75	2.14
Model II/Ext3	2.8	3.57	4.45	4.05	5.21	3.05	3.62
Model III/Ext2,3,4	2.3	1.84	3.60	2.81	4.87	1.31	1.93

It can be observed from Table 3.5 that measured displacement values vary over wide ranges from 1.13 to 3.62 mm and 1.43 to 5.62 mm for the first and second blasts, respectively. For the FLAC3D model I, however, the ranges are very narrow such as 1.59-1.75 mm and 2.06-2.14 mm for the first and second blasts, respectively. Hence, the corresponding ratios of maximum to minimum displacement at the reference head for different extensometers are 1.10 and 1.04 in the first and second blasts, respectively. Similarly for the FLAC3D model II, the ranges are 3.05-4.05 mm and 3.62-5.21 mm for the first and second blasts, making the maximum to minimum ratios of 1.33 and 1.44, respectively.

These results suggest that for the given problem (opening geometry, excavation sequence, support installation, monitoring conditions) with reasonable ranges of material parameters, there is a limit for the ratio of maximum to minimum displacements which can be obtained from the three dimensional continuum models with isotropic constitutive models. Obviously, this limit is influenced by the geometrical and loading anisotropy. In a hydrostatic stress field, the theoretical ratio of maximum to minimum displacements around the boundary of a circular opening is unity and it increases with increasing the anisotropy of the stress fields.

A series of numerical analyses was carried out using FLAC3D with elastic (EL), elastic-perfectly plastic (PP), and strain softening (SS) material models and input parameters ranging from likely to possible values (Table 3.6) to test the hypothesis. The obtained ratio of maximum to minimum displacements at reference head for different extensometers is shown in Fig. 3.9. It can be observed that considering all the elastic, elastic-perfectly plastic, and strain softening material behaviors, the ratio of maximum to minimum displacements at the reference head for different extensometers varies from 1.02 to 1.58. The results of FLAC3D models I and II also fall in this range.

Table 3.6 Range of parameters used for determining the displacement ratios in Fig. 3.9

Range	E_m(GPa)	v_m	c_p(MPa)	φ_p(deg)	σ_{tm}(MPa)	c_r (MPa)	φ_r (deg)	ψ_m (deg)
Min.	20	0.20	3.5	42	0.2	0.5	38	5
Max.	27	0.30	5.8	48	2.0	2.5	48	20

Hence, for the circular shaft with the ratio of minimum to maximum horizontal stresses of 0.6, the measurements of different extensometers based on three dimensional continuum models with isotropic constitutive models should not be different by more than approximately 60%. However, the measured ratios were 3.21 and 3.90 for the first and second blasts, respectively. This implies that regardless of the material model and corresponding parameters, the three dimensional continuum models with isotropic constitutive models simply cannot reproduce the significant difference in the measured displacements by different extensometers. The reason for such a wide range of measured displacements might be due to some errors in the measurements or the fact that the nature and behavior of the rock mass is much more complex than a continuum isotropic material. In such situations where it is not possible to match the displacements of all the extensometers, the results from the back analysis should reflect the possible range in input parameters.

Fig. 3.9 shows that for the two dimensional Phase2 model III with the parameter falling in the ranges given in Table 3.6, the ratio of maximum to minimum displacements at the reference head for different extensometers were found to be higher than those for the three dimensional FLAC3D models. According to Table 3.5, the extensometer displacements at the reference head range from 1.31-2.81 mm and 1.93-4.87 mm for the first and second

blasts, respectively. Hence, the corresponding ratios of maximum to minimum displacements are 2.15 and 2.52 for the first and second blasts, respectively. Although these values are still much lower than corresponding values of 3.21 and 3.90 based on the extensometers measurements, the two dimensional Phase2 model provided a better match to the measurements of all extensometers.
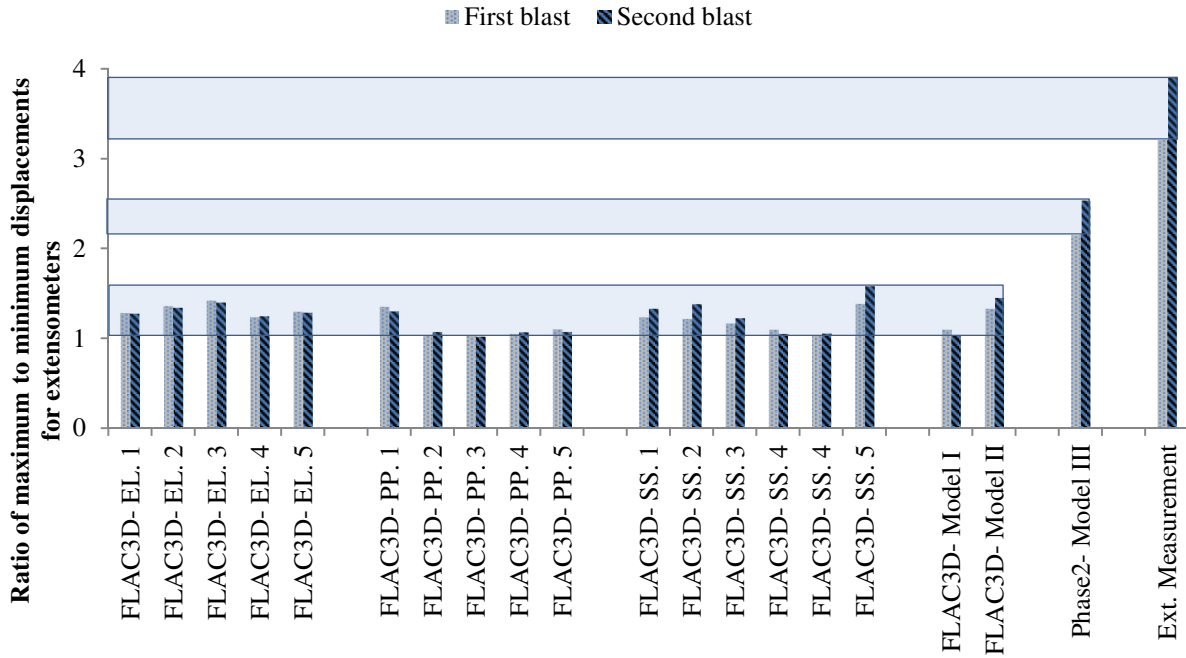
Fig. 3.9 The ratio of maximum to minimum displacements at the reference head for different extensometers from a number of FLAC3D and Phase2 models along with the extensometer measurements

In order to explore the reason for this difference between the results from the two and three dimensional models, it is useful to investigate the procedure in which three dimensional effects are handled by the two dimensional models. As discussed previously, Longitudinal Displacement Profiles are needed to help the user choose the appropriate amount of displacement that takes place ahead of the excavation face. Vlachopoulos and Diederichs (2009) provided the Longitudinal Displacement Profiles and guidelines used in this study.

To evaluate the extent to which these LDPs are accurate in capturing the real three dimensional effects, the relative convergence at different stages obtained from FLAC3D simulations for three different models are shown in Table 3.7. The first model PP (I) is an elastic-perfectly plastic model with parameters identical to Model I (Table 3.3) except that the residual values of cohesion and friction angle are equal to corresponding peak values. The second and third models, SS (I) and SS (II) are strain softening models with parameters identical to Models I and II (Table 3.3), respectively.

Table 3.7 Relative convergence at different stages obtained from FLAC3D simulations for three different models

Stage	PP (I)			SS (I)			SS (II)		
	Ext. 2	Ext. 3	Ext. 4	Ext. 2	Ext. 3	Ext. 4	Ext. 2	Ext. 3	Ext. 4
(1) Ext. installation, X/R=0.2	0.56	0.57	0.58	0.58	0.58	0.63	0.59	0.56	0.65
(2) After the first blast, X/R=0.8	0.83	0.83	0.84	0.83	0.83	0.85	0.85	0.83	0.87
(3) After the second blast, X/R=1.4	0.93	0.93	0.93	0.93	0.93	0.94	0.93	0.92	0.94

The first finding is that for the elastic-perfectly plastic model PP (I), the values of relative convergence for different extensometers at each stage are very close. It appears that for rock masses with elastic-perfectly plastic behavior, an isotropic LDP may be adequate even with an in-plane stress anisotropy ratio of 0.6. For the strain softening models SS (I) and SS (II), however, the value of relative convergence for different extensometers is more variable implying that an isotropic LDP cannot properly capture the three dimensional effects. Note that only three points along the shaft boundary are considered in Table 3.7, and investigating the results for additional points gives greater variability. It is also worth noting that the range of variability is higher at the first stage and decreases with increasing the distance from the face. Unfortunately, most of the displacement happens near the face and those occurring far from the face are of little significance.

Fig. 3.10 shows the upper bound, lower bound, and the average LDPs for the range of ratio of plastic zone radius to opening radius, R_p/R from 1.2 to 1.8 as determined from the previous two and three dimensional models. On the same plot the results from FLAC3D analyses are shown. Since the behavior for the average quality rock mass in the formation is strain softening and the results for SS (I) and SS (II) models given in Table 3.7 are very similar, for the sake of clarity only the results of the SS (II) model are shown in Fig. 3.10.

Again, the wide range of relative convergence in different directions near the face which decreases with increasing the distance from the face is noticeable. However, the results of real three dimensional analyses in all stages are well above the Vlachopoulos and Diederichs (2009) LDPs used in the two dimensional analyses. Hence, it can be concluded that the three dimensional effects could not be properly introduced into the two dimensional models using those LDPs. However, the most important point is that even by shifting the LDP upward so that it fits the data points, there is still the problem of variability of the relative convergence along the opening boundary. Hence, the adjusted LDP can be respected only for a few points along the opening boundary and it will be compromised for the rest of boundary.
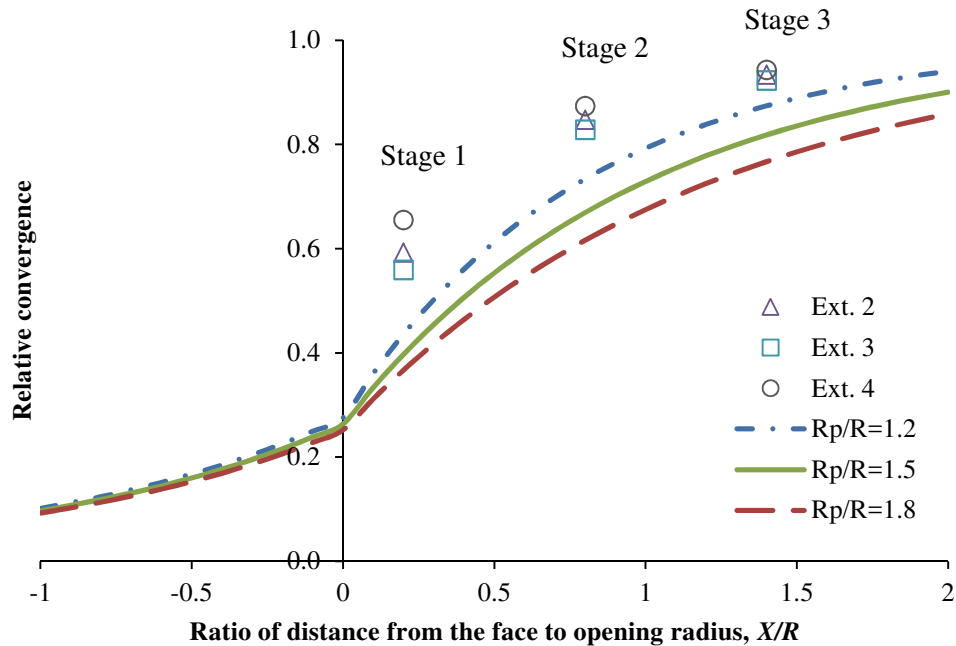
Fig. 3.10 Comparison of the relative convergence from the three dimensional model and the LDPs

Therefore, though giving apparently better match to the extensometer measurements (Fig. 3.8), the two dimensional models with LDPs cannot respect the real three dimensional effects for excavations in strain softening rock masses under anisotropic stress fields. It is not a surprising fact as the LDPs are originally obtained for circular openings in elastic or elastic-perfectly plastic rock masses under isotropic stress fields. These are three serious limiting conditions which are rarely encountered in real-world problems. However, convenience of two dimensional analyses has resulted in application of the LDPs for excavations of non-circular cross section in anisotropic in situ stress fields (e.g. Hoek et al. 2008, RocScience Inc. 2010). Apparently good matches which are directly the results of compromising the real three dimensional effects have also encouraged the use of two dimensional models.

3.6. Conclusions

In this paper the procedure of back analysis of the displacements at a deep shaft using continuum models was presented. The section of the 10 m diameter circular shaft considered in this study was located at a depth of 1172 m in Cretaceous volcanic sediments formation with intact uniaxial compressive strength and Geological Strength Index of 104 MPa and 62, respectively. Four radially installed extensometers were used to monitor the shaft response. Of those extensometers, Ext. 2, 3 and 4 produced reliable results, with the magnitude of the results from Ext. 3 being approximately twice as large as the magnitudes of the results from Ext. 2 and 4.

FLAC3D (three dimensional finite difference code) and Phase2 (two dimensional finite element code) were used to back analyse the measured displacements to determine the most likely rock mass properties. The initial values for the rock mass parameters were estimated from existing empirical relationships. The results of the FLAC3D model with the empirical parameters and a Mohr-Coulomb criterion and strain softening behavior gave a reasonable match to the measurements of Ext. 2 and 4 while underestimating the measurements of Ext. 3. In order to match the significantly higher displacements of Ext. 3, the mechanical parameters were adjusted causing a larger plastic zone. However, the obtained results significantly overestimated the displacements for Ext. 2 and 4. The two dimensional Phase2 models, however, gave a better match to the measurements of all extensometers.

In other words, while three dimensional models were not able to reproduce the significant difference between the results of different extensometer thereby giving good match to the measurements of one or two extensometers, the two dimensional models could reproduce a wider range of displacements for different extensometers which led to better overall fit to all three extensometer.

Investigating this phenomenon using the results of several three dimensional models with elastic, elastic-perfectly plastic, and strain softening behavior showed that for the given problem, there is indeed a theoretical limit for the difference among the measurements of different extensometers. However, the difference based on the measurements was much higher than the limit. As observed during the trial and error modelings, it implies that regardless of the material models and corresponding parameters, it is not possible to match the highly anisotropic measurements of the extensometers with any three dimensional continuum models adopting isotropic constitutive behavior.

However, it was still very surprising and questionable that the two dimensional Phase2 models were able to give a better match to the extensometers measurements. Using the results of three dimensional models, it was shown that the adopted Longitudinal Displacement Profile (LDP) for two dimensional models always underestimated the relative convergence especially in the near the face region where most of the displacement occurs. More importantly, it was shown that for the given problem with the ratio of minimum to maximum horizontal stresses of 0.6, the relative convergence especially near the face varies along the shaft periphery. It means that no isotropic LDP is able to respect the evolution of convergence for all the points along the opening boundary due to three dimensional effects of an advancing face. While the results of two dimensional models were found to be extremely sensitive to the relative convergence at each stage thereby showing the crucial importance of accurate considerations for three dimensional effects, they fail to respect the real variations of the displacements along the opening boundary at different stages of analysis. Compromising the real three dimensional effects is believed to be the reason for apparently better agreements between the measurements and the predictions of two dimensional models.

In summary, careful interpretation of the field measurements are recommended before any simulations as blind application of raw data can lead to extremely misleading results. Processing the data and modeling the real behavior of average quality rock masses needs

careful attention as a combination of structurally controlled and stress induced phenomena occurs simultaneously and separation of the effects is very difficult if not impossible. The empirical relationships for estimation of the rock mass parameters were found to be sufficiently accurate in preliminary stages of design. Accurate consideration of three dimensional effects is very important in the displacement back analysis. LDPs are originally developed for circular openings in elastic or elastic-perfectly plastic media under isotropic stress conditions. Though very tempting, extending the application of LDPs along with two dimensional modeling for excavations in strain softening media under anisotropic stresses is not recommended and can lead to misleading results.

References

Cai, M., Kaiser, P.K, Tasaka, Y., Minami, M., 2007. Determination of residual strength parameters of jointed rock masses using the GSI system. Int. J. Rock. Mech. Min. Sci. 44, 247-265.

Carranza-Torres. C., Fairhurst, C., (2000). Application of the convergence–confinement method of tunnel design to rock masses that satisfy the Hoek–Brown failure criterion. Tunn. Undergr. Space. Technol. 15, 187–213.

Cividini, A., Jurina, L., Gioda, G., (1981). Some aspects of characterization problems in geomechanics. Int. J. Rock. Mech. Min. Sci. 18, 487–503.

Gioda, G., Maier, G., (1980). Direct search solution of an inverse problem in elastoplasticity: identification of cohesion, friction angle and in situ stress by pressure tunnel tests. Int. J. Numer. Meth. Eng. 15, 1823–1848.

Hoek, E. and Brown, E. T. (1980), Empirical strength criterion for rock masses, J. Geotech. Eng. Div., ASCE 106(GT9), 1013-1035.

Hoek, E., Brown, E.T., (1997). Practical estimates or rock mass strength. Int. J. Rock. Mech. Min. Sci. 34, 1165-1186.

Hoek, E., Carranza-Torres, C., Corkum, B., (2002). Hoek-Brown failure criterion – 2002 Edition. In: Proceedings of the fifth North American rock mechanics symposium, Toronto, pp 267-273.

Hoek, E., Carranza-Torres, C., Diederichs, M.S., Corkum, B,. (2008). Integration of geotechnical and structural design in tunnelling – 2008 Kersten Lecture. In: Proceedings University of Minnesota 56th Annual Geotechnical Engineering Conference. Minneapolis, pp 1-53.

Hoek, E., Diederichs, M.S., (2006). Empirical estimation of rock mass modulus. Int. J. Rock. Mech. Min. Sci. 43, 203–215.

Itasca Inc,. (2009). FLAC- Fast Lagrangian Analysis of Continua, Version 3.3, Minneapolis, United States.

Miranda, T., Dias, D., Eclaircy-Caudron, S., Gomes Correia, A., Costa, L., (2011). Back analysis of geomechanical parameters by optimisation of a 3D model of an underground structure. Tunn. Undergr. Space. Technol. 26, 659–673.

Panet, M., (1995). Le calcul des tunnels par la me´thode convergenceconfinement. Presses de l'Ecole Nationale des Ponts et Chausse´es, Paris, France, p. 177.

Rocscience Inc., (2010). 3D tunnel simulation using the core replacement technique. Phase2 Version7.0 Tutorial Manual, Toronto, Canada.

Rocscience Inc,. (2011). Phase2 - Finite Element Analysis for Excavations and Slopes, Version 8.0, Toronto, Canada.

Sakurai, S., Takeuchi, K., (1983). Back analysis of measured displacements of tunnels. Rock. Mech. Rock. Eng. 16, 173-180.

Unlu, T., Gercek, H., (2003). Effect of Poisson's ratio on the normalized radial displacements occurring around the face of a circular tunnel. Tunn. Undergr. Space. Technol. 18, 547–553.

Vardakos, S.S., Gutierrez, M.S., Barton, N.R., (2007). Back-analysis of Shimizu Tunnel No. 3 by distinct element modeling. Tunn. Undergr. Space. Technol. 22, 401–413.

Vlachopoulos, N., Diederichs, M.S., 2009. Improved longitudinal displacement profiles for convergence-confinement analysis of deep tunnels. Rock. Mech. Rock. Eng. 42, 131-146.

Yazdani, M., Sharifzadeh, M., Kamrani, K., Ghorbani, M., (2012). Displacement-based numerical back analysis for estimation of rock mass parameters in Siah Bisheh powerhouse cavern using continuum and discontinuum approach. Tunn. Undergr. Space. Technol. 28, 41–48.

Chapter 4

Cohesion degradation and friction mobilization in brittle failure of rocks[3]

4.1. Introduction

Predicting the behavior of rock masses is a necessary part of rock engineering design. Over the years, various empirical and numerical approaches have been developed to address the problem. Discontinuum modeling approaches emphasize the fractured nature of rock masses and can capture the discontinuous displacement fields resulting from relative movement of individual blocks. On the other hand, continuum modeling approaches consider the rock mass as an equivalent continuum with degraded mechanical properties due to the presence of fractures.

Strength of materials has long been a subject of interest in engineering design and numerous strength theories have been proposed over the years. While modern day theories often become increasingly complex, the fundamental components which contribute to the overall strength of materials can be explained in simple terms.

Starting from the simplest system where there is a contact between two separate bodies, Amonton's law of friction states that the shear force required to cause the slip is proportional to the normal force acting on the surface and the coefficient of proportionality is the friction coefficient. Adding some bonds between the contacting bodies, Coulomb criterion states that there is still a direct relationship between the critical shear force and the applied normal force. However, there is finite shear strength even at zero normal force in a bonded system. This is the cohesive component of strength which totally depends on the bonds between the contacting surfaces.

The bonded contacts system described above is a useful model to study the strength of brittle rocks. Rocks are composed of mineral grains attached together. Researchers (e.g., Bieniawski 1967; Martin and Chandler, 1994) have shown that during a standard compression test that follows the ISRM Suggested Guidelines (Brown, 1981), brittle rocks go through five distinct stages shown in Fig. 4.1.

---

[3] A version of this chapter is submitted as a paper to the International Journal of Rock Mechanics and Mining Sciences
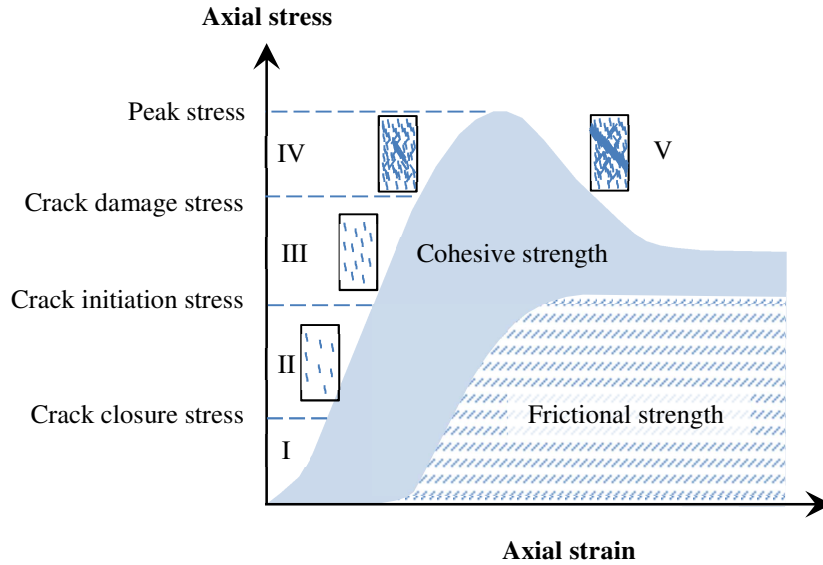
Fig. 4.1 The five stages of compressive brittle failure of rocks (Bieniawski, 1967), and the possible development of cohesive and frictional strength components (modified after Hajiabdolmajid et al., 2002)

In stage I, existing cracks are closed under relatively low stresses causing low initial stiffness. After crack closure, stage II starts with linear elastic deformations in axial and lateral directions. In stage III, stable axial cracks are initiated causing acoustic emissions (AE) and departure from linear expansion in the lateral direction. As loading continues, the length and number of microcracks within the material increase to a point where axial microcracks begin to coalesce together and form shear cracks. This marks the start of stage IV, unstable crack growth, and the corresponding stress level is called the crack damage stress. Aside from a sharp increase in the number of AE events, crack damage stress can also be identified using the volumetric strain response and denotes where the sample ceases to contract and starts to dilate. Crack damage stress also corresponds to the long-term strength of the material (Schmidtke and Lajtai, 1985) as higher loads can only be sustained for a short time and cannot be relied on for the long term (Martin and Chandler, 1994). By increasing loading, the peak stress is reached which marks the start of post-peak stage V associated with a macro shear failure and drop of stress level.

From a microscopic point of view, the rock sample in a triaxial test starts from an initial state with some pre-existing microcracks and experience damage i.e., initiation, propagation, and coalescence of cracks. Going back to the concept of a bonded contacts model, as crack density increases the number of bonds and therefore cohesive strength decreases (Fig. 1). Frictional strength, on the other hand, increases with increasing number of crack surfaces and will be present even after all the bonds are broken (Fig. 1).

Continuum models commonly used in rock engineering mostly focus on the peak stress and ignore the interrelationship between damage, deformability, and strength. Such approaches

54

have shown to be ineffective in capturing the brittle failure of rock in situ (Hajiabdolmajid et al, 2002). While the approach suggested by Martin (1997) and applied by Hajiabdolmajid et al. (2002) has gained wider acceptance (e.g., Diederichs, 2007; Zhao and Cai, 2010; Edelbro et al., 2012; Walton et al., 2015), little work has been carried out to develop the methodology using confined laboratory tests. In this study, the results of confined damage controlled tests have been used to capture the full failure process and development of cohesion and friction at different damage levels. The results have been analyzed and equations are proposed to describe the observed behavior. The model is implemented in a numerical code and case studies have been used to verify the proposed approach.

4.2. Damage-controlled laboratory tests

Standard triaxial compression tests using stiff servo-controlled loading machines can provide pre- and post-peak stress-strain curves at different levels of confining stress. However, they provide little if any information regarding the gradual damage process (crack initiation, propagation, and coalescence) and its effect on the fundamental components of strength, i.e., cohesion and friction.

To capture the effect of incremental microstructural damage on the macroscopic strength characteristics, Martin (1993) reported the results from a series of damage-controlled compression tests on Lac du Bonnet (LdB) granite and Indiana limestone. The test specimens were prepared according to the ISRM suggested methods (Brown, 1981).

In the damage-controlled tests, the axial and confining stress were initially increased simultaneously at a rate of 0.75 MPa/s to reach the desired confinement level. Axial stress was then increased at the same rate up to about 75% of the expected peak strength with unload-reload cycles. In order to ensure a controlled damage process, the unload-reload cycles after 75% of the peak strength were carries out at 0.063 mm increments of circumferential deformation. During unloading, axial stress was reduced to confining stress in triaxial tests and to 5 MPa in the unconfined tests. The results of damage-controlled tests were shown to be in agreement with standard compression tests. More details on the damage-controlled tests is given by Martin (1993) and Martin and Chandler (1994).

The damage-controlled tests reported by Martin (1993) provided pre- and post-peak stress-strain curves for a gradual damage process (Fig. 4.2). The results are used in this study to develop theories and modeling approaches.

4.2.1.   Tests on LdB granite samples from the URL

A comprehensive set of damage-controlled tests were carries out on the samples of Lac du Bonnet granite from the 420 level of the Underground Research Laboratory (URL) owned by Atomic Energy of Canada Limited (Martin, 1993). The results under uniaxial and triaxial loading conditions with 10, 20, 40, and 60 MPa confining stress have been analyzed. In

order to quantify the extent of damage within the sample, volumetric strain were evaluated as initiation and propagation of cracks during each loading cycle cause an increase in sample volume. It can be seen from Fig. 4.2b that after each cycle, the volumetric strain at unloading stress shifts towards left (decreasing volumetric strain, i.e., dilation). As suggested by Martin and Chandler (1994), cumulative irreversible volumetric strain can be used for damage quantification and will be referred to in this paper as plastic strain.
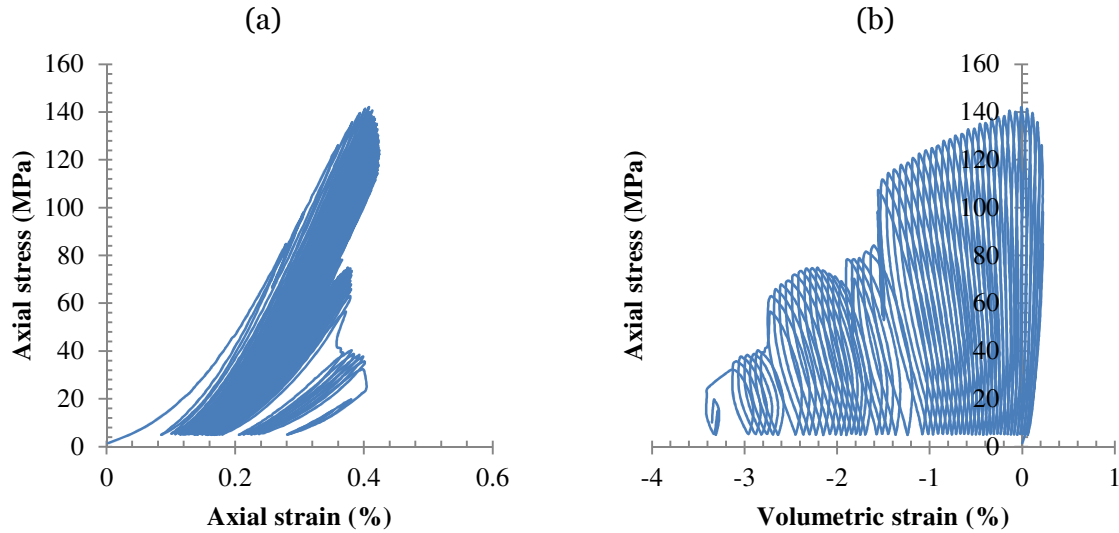
Fig. 4.2 Results of unconfined damage-controlled tests on a sample of Lac du Bonnet granite from the 420 level of URL, (a) axial stress vs. axial strain, (b) axial stress vs. volumetric strain

A MATLAB code was written to automatically extract crack damage stress and peak stress for each loading cycle. Fig. 4.3 shows the variations of crack damage stress and peak stress with plastic strain for samples of Lac du Bonnet granite from the 420 level of the URL. It can be observed that both crack damage stress and peak stress are directly related to confining stress. At all confinement levels, crack damage stress rapidly drops to a threshold value with increasing damage and plastic strain. The peak stress, however, shows an initial hardening followed by a slower softening as plastic strain increases. The maximum values of crack damage stress and peak stress for the unconfined tests are 110 and 141 MPa, respectively.

4.2.2.   Tests on LdB granite samples from the Cold Spring Quarry

Similar damage controlled tests were also carried out on the samples of Lac du Bonnet granite from the Cold Spring Quarry located in southeastern Manitoba, Canada. The tests were done under uniaxial and triaxial loadings with confining stress levels of 2 and 10 MPa. Crack damage stress and peak stress for the samples from the Cold Spring Quarry are shown in Fig. 4.4. As it can be seen, the test results for the Cold Spring Quarry are limited

compared to those of URL in terms of both confinement levels and also the number of loading cycles and damage increments. The plastic strains obtained from the Cold Spring Quarry test results are less than 0.7% compared to near 3% for the URL samples. The general trends of data, however, are very similar. Crack damage stress and peak stress both increase with confinement and crack damage stress decreases more rapidly than peak stress with increasing plastic strain.
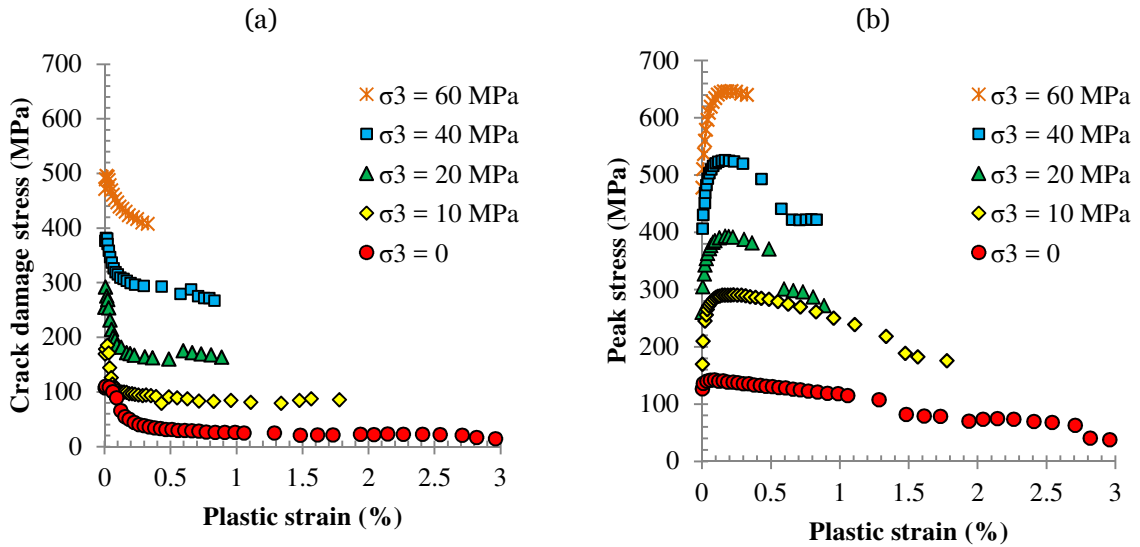
Fig. 4.3 (a) Crack damage stress and, (b) peak stress obtained from damage-controlled tests on samples of Lac du Bonnet granite from the 420 level of URL
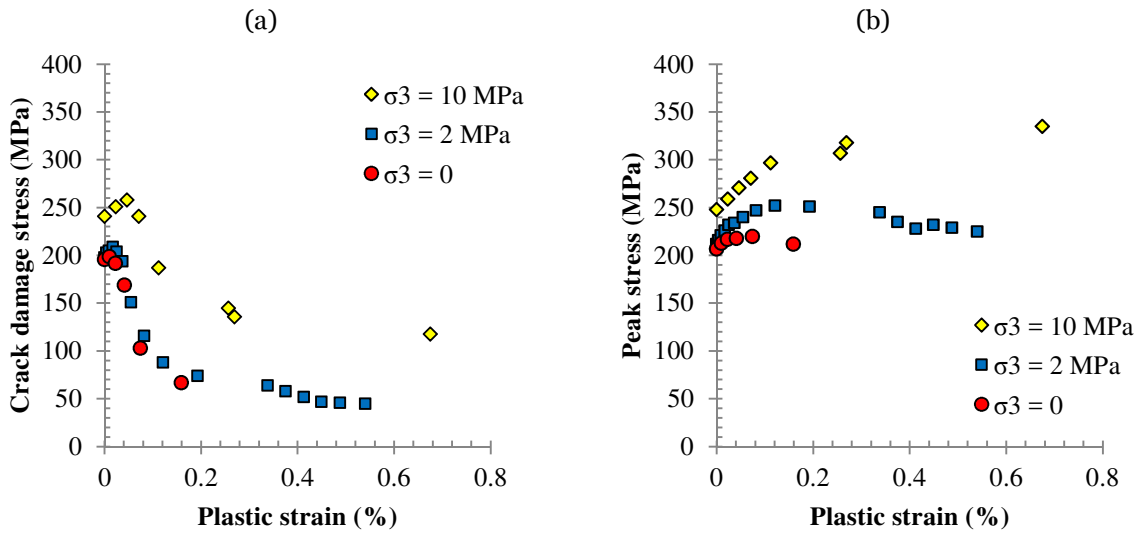
Fig. 4.4 (a) Crack damage stress and, (b) peak stress obtained from damage-controlled tests on samples of Lac du Bonnet granite from the Cold Spring Quarry

It can be observed that the sample form the Cold Spring Quarry is significantly stronger from the URL sample. The maximum values of crack damage stress for the unconfined samples from URL and Cold Spring are 110 and 199 MPa, respectively. The peak unconfined stress for the URL sample is 141 MPa compared to 220 MPa for the Cold Spring sample.

As extensively discussed by Martin and Stimpson (1994), the difference between the results of tests on Lac du Bonnet granite samples from the 420 level URL and Cold Spring Quarry is due to sample disturbance rather than actual changes of in situ properties with depth. Samples obtained from the high in situ stress field at the 420 level of URL have experienced excessive stress concentrations and damage during sampling. On the other hand, sample taken at shallow depth from the Cold Spring Quarry have not been subject to such disturbance and therefore provide a closer estimate of the actual undamaged in situ properties.

4.2.3. Tests on samples of Indiana limestone

In order to examine the applicability of the previous findings to other rock types, a series of damage-controlled tests were carried out on samples of Indiana limestone. The tests were done in unconfined and triaxial conditions with confining stresses of 4 and 10 MPa. Crack damage stress and peak stress for the samples of Indiana limestone are shown in Fig. 4.5. Again, the number and range of data for Indiana limestone are limited compared to those of granite samples from the URL. However, limestone samples display similar trends observed in granite, i.e., crack damage and peak stress increase with confinement and decrease with plastic strain.
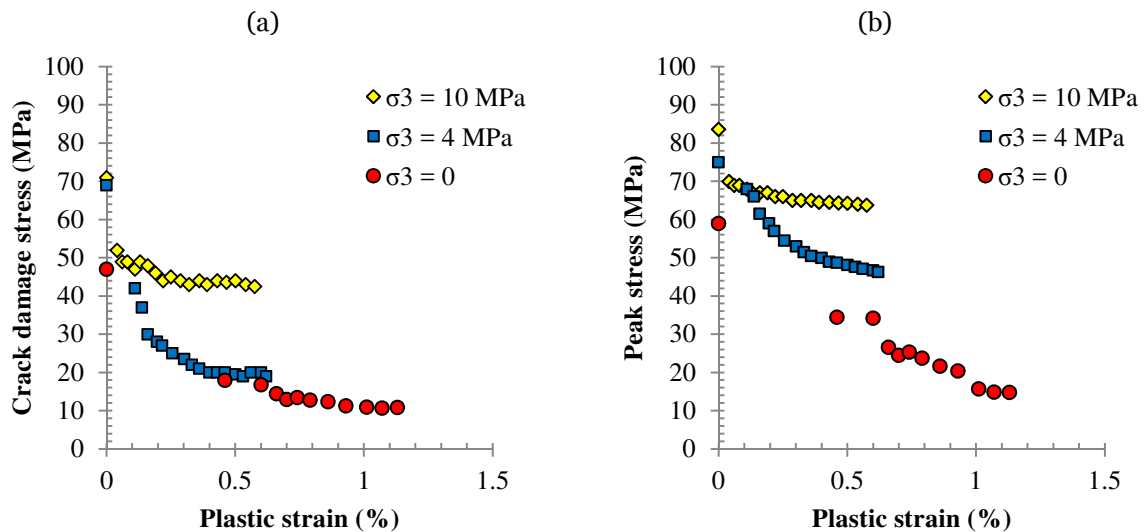
Fig. 4.5 (a) Crack damage stress and, (b) peak stress obtained from damage-controlled tests on samples of Indiana limestone

4.3. Determination of cohesion and friction angle

The well-known Mohr-Coulomb strength envelope can be expressed as:

$$\sigma_1 = 2c \tan\left(\frac{\varphi}{2} + \frac{\pi}{4}\right) + \sigma_3 \tan^2\left(\frac{\varphi}{2} + \frac{\pi}{4}\right)$$

(4.1)

where σ_1 and σ_3 are the major and minor principal stress and c and φ are the cohesion and friction angle, respectively. Note that the slope of the σ_1 vs σ_3 envelope depends only on friction angle while cohesion controls the intercept.

Fig. 4.6 shows the maximum and minimum values of crack damage stress at different confinement levels. For the URL samples, the maximum and minimum crack damage stress points fall on two parallel lines with a slope of 6.4. According to Eq. (4.1), this slope corresponds to a friction angle of 47° at crack damage stress level. For the Cold Spring samples, the slope of the maximum crack damage line is 6.0 corresponding to a friction angle of 46°. The threshold minimum value of crack damage stress for the unconfined sample from Cold Spring has not been captured in the test and the last data point has been used (Fig. 4.4a). Using the minimum obtained value from the unconfined test gives a similar friction angle of 46°. Maximum and minimum crack damage stresses for Indiana limestone show a slope of 2.7 corresponding to a friction angle of 28°.
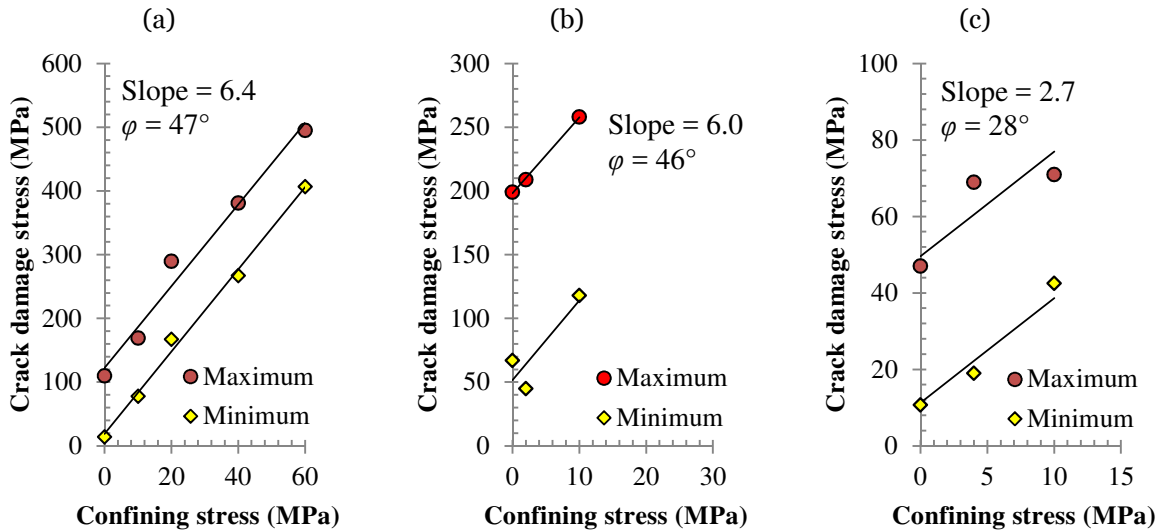
Fig. 4.6 Relationship between maximum and minimum values of crack damage stress and confining stress for samples of (a) Lac du Bonnet granite from 420 level of URL (b) Lac du Bonnet granite from Cold Spring Quarry, and (c) Indiana limestone

Having established the value of friction angle at crack damage stress, it is now possible to determine the relationship between cohesion and plastic strain. Fig. 4.7 shows cohesion

calculated using crack damage stresses and friction angles of 47°, 46°, and 28° for the URL granite, Cold Spring granite, and Indiana limestone, respectively. It can be observed that in all cases, cohesion rapidly drops to a residual value. Data points for all confinement levels are roughly on the same curve which suggests that cohesion is indeed independent of confining stress. Note that initial cohesion for Cold Spring samples is significantly higher than those for the 420 level of URL. As explained earlier, this is attributed to the fact that URL samples have been subject to sampling disturbance and damage due to high in situ stresses at the depth of 420 m at URL. The threshold value of cohesion at plastic strain higher than 0.5%, however, is quite similar for the URL and Cold Spring samples. Despite the fact that Indiana limestone is much weaker than Lac du Bonnet granite, it also reaches a threshold value for cohesion at plastic strain of about 0.5%.

Peak stress data combined with cohesion values in Fig. 4.7 can now be used to determine the variation in friction angle with plastic strain. Fig. 4.8 shows the effect of plastic strain on friction angle of Lac du Bonnet granite and Indiana limestone. It can be seen that friction angle initially increases with increasing plastic strain. Another important observation is that confining stress clearly affects friction angle. The increase of friction angle is most pronounced in unconfined tests and as confinement increases, maximum friction angle decreases. This can be attributed to the strengthening effect of dilation (Barton and Choubey, 1977). Increasing confining stress suppresses dilation thereby reducing its strengthening contribution.

Data from samples of granite at the URL and Indiana limestone also show that at higher plastic strains, friction angle begins to slowly decrease. This is expected as excessive damage and plastic strain cause the friction angle to decrease towards the residual friction angle (Martin and Chandler, 1994). Cold Spring data have not captured this phenomenon as the number of loading cycles and ranges of plastic strain are relatively limited.
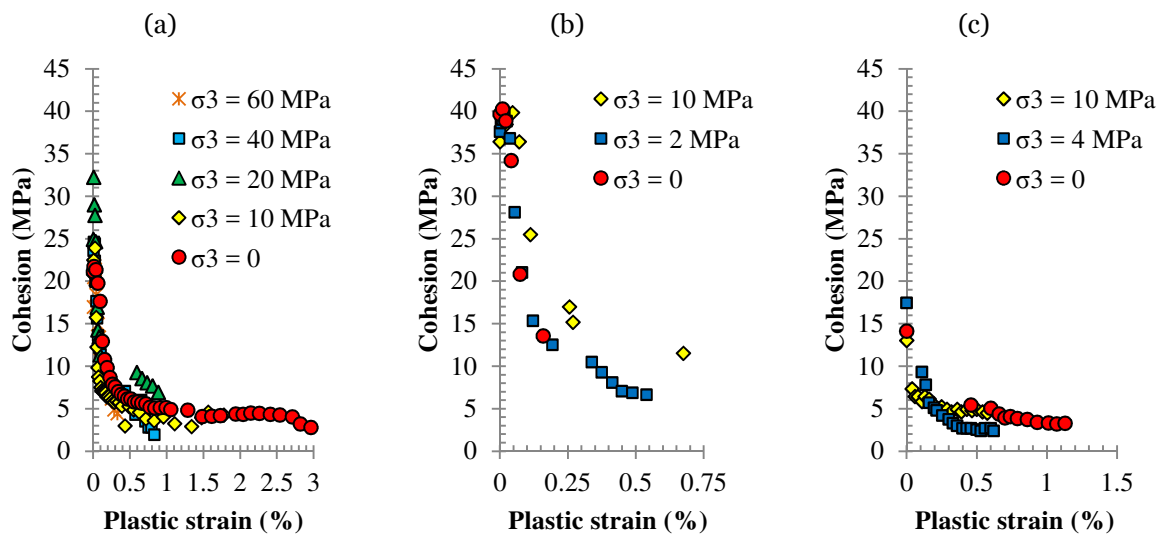
Fig. 4.7 Degradation of cohesion for samples of (a) Lac du Bonnet granite from 420 level of URL (b) Lac du Bonnet granite from Cold Spring Quarry, and (c) Indiana limestone

4.4. Theoretical models for laboratory behavior

In this section, a theoretical model is proposed to capture the mobilization of cohesion and friction as obtained from the damage-controlled laboratory tests. As shown in Fig. 4.7, as plastic strain increases cohesion decreases from an initial value to a residual value. Mobilization of friction angle, however, is a little more complex (Fig. 4.8). By increasing plastic strain, friction angle starts to increase from an initial value to a maximum value followed by a slow reduction towards the residual friction angle at higher plastic strains. Furthermore, the maximum value of friction angle depends on confining stress and decreases with increasing confinement.

The degradation of cohesion with increasing plastic strain ε^p can be given by:

$$c = c_r + (c_i - c_r)\left[2 - \frac{2}{1 + \exp\left(-5\dfrac{\varepsilon^p}{\varepsilon^p_{c,r}}\right)}\right]$$

(4.2)
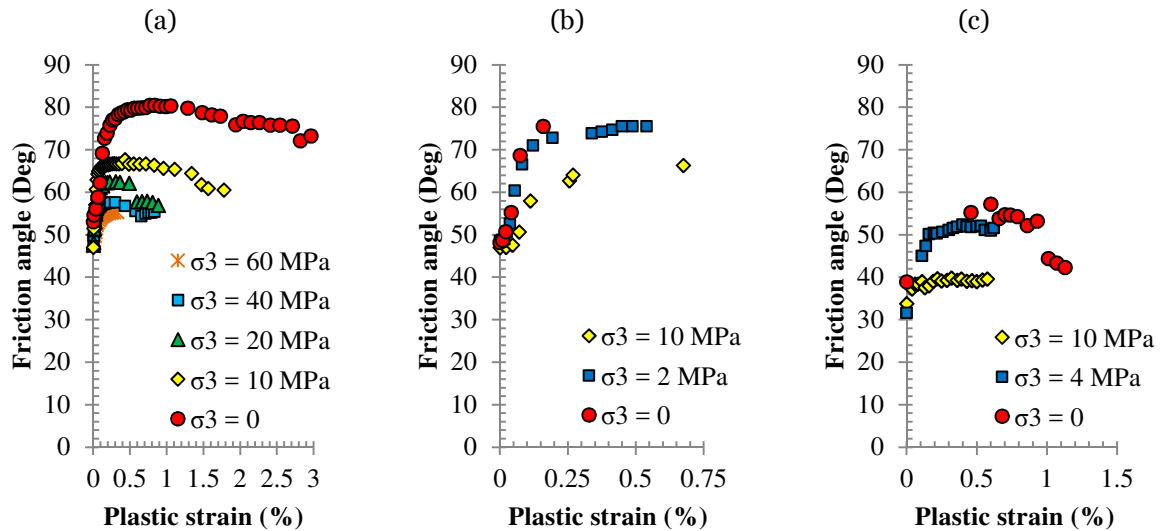
Fig. 4.8 Mobilization of friction for samples of (a) Lac du Bonnet granite from 420 level of URL (b) Lac du Bonnet granite from Cold Spring Quarry, and (c) Indiana limestone

where c_i and c_r are initial and residual cohesion and $\varepsilon^p_{c,r}$ is the plastic strain at which cohesion approaches the residual value (cohesion degradation 99% completed). Mobilization of friction can be expressed as:

$$\varphi = \varphi_i + (\varphi_{max} - \varphi_i)\left[\dfrac{2}{1+\exp\left(-5\dfrac{\varepsilon^p}{\varepsilon^p_{\varphi,max}}\right)} - 1\right] - (\varphi_{max} - \varphi_r)\left[\dfrac{1}{1+\exp\left(-5\dfrac{2\varepsilon^p - \varepsilon^p_{\varphi,r} - \varepsilon^p_{\varphi,max}}{\varepsilon^p_{\varphi,r} - \varepsilon^p_{\varphi,max}}\right)}\right]$$

$$(4.3)$$

where φ_i, φ_{max} and φ_r are initial, maximum and residual friction angle, respectively. $\varepsilon^p_{\varphi,max}$ and $\varepsilon^p_{\varphi,r}$ are the plastic strains at which friction angle approaches the maximum and residual value (within 1%), respectively. If $\varepsilon^p_{\varphi,r} >> \varepsilon^p_{\varphi,max}$, Eq. (4.3) can be simplified as:

$$\varphi = \varphi_i + (\varphi_{max} - \varphi_i)\left[\dfrac{2}{1+\exp\left(-5\dfrac{\varepsilon^p}{\varepsilon^p_{\varphi,max}}\right)} - 1\right] - (\varphi_{max} - \varphi_r)\left[\dfrac{1}{1+\exp\left(-5\dfrac{2\varepsilon^p - \varepsilon^p_{\varphi,r}}{\varepsilon^p_{\varphi,r}}\right)}\right]$$

$$(4.4)$$

Finally, the relationship between the maximum friction angle and confining stress can be described as:

$$\varphi_{max} = \varphi^{\infty}_{max} + (\varphi^0_{max} - \varphi^{\infty}_{max})\exp\left(-\kappa\dfrac{\sigma_3}{\sigma_{c,i}}\right)$$

$$(4.5)$$

where $\sigma_{c,i}$ is the uniaxial compressive strength of intact rock, κ is a constant, and φ^0_{max} and φ^{∞}_{max} are maximum friction angle at zero and infinite confining stress, respectively.

The comprehensive data for the LdB samples at the URL was used as an example to illustrate the application of the proposed theoretical model for laboratory results. The average Young's modulus, E for Lac du Bonnet at the 420 level of URL is 60 GPa. As shown in Fig. 4.2a, uniaxial compressive strength is 141 MPa. Fig. 4.7a shows that average cohesion starts from 27 MPa and degrades to about 4 MPa. According to Fig. 4.8a, initial friction angle is 47°. Maximum friction angle for the unconfined test is 77° and reaches the asymptotic value of 55° at 60 MPa confining stress. Based on the results of direct shear tests carried out by Lajtai and Gadi (1989), the residual friction angle for Lac du Bonnet granite is considered to be 42° mobilized at 1% plastic strain. Finally, the κ constant can be determined from Fig. 4.9 which shows the relationship between maximum friction angle and confining stress according to Eq. (4.5).
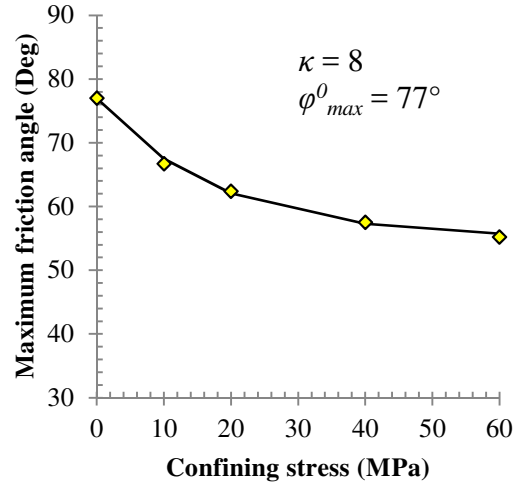
Fig. 4.9 Relationship between maximum friction angle and confining stress for laboratory samples of Lac du Bonnet granite

Fig. 4.10 shows the mobilization of cohesion and friction angle and stress-strain curves using the theoretical model with parameters shown in Table 4.1. Note that for a proper comparison with laboratory data, the initial non-linear strains during the seating phase of the tests were added to the calculated strains making the theoretical stress-strain curves to shift to the right of the strain axis. Volumetric strain response is given in Appendix B.

Table 4.1 Parameters of the proposed model for laboratory behavior of Lac du Bonnet granite

E (GPa)	$\sigma_{c,i}$ (MPa)	c_i (MPa)	c_r (MPa)	$\varepsilon_{c,r}^p$ (%)	φ_i (deg)	φ_{max}^0 (deg)	φ_{max}^∞ (deg)	φ_r (deg)	$\varepsilon_{\varphi,max}^p$ (%)	$\varepsilon_{\varphi,r}^p$ (%)	κ
60	141	27	4	0.3	47	77	55	42	0.3	1.0	8

4.5. Theoretical models for in situ behavior

Theoretical models to capture brittle failure of rocks in situ are discussed in this section. Hajiabdolmajid et al (2002) used the Mine-by tunnel at the URL as a case study and showed that traditional constitutive models based on simultaneous mobilization cohesion and friction could not capture the observed zone of brittle failure around the tunnel (Fig. 4.11a,b). They then used a cohesion-weakening friction-strengthening (CWFS) model in which cohesion decreased from an initial value of 50 MPa to a residual value of 15 MPa at 0.2% plastic strain and friction angle increased from zero to 48° at 0.5% plastic strain. This model adequately captured the V-shaped notches formed around the Mine-by tunnel (Fig. 4.11c).
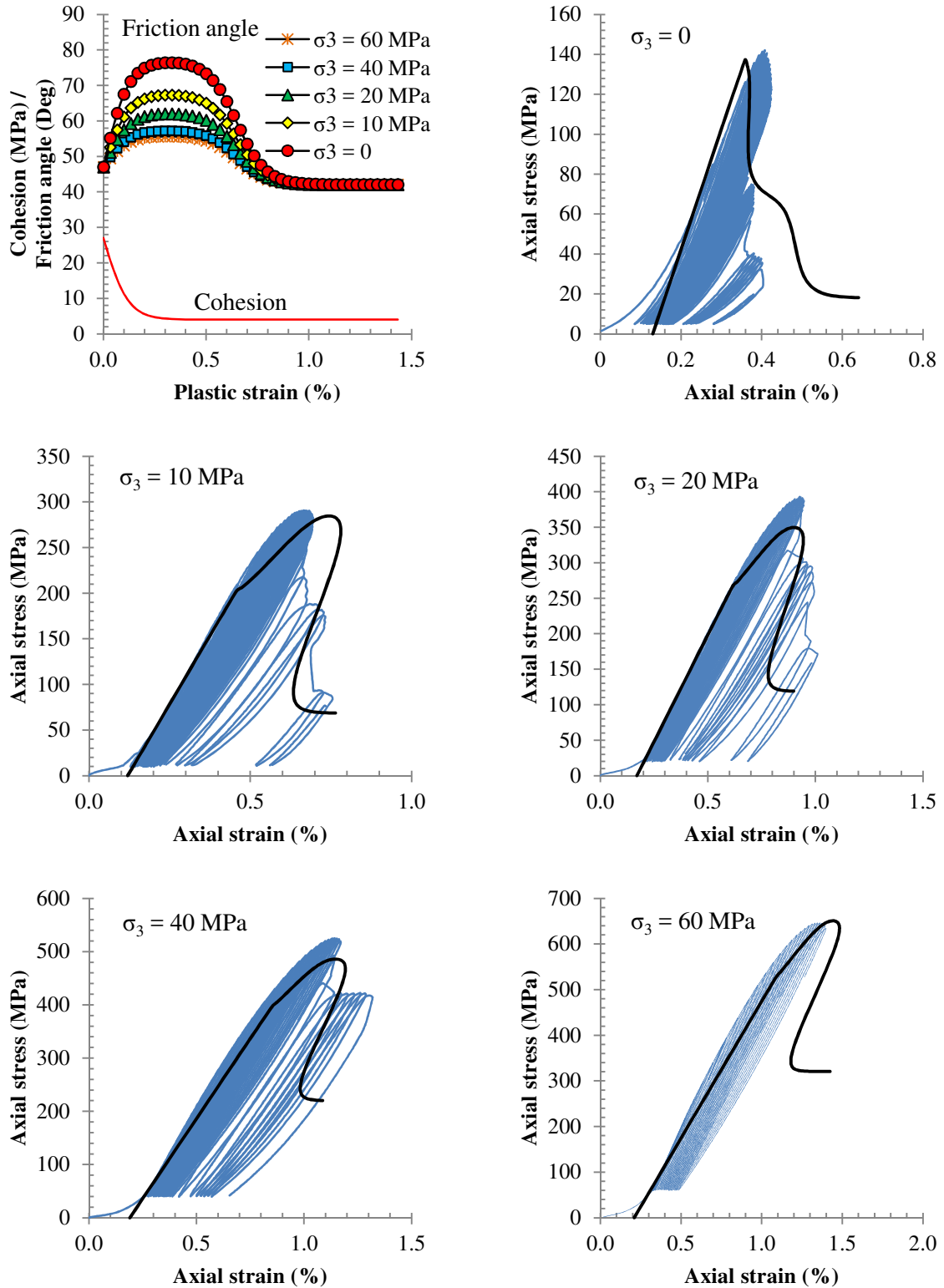
Fig. 4.10 Cohesion degradation and friction mobilization in the proposed model and comparison of experimental (fine line) and simulated (bold line) stress-strain curves
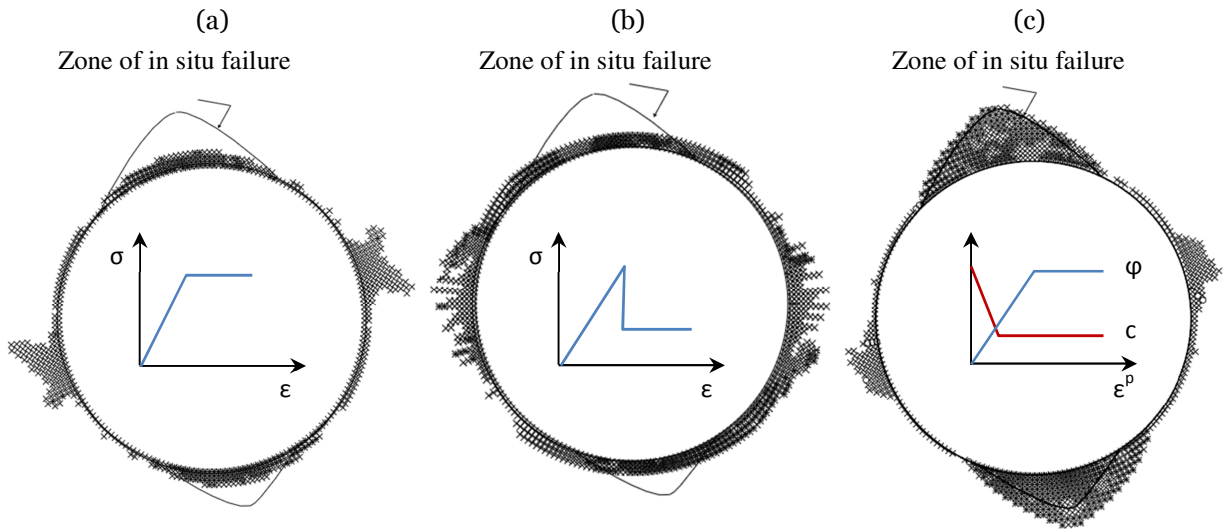
Fig. 4.11 Zone of failure around the Mine-by tunnel using (a) elastic perfectly-plastic model, (b) elastic brittle model and (c) cohesion-weakening friction-strengthening model (modified from Hajiabdolmajid et al, 2002)

It is useful to take a closer look at the model shown in Fig. 4.11c and determine the corresponding strength envelopes at different levels of plastic strain. Fig. 4.12a shows the strength envelopes at plastic strains ranging from 0.0 to 0.5%. Note that strength envelopes for plastic strains higher than 0.5% are identical to that for 0.5% plastic strain because both cohesion and friction angle remain constant after 0.5% plastic strain as shown in Fig. 4.11c.

Fig. 4.12a shows that by increasing damage and plastic strain, the slope of the strength envelope increases. The intercept, however, shows an initial decrease followed by an increase after 0.2% plastic strain. The reason is that according to Eq. (4.1), the slope is only a function of friction angle thereby friction mobilization causes increasing slope. The intercept, on the other hand, depends on both cohesion and friction angle. For plastic strains from 0.0 to 0.2%, cohesion degradation and friction mobilization occurs simultaneously and the combined effect is decreasing intercept. From 0.2 to 0.5%, cohesion remains constant while friction mobilization continues leading to an increase in the intercept.

The implications of such model are shown in Fig. 4.12b in terms of stress-strain curves in triaxial compression for different confining stresses. It can be observed that in unconfined condition, stress drops from 100 MPa to 42 MPa and then increases to 78 MPa. Stress-strain curves at 5 and 10 MPa also show similar trends. Obviously, such increase of strength after strain softening is not plausible and shows a fundamental flaw in the CWFS model proposed by Hajiabdolmajid et al (2002).

This problem is the result of using two different plastic strains for stabilization of cohesion and friction angle, i.e., 0.2% and 0.5%, respectively. It can be shown that using the same plastic strain for stabilization of cohesion and friction angle will remedy the unreasonable behavior of the model. Further improvements can be made by using smooth curves instead

of straight lines to better capture the gradual process of cohesion degradation and friction mobilization.
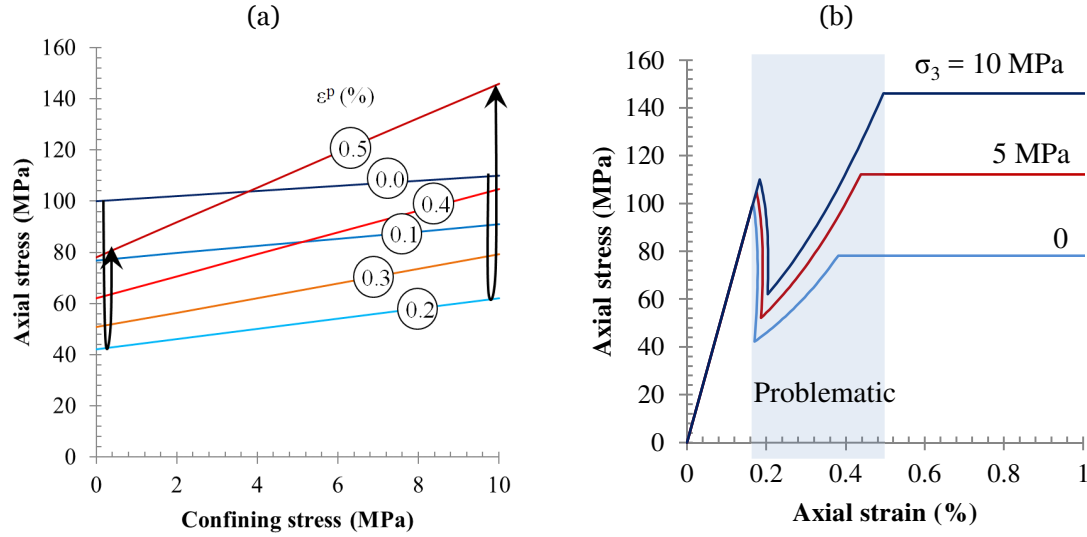
Fig. 4.12 (a) Strength envelopes at different levels of plastic strain and (b) stress-strain curves for the CWFS model used by Hajiabdolmajid et al (2002)

The proposed model for in situ failure of brittle rocks can be given by:

$$c = c_r + (c_i - c_r)\left[2 - \frac{2}{1 + \exp\left(-5\dfrac{\varepsilon^p}{\varepsilon_r^p}\right)}\right]$$

(4.6)

$$\varphi = \varphi_i + (\varphi_r - \varphi_i)\left[\frac{2}{1 + \exp\left(-5\dfrac{\varepsilon^p}{\varepsilon_r^p}\right)} - 1\right]$$

(4.7)

where $\varepsilon_r^p = \varepsilon_{c,r}^p = \varepsilon_{\varphi,r}^p$. Eq. (4.6) is identical to the Eq. (4.2) for laboratory behavior is repeated here for the sake of convenience and completeness. Eq. (4.7) can be considered as a simplified version of Eq. (4.3) proposed for laboratory behavior.

To illustrate the difference between the proposed smooth non-linear model with $\varepsilon_{c,r}^p = \varepsilon_{\varphi,r}^p$ and the commonly-used linear model with $\varepsilon_{c,r}^p \neq \varepsilon_{\varphi,r}^p$, the stress-strain curves for the proposed model using identical initial and residual values of cohesion and friction angle as those in Fig. 4.12 and $\varepsilon_{c,r}^p = \varepsilon_{\varphi,r}^p = 0.5\%$ are shown in Fig. 4.13. It can be seen that the

proposed model eliminates the problematic behavior of the current linear models with $\varepsilon_{c,r}^p \neq \varepsilon_{\varphi,r}^p$ shown in Fig. 4.12b while giving similar yield and residual strength values.
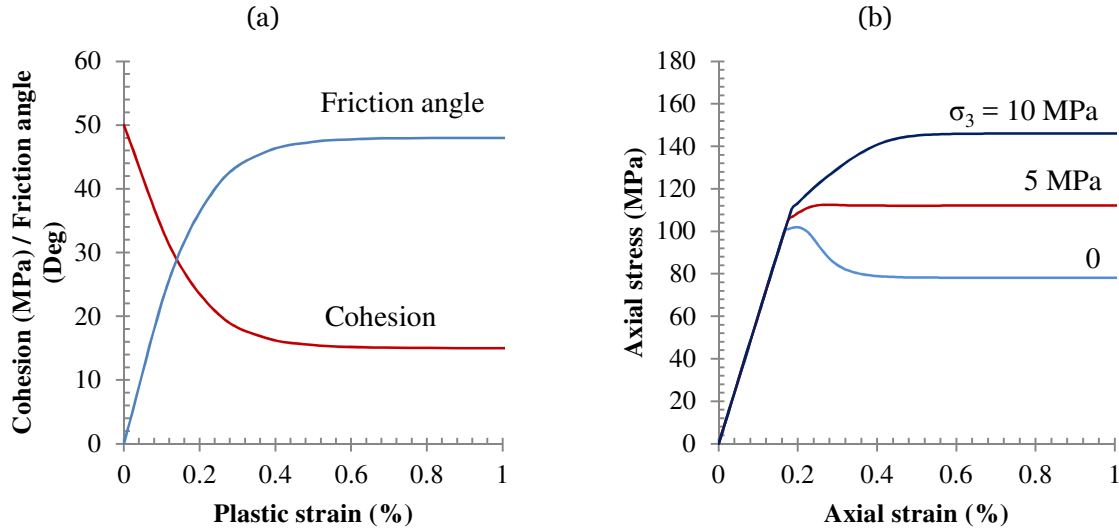
Fig. 4.13 Example of the proposed model for in situ behavior (a) cohesion degradation and friction mobilization and (b) corresponding stress-strain curves

4.6. Numerical implementation of the in situ model

The in situ model presented in Eqs. (4.6) and (4.7) was implemented in the finite difference code, FLAC3D (Itasca Inc., 2009). Four tunnels at the 420 level of the URL were used as case studies to verify the proposed modelling approach. The tunnels were excavated in massive sparsely-jointed Lac du Bonnet granite.

The Mine-by experiment was conducted to study the process of progressive failure around excavations under high induced stresses. The tunnel was 3.5 m in diameter and excavated using non-explosive mechanical excavation method to minimize excavation-induced damage. The Mine-by tunnel was advanced parallel to the intermediate principal in situ stress of 45 MPa to maximize deviatoric stresses around the tunnel. The major and minor principal in situ stresses were 60 MPa subvertical and 11 MPa subhorizontal with 11° plunge from horizontal.

The TSX tunnel was 3.5 m high with elliptical cross section and 1.25:1 aspect ratio. Unlike the Mine-by tunnel, the TSX tunnel was excavated parallel to the major principal in situ stress of 60 MPa and using drilling and blasting method. The major horizontal and minor vertical cross sectional axes of the excavation were at 11° from the 45 MP intermediate and 11 MPa minor principal in situ stresses, respectively.

The ESS tunnels M1 and U1 were 3-m high ovaloid openings with aspect ratio of 2.2:1. Both tunnels were excavated parallel to 45 MPa intermediate principal in situ stress using drilling and blasting. The M1 tunnel had a major cross sectional axis in the horizontal direction making 11° to the major principal in situ stress of 60 MPa and a vertical minor axis 11° to the minor principal in situ stress of 11 MPa. The U1 tunnel, on the other hand, was excavated so that its major and minor axes coincide with the direction of major and minor principal in situ stresses thereby minimizing induced stresses.

Table 4.2 shows the parameters of the proposed in situ model used for the Mine-by tunnel with mechanical excavation and TSX and ESS (M1 and U1) tunnels with drilling and blasting excavation. Other model parameters include Young's modulus of 60 GPa, Poisson's ratio of 0.25, tensile strength of 3.7 MPa and dilation angle of 30°. It has been shown that dilation mainly affects displacements around excavations. The plastic zone, on the other hand, is relatively insensitive to dilation and a constant dilation angle model can adequately capture the zone of failure (Zhao and Cai, 2010; Walton and Diederichs, 2015). Figs. 4.14-4.16 show the observed and simulated zone of failure around the tunnels.

Table 4.2 Parameters of the proposed model for in situ behavior of Lac du Bonnet granite

Excavation method	c_i (MPa)	c_r (MPa)	φ_i (deg)	φ_r (deg)	ε_r^p (%)
Mechanical excavation	55	5.5	0	42	0.5
Drilling and blasting	48	4.8	0	42	0.5

It can be observed that the model with initial cohesion of 55 MPa can adequately capture the zone of brittle failure around the Mine-by tunnel made by mechanical excavation. Zones of shear failure near the roof is similar to the V-shaped notches formed in situ and the tensile zones on the side well coincide with location of recorded acoustic emissions (Read and Chandler, 2002). As expected, drilling and blasting induce damage to the surrounding rock thereby decreasing its strength. The model with initial cohesion of 48 MPa successfully captured the stability of TSX and ESS (U1) tunnels and zone of failure around the ESS (M2) tunnel.

4.7   Discussion

As shown in Fig. 4.10, the proposed CWFS model for laboratory behavior given by Eqs. (4.2-4.5) can closely capture the stress-strain behavior of intact rock. The parameters of the laboratory model can be best determined from the results of damage-controlled or cyclic loading as illustrated in Section 4.2. In the absence of such data, the model can be calibrated using stress-strain curves from normal uniaxial and triaxial compression tests with monotonic loading at different confining stresses.

While the absolute strength values for granite and limestone samples analyzed in this study are very different, it is useful to examine their relative response. Fig. 4.17 shows the normalized crack damage and peak stress for unconfined samples of granite and limestone. Interestingly, normalized crack damage stress curves for different samples are very similar.
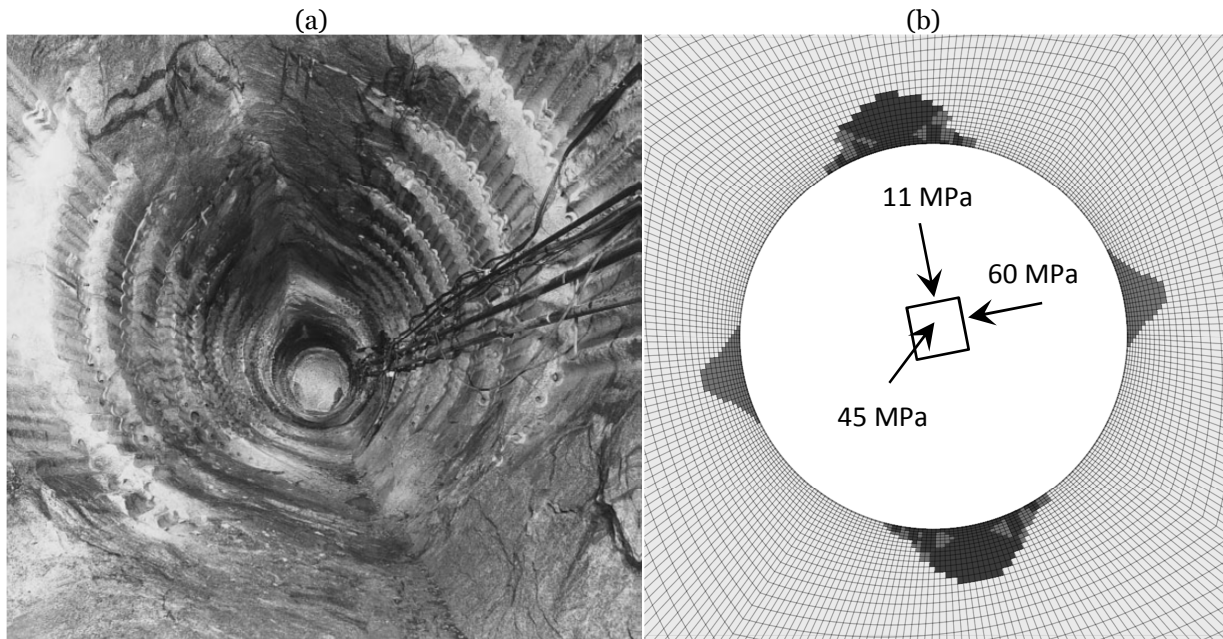
Fig. 4.14 Mine-by tunnel (a) observed zone of failure after Read et al (1998), (b) simulated zone of failure
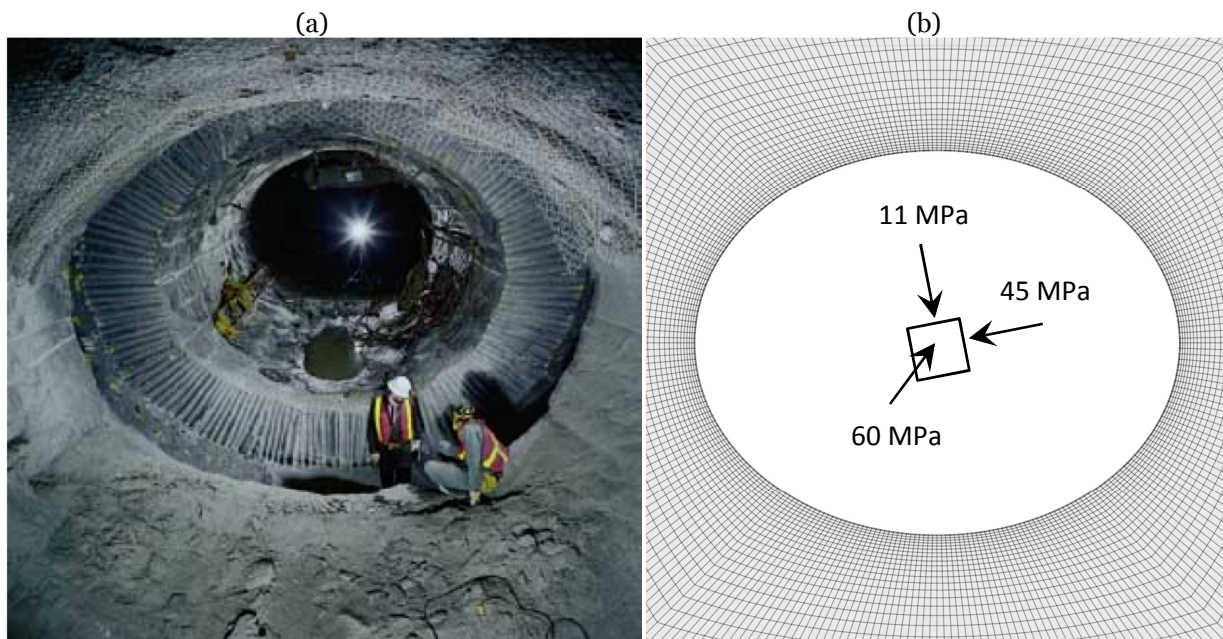
Fig. 4.15 TSX tunnel (a) observed zone of failure after Read and Chandler (2002), (b) simulated zone of failure
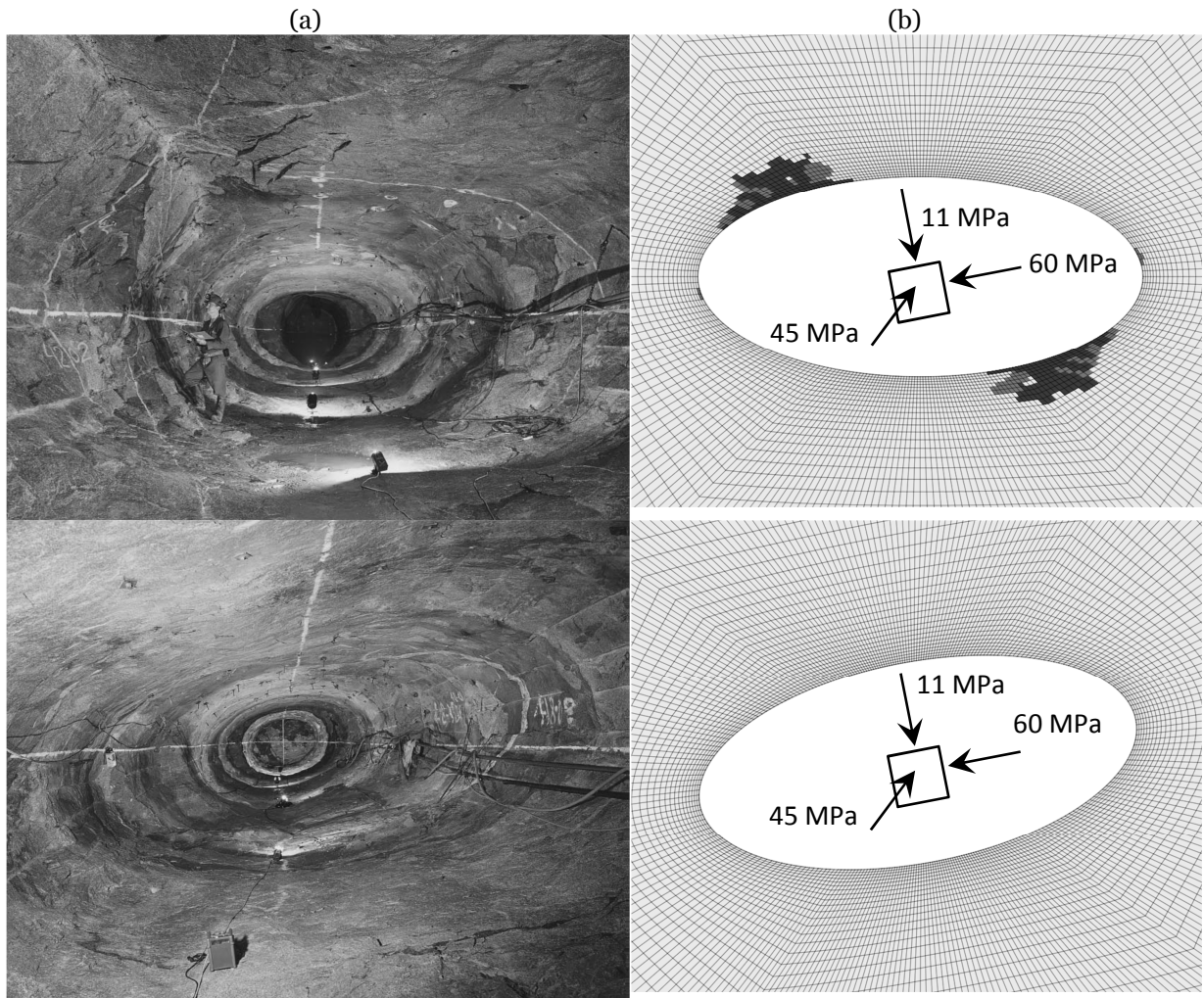
Fig. 4.16 ESS tunnels M1 and U1 (a) observed zone of failure after Read et al (1998), (b) simulated zone of failure
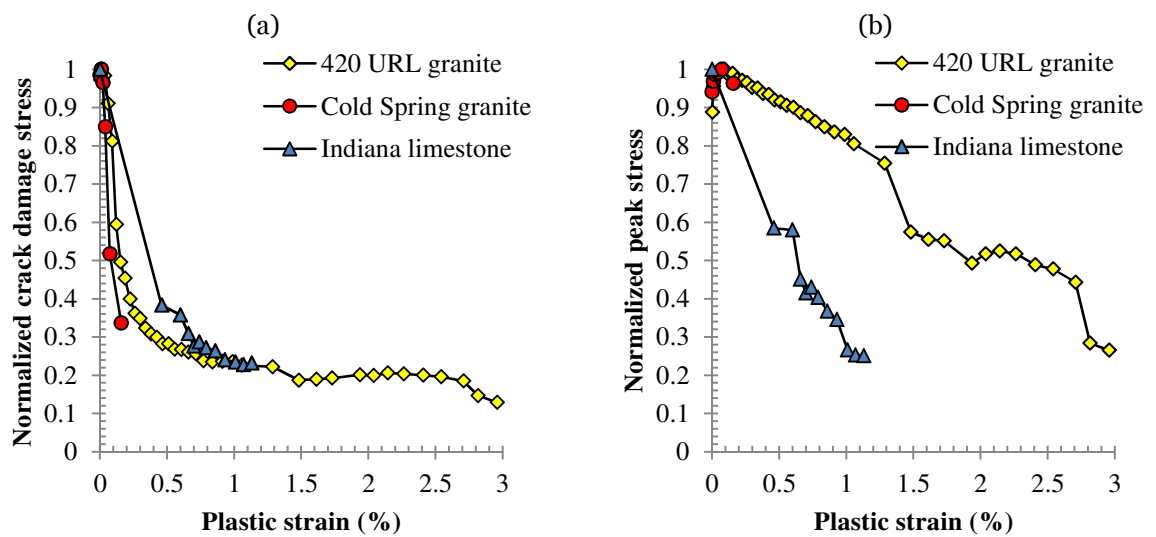
Fig. 4.17 Comparison of crack damage stress and peak stress for unconfined samples of Lac du Bonnet granite from the 420 level of URL and Cold Spring Quarry

The small offset between the curves can be explained in terms of the absolute strength of rocks. Samples of granite from the Cold Spring Quarry with the highest strength are the most sensitive to damage and reach their threshold level at smaller plastic strains compared to the URL samples. On the other hand, samples of Indiana limestone with the lowest strength can experience more plastic strain before reaching the threshold level of crack damage stress. Normalized peak stress curves for the samples of Lac du Bonnet granite from the URL and Cold Spring Quarry are almost identical. Unlike the normalized crack damage stress curves, normalized peak stress curves for the granite and limestone samples are quite different.

The CWFS model for in situ behavior proposed in Eqs. (4.6) and (4.7) is a simplified version of the laboratory model. It not only captures the zone of brittle failure around the URL tunnels, but also respects the fundamental stress-strain characteristics of rocks. As shown by the example in Fig. 4.13, the proposed model captures the gradual degradation of cohesion and mobilization of friction with increasing plastic strain and transition from strain-softening to strain-hardening behavior with increasing confinement.

Fig. 4.18 shows the stress-path for three points within the zone of shear failure around the Mine-by tunnel. Initial and residual strength envelopes obtained from initial and residual values of cohesion and friction angle (Table 4.2) are also shown for reference.
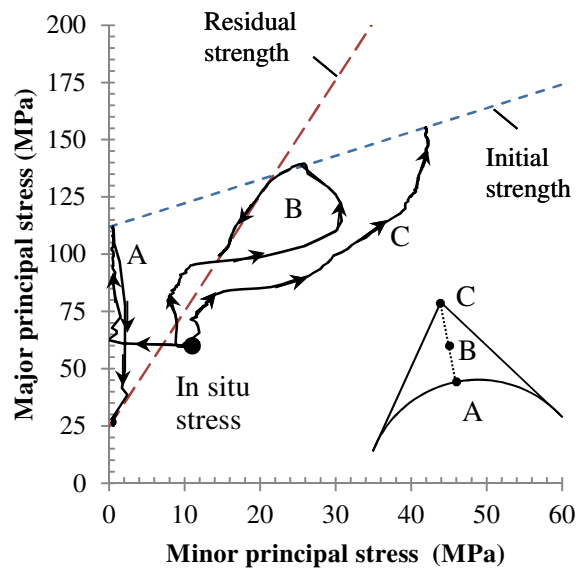
Fig. 4.18 Stress-path for three points within the zone of brittle failure

It can be observed that all curves start from a single point corresponding to initial in situ stresses. Point A on the tunnel boundary experiences rapid reduction of minor principal stress and increase of major principal stress until it reaches the initial strength envelope followed by rapid strain-softening. Point B half-way inside the zone of failure shows increase of major and minor principal stresses until it hits the initial strength envelope

followed by unloading along the residual strength envelope. Point C corresponding to the deepest part of the failure zone experiences continuous increase of major and minor principal stress until it is stabilized on the initial strength envelope. Stress-paths in Fig. 4.18 show that by moving from the tunnel boundary deeper inside the zone of failure, increasing confinement limits the strain-softening behavior.

The proposed CWFS model can also capture the effect of initial damage in rock. As shown in Table 4.2 for example, initial damage caused by drilling and blasting excavation reduced the initial cohesion from 55 to 48 MPa. Fig. 4.19a shows the stress-strain curves from the proposed model with different values of initial cohesion. It can be seen that for a given material with constant values of residual cohesion and friction angle, initial damage can be reflected in the initial cohesion value. Initial damage leads to lower peak strength and reduction of brittleness and strain-softening behavior. Note that in all cases, the residual strength is the same as residual cohesion and friction angle are constant for the given material.

The effect of increasing initial damage on rocks shown in Fig. 4.19a is very similar to the transition of behavior from dense to loose sand and overconsolidated to normally consolidated clays in Fig. 4.19b. In the case of sand and clay, initial strength at low displacements depends on initial density and micro-structures within the soil whereas at higher displacements, the structure is fully destroyed and residual strength is solely governed by residual cohesive or frictional forces. This example shows that the proposed model can capture the behavior of a wide range of geo-materials.
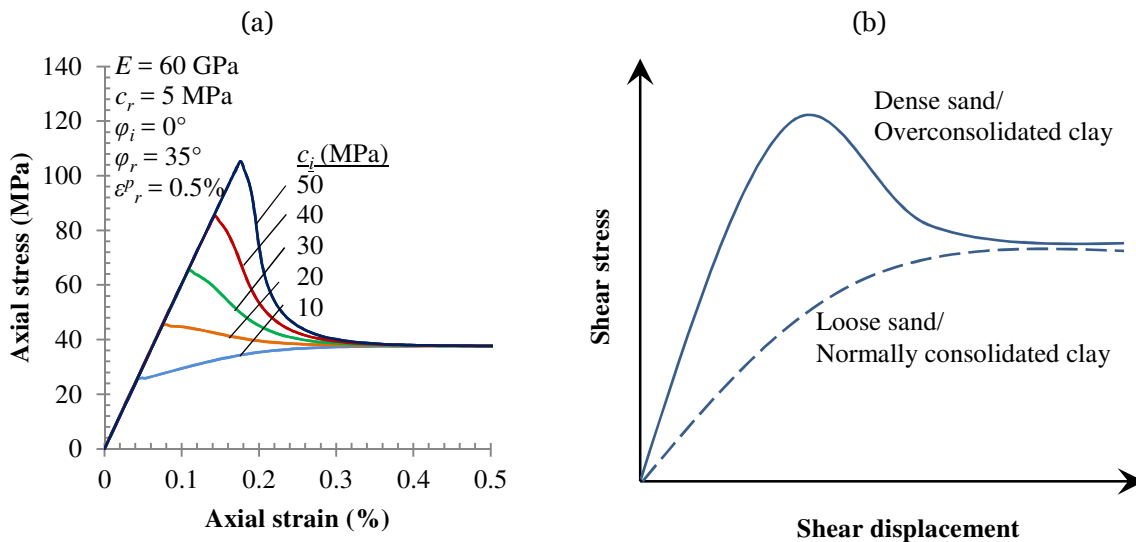
Fig. 4.19 (a) Effect of initial cohesion on the behavior of proposed model, (b) Effect of initial microstructure and transition from strain-softening to strain-hardening in sand and clay

In order to explore the effect of model parameters on the simulated zone of failure, a sensitivity analysis was carried out for the Mine-by tunnel. Fig. 4.20 shows the results of sensitivity analyses in which all the model parameters are identical to those given in
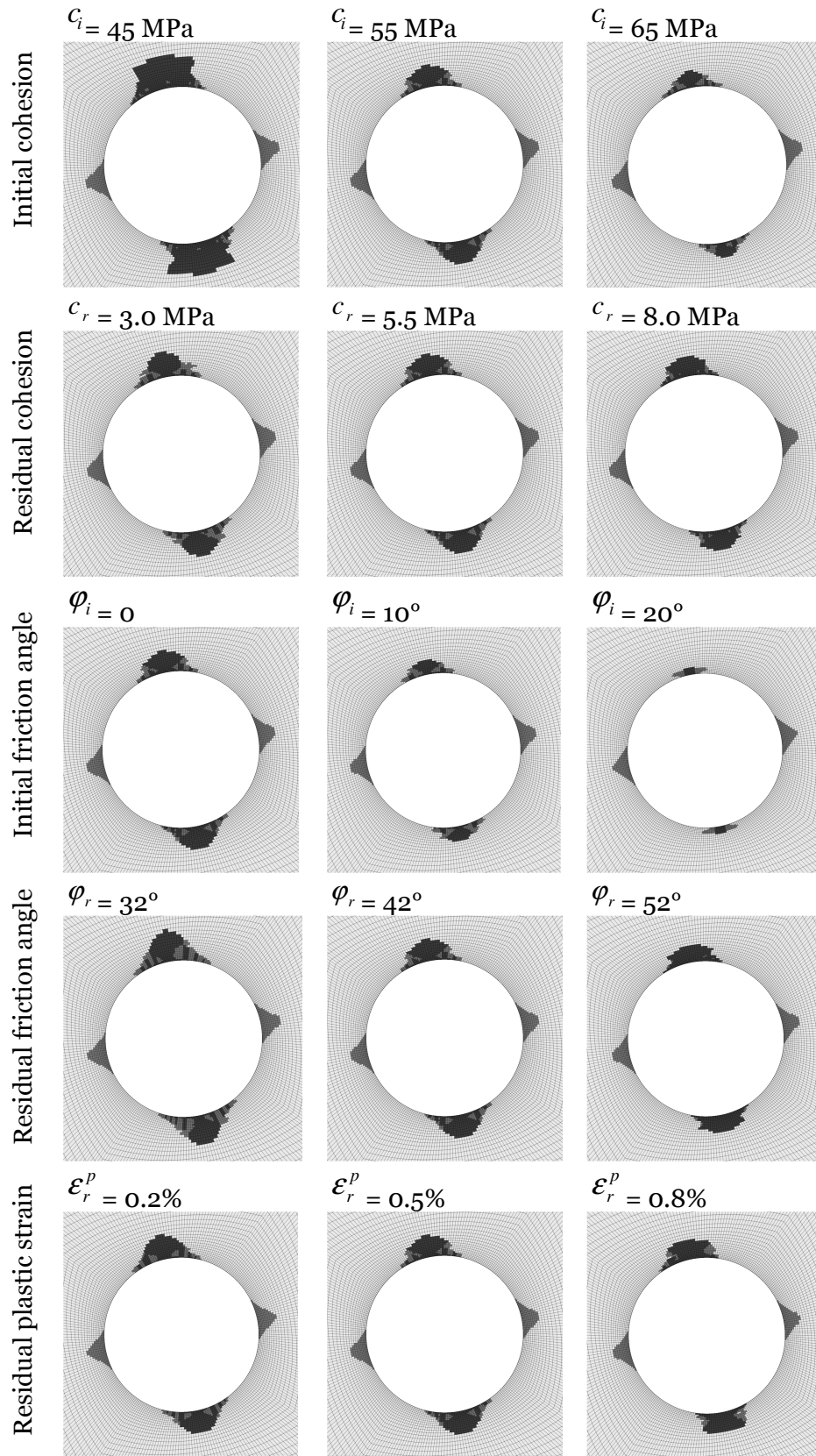
Fig. 4.20 Parametric study of the proposed model for in situ behavior

Table 4.2 (mechanical excavation) except one parameter which is under study and its value is shown in the figure. It can be observed that higher initial and residual cohesion values reduce the depth of failure. Increasing initial and residual friction angle significantly limit the depth and angular extent of failed rock. Shallower zone of failure can be obtained by increasing the amount of plastic strains required for cohesion and friction angle to reach corresponding residual values.

Finally, it is useful to provide some general guidelines on estimating the parameters of the proposed in situ model. Based on the experience gained by application of the model to the URL excavations and also hard rock pillars (Rafiei Renani and Martin, 2016), the following guidelines are suggested as a first estimate for strong rock masses with geological strength index, GSI>70. Initial cohesion can be estimated using:

$$c_i = \frac{\sigma_{c,i}}{2}\left[0.3 + \frac{0.2}{1+\exp(26-0.3GSI)}\right]$$

(4.8)

Residual cohesion values equal to 10% of initial cohesion provided reasonable predictions. As discussed by Martin and Chandler (1994) and concluded from numerical modeling, initial friction angle of zero may be adopted. Residual friction angle depends on the rock type. According to data compiled by Barton and Choubey (1977), average residual friction angle for dry igneous, sedimentary, and metamorphic rocks can be estimated as 34, 33, and 29°, respectively. A value of 0.5% for plastic strain corresponding to residual cohesion and friction angle provided reasonable results and may be used as a first estimate.

4.8   Conclusions

Results from damage-controlled confined tests on samples of Lac du Bonnet granite and Indiana limestone were analyzed to explore the gradual process of cohesion degradation and friction mobilization in the lab. As damage accumulates within the sample, cohesion decreases and friction angle increases. Cohesion degradation curves obtained from tests at different levels of confining stress are very similar while friction mobilization curves show lower values at higher confinements. The theoretical model proposed for laboratory behavior closely matched the stress-strain curves from damage-controlled tests at different confinement levels.

The current CWFS model for capturing in situ brittle failure was analyzed and it was shown that using straight lines for cohesion degradation and friction mobilization along with different plastic strains for residual cohesion and friction angle is fundamentally problematic and gives implausible stress-strain curves. The proposed CWFS model with smooth curves and identical plastic strains for residual cohesion and friction was shown to eliminate the problem and provide reasonable behavior at a fundamental level.

The proposed model for in situ behavior was implemented in FLAC3D and used to simulate the behavior of Mine-by, TSX, and ESS (M1 and U1) excavations at the 420 level of URL.

The results of numerical analysis showed a close agreement between the observed and predicted zone of brittle failure. Analyzing the stress-path followed by different points within the zone of brittle failure showed that by moving from the excavation boundary inside the breakout, confining stress increases which restrains the strain-softening behavior. Parametric studies showed that increasing initial and residual values of cohesion and friction angle limits the depth and angular extent of failure zone. Finally, general guidelines were suggested for estimating the parameters of the proposed model for in situ brittle failure of good quality rock masses.

References

Barton, N., Choubey, V. (1977). The shear strength of rock joints in theory and practice. Rock Mechanics 10:1-54. Vienna: Springer.

Bieniawski ZT (1967) Mechanism of brittle fracture of rock, parts I, II and III. Int J Rock Mech Min Sci Geomech Abstr. 4(4):395–430.

Brown E. T. (1981). Rock Characterization Testing and Monitoring, ISRM Suggested Methods. pp. 107-127. Pergamon Press, Oxford.

Diederichs, M.S. (2007). The 2003 Canadian Geotechnical Colloquium: Mechanistic interpretation and practical application of damage and spalling prediction criteria for deep tunnelling. Can Geotech J, 44:1082-1116.

Edelbro C, Sjoberg C, Malmgren L, Dahner-Lindqvist C (2012) Prediction and follow-up of failure and fallouts in footwall drifts in the Kiirunavaara mine, Can Geotech J, 49:546-559.

Hajiabdolmajid, V., Kaiser, P.K., Martin, C. D. (2002) Modelling brittle failure of rock. International Journal of Rock Mechanics and Mining Sciences, 39, 731-741.

Itasca Inc. (2009). FLAC3D, Fast Lagrangian Analysis of Continua in 3 Dimensions. Version 4.00. Minneapolis.

Lajtai E. Z. and Gadi A. M. (1989). Friction on a granite to granite interface. Rock Mech. Rock Eng, 22, 25-49.

Martin CD (1993) The strength of massive Lac du Bonnet granite around underground opening. Ph.D. thesis, Dept of Civil & Geological Engineering, University of Manitoba, Winnipeg.

Martin CD, Chandler N. (1994) The progressive fracture of Lac du Bonnet granite. Int J Rock Mech Min Sci, 31(6):643–59.

Martin CD, Stimpson B (1994) The effect of sample disturbance on laboratory properties of Lac du Bonnet granite. Can Geotech J, 31:692–702.

Rafiei Renani, H., Martin, CD., Modelling the progressive failure of hard rock pillars, Rock Mechanics and Rock Engineering, Under review.

Read, RS, Chandler, NA, Dzik, EJ. (1998). In situ strength criteria for tunnel design in highly-stressed rock masses. International Journal of Rock Mechanics and Mining, 35(3), 261-278.

Read, RS, Chandler, NA. (2002) An approach to excavation design for a nuclear fuel waste repository -the thermal-mechanical stability study final report, Ontario Power Generation, Nuclear Waste Management Division Report No: 06819-REP-01200-10086-R00.

Schmidtke R. H. and Lajtai E. (1985) The long-term strength of Lac du Bonnet granite. Int. J. Rock Mech. Min. Sci. & Geomech. Abstr. 22, 461-465.

Walton, G., Diederichs, M. (2015) Dilation and post-peak behaviour inputs for practical engineering analysis. Geotech Geol Eng, 33: 15–34.

Walton, G., Diederichs, M., Punkkinen, A. (2015) The influence of constitutive model selection on predicted stresses and yield in deep mine pillars – A case study at the Creighton mine, Sudbury, Canada. Geomech Tunnelling, 8: 441–449.

Zhao, XG, Cai, M. (2010). Influence of plastic shear strain and confinement-dependent rock dilation on rock failure and displacement near an excavation boundary. Int J Rock Mech Min Sci, 47: 723-738.

Chapter 5

Modelling the progressive failure of hard rock pillars[4]

5.1. Introduction

Estimating the strength of pillars is a necessary step in the design of underground mines. In conventional mining methods such as room and pillar operations, economic incentives point towards higher excavation ratios by leaving smaller pillars between the stopes while safety and stability requirements favor wider stronger pillars. In some mining methods such as caving operations, the excessive yielding of the pillars between optimized drawpoints can jeopardize the mining operation. Therefore, design of pillar poses a somewhat unique challenge to rock engineers where simple conservative approaches frequently used in other design methods are no longer acceptable. The behavior of pillar under elevated loads should be predicted accurately.

The most straight-forward method for estimation of pillar strength is using empirical formulas based on the analysis of large numbers of pillars in different mines. As in any empirical method, however, it is essential to note the conditions and ranges of variables in the data sets used for developing the formulas. Many of the pillars in the empirical data sets have limited width to height ratio and occur at relatively shallow depths in high quality rock masses (Lunder and Pakalnis, 1997; Martin and Maybee, 2000; Kaiser, 2011). Extending the application of empirical formulas beyond these ranges is unwarranted. In addition, the approach is very simplified and the effect of many parameters such as the conditions of roof and floor, pillar-foundation interface and in situ stress ratio cannot be explored by the empirical formulas. Finally, these formulas only estimate the pillar strength while knowledge of the pre- and post-peak behavior is also important in mining operations.

Another approach to pillar design is using numerical modeling. This method can take into account most of the variables and complexities affecting pillar behavior. In addition, the complete pillar behavior, from initial loading to post-peak, can be captured. However, realistic modeling of pillars requires a good knowledge of material behavior and implementing a representative constitutive model.

---

[4] A version of this chapter is submitted as a paper to the journal of Rock Mechanics and Rock Engineering

The focus of this paper is the application of a Cohesion-Weakening Friction-Strengthening (CWFS) model implemented into the finite difference code FLAC3D (Itasca Inc., 2009) to determine the behavior of hard rock pillars. Empirical formulas and factors affecting pillar strength are reviewed. New pillar strength formulas based on empirical evidence and modeling results are presented. The merits of the CWFS model in simulating brittle failure are illustrated. Case studies are used to verify the proposed modelling approach.

5.2. Empirical formulas for strength of hard rock pillars

Following the failure of Coalbrook coal mine in 1960, extensive research was initiated in South Africa to establish the strength of coal pillars. One of the early works is due to Salamon and Munro (1967) who analyzed 125 cases of coal pillar failure and expressed the strength of pillar as a power function of its width and height. The findings of Salamon and Munro (1967) were used by Hedley and Grant (1972) to analyze 28 hard-rock rib pillars in the Elliot Lake uranium mines and proposed the same power function with modified exponent. Table 5.1 summarizes empirical formulas that have been reported for the design of hard rock pillars. As pointed out by Bieniawski (1992) and Lunder and Pakalnis (1997), and evident from Table 5.1, pillar strength is influenced by the size effect and shape effect.

Table 5.1 Empirical formulas for hard rock pillar strength, σ_p (W and H are the width and height of pillar in metres, respectively, σ_c is the intact laboratory uniaxial compressive strength of rock and κ is the mine pillar friction term

Reference	Pillar strength, σ_p	σ_c (MPa)	No. of pillars	Rock mass
Hedley & Grant (1972)	$133\left(W^{0.5}/H^{0.75}\right)$	230	28	Quartzite
von Kimmelmann et al (1984)	$65\left(W^{0.46}/H^{0.66}\right)$	94	57	Metasediments
Krauland & Soder (1987)	$35.4\left[0.778+0.222(W/H)\right]$	100	14	Limestone
Potvin et al (1989)	$0.42\sigma_c(W/H)$	-	23	Canadian shield
Sjoberg (1992)	$74\left[0.778+0.222(W/H)\right]$	240	9	Limestone/Skarn
Lunder & Pakalnis (1997)	$0.44\sigma_c(0.68+0.52\kappa)$	-	178	Hard rocks

5.2.1. Size effect

Size effect refers to the reduction of strength by increasing the size of the test sample. It is a fundamental characteristic of heterogeneous materials and is caused by the increasing number of weaker and softer elements within larger samples. As suggested by Bieniawski

(1968) and Martin et al (2012), there is a critical size above which there will be no further reduction of strength with increasing size. Determination of the critical size requires testing of very large samples. Performing such tests is very difficult and costly and the number of tests on sufficiently large samples is very limited. The results of independent large scale tests carried out on diorite (Pratt et al, 1972) and coal (Bieniawski, 1968) suggest that the critical size for these materials is about 1 m.

In order to estimate the strength of large scale pillars, it is useful to find a relationship between the uniaxial compressive strength of intact rock and the pillar strength. This relationship bridges the size gap between the laboratory samples and large-scale pillars. To this end, a reference pillar, representative of large-scale pillars is defined. The size of the reference pillar must be no smaller than the critical size. Since the strength of the reference pillar is compared with strength of intact laboratory sample, the width to height ratio of the reference pillar must also be similar to that of laboratory specimen. Choosing the width of 1 m for the reference pillar ensures that the results will be valid for larger pillars (no size effect beyond the critical size of 1 m). In order to avoid the introduction of shape effects in this analysis, the width to height ratio of pillar is chosen as 0.5 to be similar to the diameter to length ratio of the laboratory test sample (ASTM, 2004).

Strength of the reference pillar (W=1m and H=2m) can be estimated from the empirical formulas. The ratio of the reference pillar strength to intact uniaxial compressive strength is defined as the in situ strength factor K. Using the empirical formulas in Table 5.1, in situ strength factor K ranges from 0.21 to 0.44 with the average value of 0.31. Based on comprehensive back analysis of pillars at the Quirke mine, Swan (1985) also found that the ratio of mean pillar strength to mean intact uniaxial compressive strength is 0.33 (Fig. 5.1).
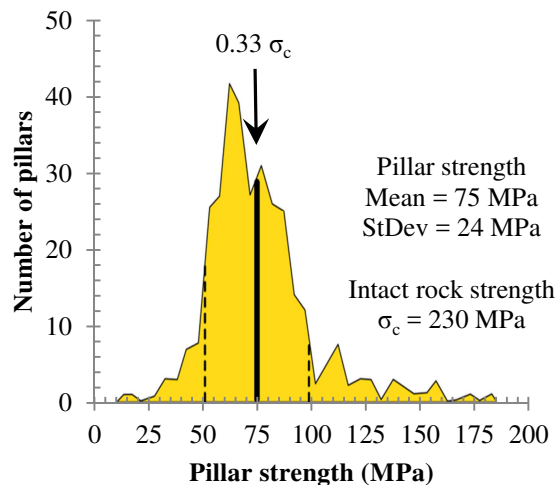
Fig. 5.1 Distribution of pillar strength in the Quirke mine (Swan 1985)

5.2.2.   Shape effect

The strength of pillars is also influenced by the shape of pillar expressed as the width to height ratio in the empirical formulas in Table 5.1. The relationship between the pillar strength normalized by the uniaxial compressive strength and width to height ratio of the pillar is shown in Fig. 5.2. It can be observed that the pillar strength increases with increasing the width to height ratio.
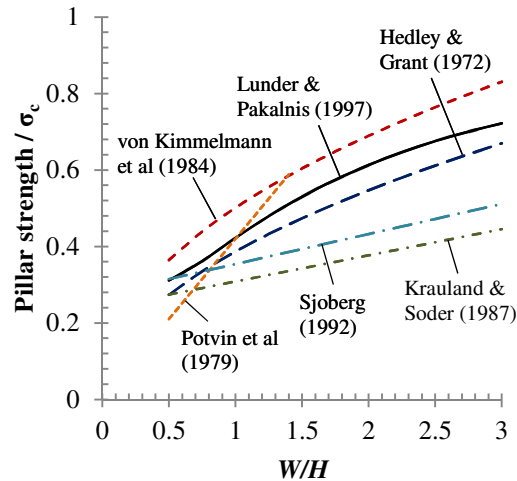
Fig. 5.2 The effect of shape on pillar strength based on empirical formulas

This trend is similar to the one observed in the laboratory compression tests on specimens with different diameter to length ratios (e.g., Hawkes and Mellor, 1970). As in the case of laboratory tests, the actual factor which causes an increased strength for wider pillars is the end constraints which induce higher confinements within the pillar.

5.3.   Semi-analytical formula for strength of hard rock pillars

In order to explore the relationship between the width to height ratio and induced confinement, a series of uniaxial compression tests were carried out on elastic rib pillars using the finite difference code FLAC3D. Fig. 5.3 shows the profile of minor principal stress (confinement) normalized by the average major principal stress (average pillar stress) across the mid-height of pillars with difference width to height ratios. It can be observed that increasing the width to height ratio has a significant effect on the confinement within the pillar.

It is also worth noting that for a pillar with W/H ratio of 0.5, tensile stresses are induced within the pillar. It suggests that the behavior of very slender pillars (W/H<0.5) is governed by tensile mechanisms, splitting and buckling. Analyzing these modes of failure requires special considerations and in beyond the scope of this paper.

Fig. 5.4a shows the average normalized confinement as a function of width to height ratio derived from Fig. 5.3. This relationship can be expressed as:

$$\frac{\bar{\sigma}_3}{\bar{\sigma}_1} = -0.1 + 0.2\left(\frac{W}{H}\right) - 0.034\left(\frac{W}{H}\right)^2 + 0.002\left(\frac{W}{H}\right)^3$$

(5.1)

where $\bar{\sigma}_3$ and $\bar{\sigma}_1$ are the average minor and major principal stresses across the mid-height of the pillar.
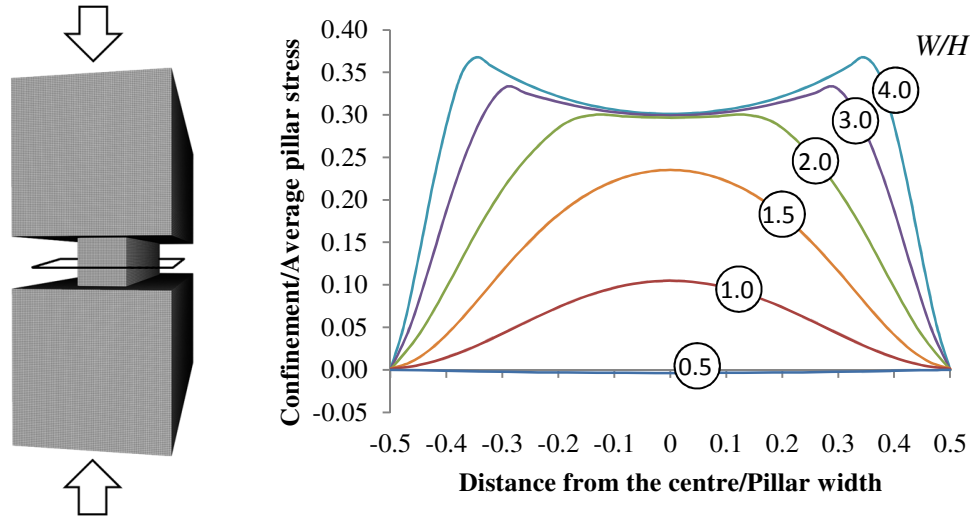
Fig. 5.3 Profiles of normalized confinement at the mid-height of elastic pillars with different *W/H* ratios
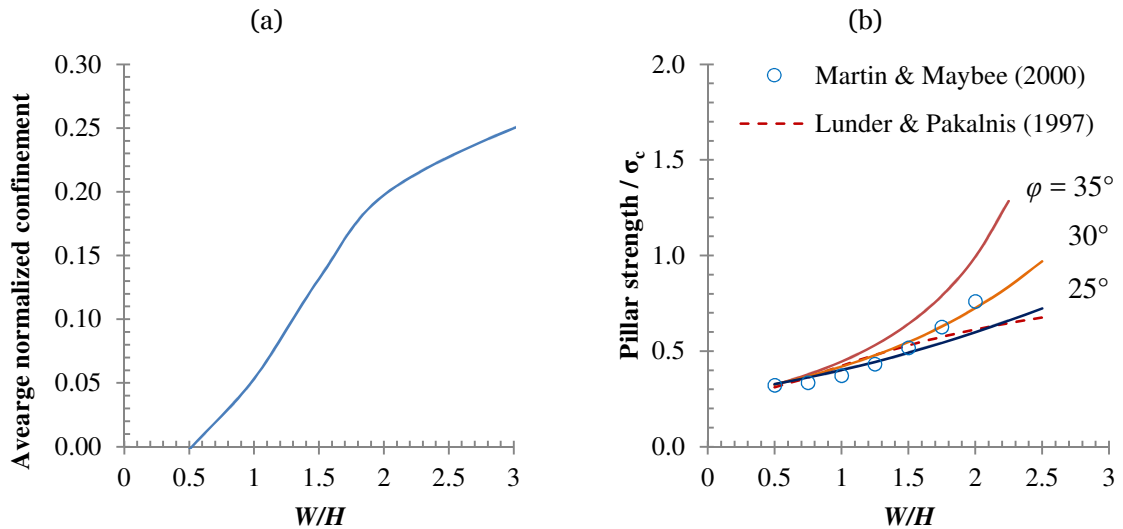
Fig. 5.4 (a) Relationship between average confinement normalized by average pillar stress and *W/H* ratio, (b) semi-analytical relationship between pillar strength and *W/H* ratio

In order to quantify the effect of confinement on pillar strength, it is useful to consider a failure criterion. The Mohr-Coulomb criterion for in situ rock mass can be expressed as:

$$\sigma_1 = \sigma_{c,M} + \sigma_3 \tan^2\left(\frac{\varphi}{2} + \frac{\pi}{4}\right)$$

(5.2)

where σ_1 and σ_3 are the major and minor principal stress and $\sigma_{c,m}$ is rock mass uniaxial compressive strength given by:

$$\sigma_{c,m} = 2c \tan\left(\frac{\varphi}{2} + \frac{\pi}{4}\right)$$

(5.3)

where c and φ are the cohesion and friction angle of rock mass. Rock mass uniaxial compressive strength can also be expressed in terms of the intact uniaxial compressive strength and the in situ strength factor K ($\sigma_{c,m} = K\sigma_c$).

While the stress distribution and strength properties within the pillar are non-uniform, it is instructive to take a simplified approach and consider the pillar as a single element with equivalent stress and strength values. The stresses can be approximated by the average principal stresses across the mid-height, $\bar{\sigma}_3$ and $\bar{\sigma}_1$. Substituting Eq. (5.1) into Eq. (5.2) gives:

$$\sigma_1 = \frac{K\sigma_c}{1 + \left[0.1 - 0.2\left(\frac{W}{H}\right) + 0.034\left(\frac{W}{H}\right)^2 - 0.002\left(\frac{W}{H}\right)^3\right]\tan^2\left(\frac{\varphi}{2} + \frac{\pi}{4}\right)}$$

(5.4)

As discussed in Section 5.2.1, the in situ strength factor for hard rock pillars is about 0.33. The value of effective friction angle in Eq. (5.4) should respect the fact that pillar strength is significantly affected by the presence of weak planes and joints of varying lengths and directions within the pillar. Fig. 5.4b shows the results of Eq. (5.4) with the in situ strength factor of 0.33 and effective friction angle of 25°, 30° and 35°. It can be observed that using an effective friction angle of 30° matches the numerical results of Martin and Maybee (2000). The results of using an effective friction angle of 25° are in close agreement with the empirical formula proposed by Lunder and Pakalnis (1997). Adopting this value, the final semi-analytical strength formula for hard rock pillars is derived:

$$\sigma_p = \frac{\sigma_c}{3.74 - 1.48\left(\frac{W}{H}\right) + 0.25\left(\frac{W}{H}\right)^2 - 0.015\left(\frac{W}{H}\right)^3}$$

(5.5)

Although the empirical formula by Lunder and Pakalnis (1997) and the semi-analytical pillar formula in Eq. (5.5) give similar results for pillars with W/H ratios of less than 2, the semi-analytical formula predicts higher strength values for wider pillars. As discussed later, it is an important feature which is in keeping with the results of numerical models.

5.4. Progressive failure of hard rocks

While the pillar formulas provide an initial estimate of the pillar peak strength, they cannot capture the effect of complex geometries, in situ stress fields, and material behavior. Numerical modeling provides a broader and more detailed insight into the pre- and post-peak behavior of pillars. However, obtaining realistic results from numerical models strongly depends on the implementation of a representative constitutive model. In order to determine a representative material model for a specific problem, it is necessary to analyze the process of deformation and mechanisms of failure observed in the laboratory and in situ. Such analysis provides invaluable information for selecting a representative material model, which is most capable of capturing the observed mechanisms.

5.4.1. Laboratory observations

Using a series of damage-controlled triaxial tests on Lac de Bonnet granite, Martin and Chandler (1994) showed that contrary to general assumption, cohesion and friction are not mobilized simultaneously. They showed that as stress level increases and damage accumulates within the material, the cohesive component of strength decreases and frictional component increases. The evolution of cohesion and friction for Lac de Bonnet granite under uniaxial compression is shown in Fig. 5.5a.
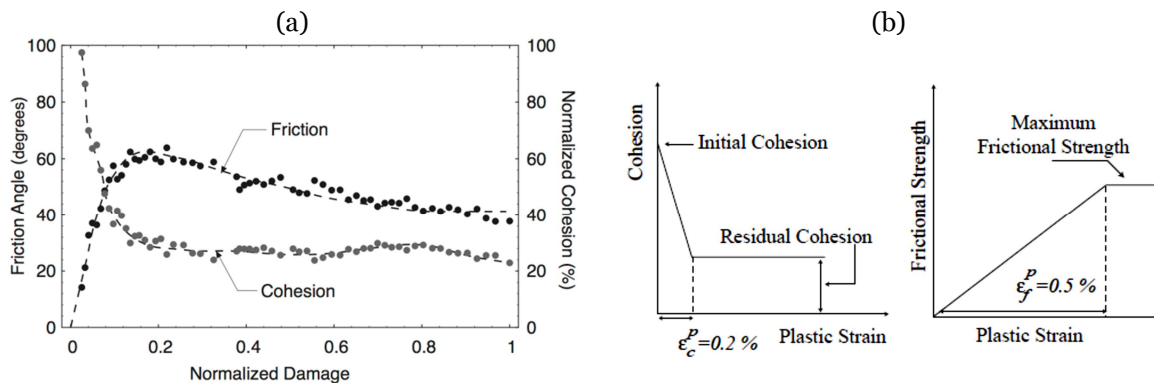
Fig. 5.5 Evolution of cohesion and friction with damage (a) Test results on Lac de Bonnet granite (Martin and Chandler, 1994), (b) Numerical model for the Mine by tunnel (Hajiabdolmajid et al, 2002)

5.4.2. In situ observations

Pritchard and Hedley (1993) made detailed observations of the evolution of deformation and process of failure in the hard rock pillars from the Elliot Lake region. Their observations clearly show that minor spalling marks the initiation of failure. Loss of the detached spalled rock induces increased loads on the pillar causing a progressive process of spalling and slabbing. Gradual spalling results in the loss of load carrying capacity of the pillar and finally leaves a narrow hour glass shaped pillar which is then vulnerable to shear failure along the weak structural features such as bedding planes and joints. Martin (1997) observed a similar

process of progressive failure around the Mine by test tunnel at the Underground Research Laboratory (URL) in Canada.

5.4.3. Numerical modeling

Hajiabdolmajid et al (2002) observed that the conventional models were not able to reproduce the mechanisms of progressive failure observed around underground tunnels in good quality rock masses. Based on the experimental and theoretical works of Martin and Chandler (1994) on progressive failure, Hajiabdolmajid et al (2002) proposed the Cohesion-Weakening Friction-Strengthening (CWFS) model to capture the progressive failure process. In this model, both cohesion and friction angle are expressed as functions of plastic strain ε^p. Fig. 5.5b shows the variation of cohesion and friction angle adopted by Hajiabdolmajid et al (2002). As can be seen, the values of cohesion and friction angle change up to a certain value of plastic strain after which the values remain constant. The CWFS model successfully reproduced the observed failure pattern observed in the field.

5.5. Numerical modeling of hard rock pillars

Considering the laboratory and in situ evidence for the CWFS model, it was used in FLAC3D to simulate the progressive failure of hard rock pillars. The following equations are proposed to specify the cohesion degradation and friction mobilization as smooth functions of plastic strain:

$$c = c_r + (c_i - c_r)\left(2 - \frac{2}{1+\exp\left(-3.66\dfrac{\varepsilon^p}{\varepsilon^p_{c,r}}\right)} \right) \tag{5.6}$$

$$\varphi = \varphi_i + (\varphi_r - \varphi_i)\left(\frac{2}{1+\exp\left(-3.66\dfrac{\varepsilon^p}{\varepsilon^p_{\varphi,r}}\right)} - 1 \right) \tag{5.7}$$

where c_i and c_r are the initial and ultimate (degraded) values of cohesion ($c_i \geq c_r$), φ_i and φ_r are the initial and residual (mobilized) values of friction angle ($\varphi_i \leq \varphi_r$), and $\varepsilon^p_{c,r}$ and $\varepsilon^p_{\varphi,r}$ are plastic strains at which cohesion and friction angle are within 5% of their residual values, respectively.

Implications of Eqs. (5.6) and (5.7) on cohesion degradation and friction mobilization are illustrated in Fig. 5.6a using an example. It can be observed that increasing damage and

plastic strain causes a gradual loss of cohesion and mobilization of friction. Compared to Fig. 5.5, it is evident that the smooth and non-linear cohesion degradation and friction mobilization model specified by Eqs. (5.6) and (5.7) capture the experimental results more closely than a linear model with sharp changes. As shown in Fig. 5.6b, the proposed model also leads to realistic stress-strain curves and captures the fundamental characteristics of transition from strain-softening to strain-hardening behavior with increasing confinement.
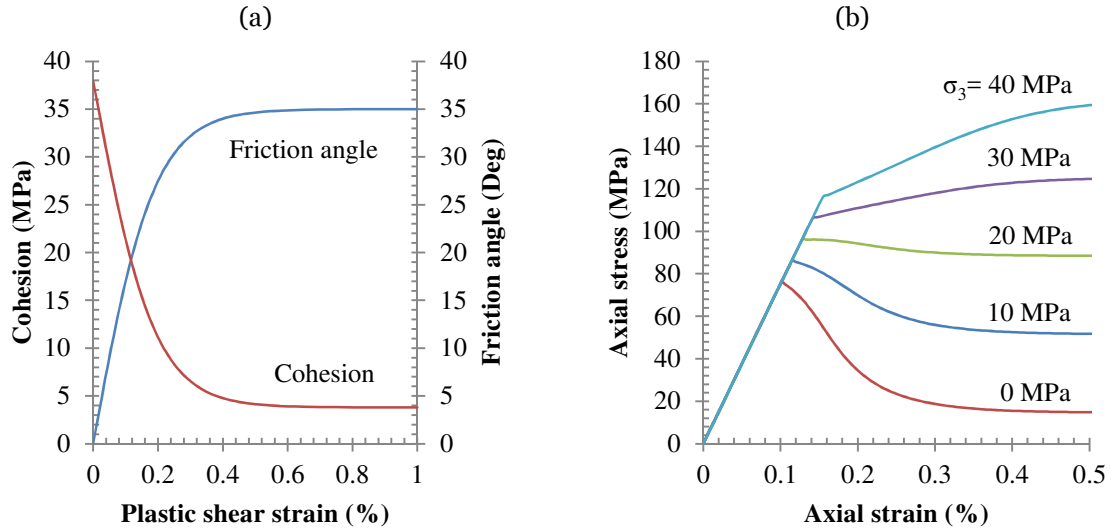
Fig. 5.6 CWFS model for the rock mass at the Elliot Lake mine (a) Cohesion loss and friction mobilization, (b) stress-strain curves under uniaxial and triaxial compression

The geometric boundaries of the model were chosen to minimize the undesirable boundary effects. The vertical extent of the model was 15 times the height of the pillar. The distance between horizontal boundaries was 3 times the width of the pillar representing a road way twice as wide as the pillar. A uniform mesh with square elements was used throughout the model with 30 elements across the width of the pillar. The boundary conditions of the model consisted of fixed horizontal displacement at the sides, fixed vertical displacement at the bottom, and constant velocity on the top inducing compression within the pillar. The following case studies were analyzed under plane strain conditions. A three-dimensional model was also analyzed to verify the applicability of the findings to pillars with complex geometries.

The overall deformation behavior of the pillar was quantified using the total vertical strain across the height of the pillar. The average pillar stress was recorded by averaging the major principal stress over elements within a narrow range of the mid-height of the pillar. The strength of the pillar is determined as the peak value of average pillar stress during deformation. The stresses at the core of the pillar (central element within the pillar) were also monitored.

5.6. Case studies

Two case studies including the documented behavior of hard rock pillars were used to verify the numerical modeling approach.

5.6.1. Case study I: The Elliot Lake mine

The Elliot Lake uranium orebody is located in Ontario, Canada. Tabular deposits of uranium bearing conglomerates were separated by massive quantize beds with thickness of 3-30 m. The orebody was mined using room-and-pillar and stope-and-pillar methods to a depth of 1 km. Based on seismic wave velocity measurements and according to the Q-system, pillars were excavated in "good" to "very good" quality rock masses (Hedley and Grant, 1972; Coats and Gyenge, 1981). Martin and Maybee (2000) assigned a GSI value of 80 to the quartzite rock mass at the Elliot Lake mine.

The parameters of the CWFS model for the pillars at the Elliot Lake mine are given in Table 5.2 where E and υ are rock mass modulus and Poisson's ratio, respectively. The variation of cohesion and friction as smooth functions of plastic strain are shown in Fig. 5.6a. Fig. 5.6b shows the corresponding stress-strain response of the CWFS model under uniaxial and triaxial compression as implemented in a MATLAB code. It can be observed that the stress-strain curves indicate a transition from strain-softening to strain-hardening behavior at confining pressure of about 20 MPa. Notice that unconfined rock mass strength from the CWFS model provides a pillar uniaxial compressive strength which is approximately 1/3 of the laboratory intact uniaxial strength, as discussed in Section 5.2.1.

5.6.2. Case study II: The Selebi-Phikwe mine

The Selebi-Phikwe deposits of nickel and copper are located in Botswana, Southern Africa. The strata-bound sulphide orebody is hosted in highly deformed metasediments of Archaean age. Open stoping and cut-and-fill stoping methods were used to extract the orebody to a depth of 500 m. The average value of rock mass rating (RMR) in the Selebi-Phikwe mine is 85 (von Kimmelmann et al, 1984; Nareetsile, 1998). According to the correlation proposed by Hoek and Brown (1997), a GSI value of 80 is estimated for the sulphide rock mass at the Selebi-Phikwe mine. The parameters of the CWFS model for the pillars at the Selebi-Phikwe mine are given in Table 5.2. The trend of cohesion and friction evolution by accumulated damage and transition from strain-softening to strain-hardening by increasing confinement is similar to those at the Elliot Lake mine shown in Fig. 5.6.

5.6.3. Results

The average stress-strain curves for pillars at the Elliot Lake mine and the Selebi-Phikwe mine are shown in Fig. 5.7. The width to height ratio of pillar ranges from 0.5 to. 3 It can be

observed that pillars with W/H values of 0.5 and 1 show very similar stress-strain curves. For pillars with W/H ratios of 2, there is a slight reduction of stresses after the peak. On the other hand, pillars with W/H ratios of 3 show a significant strain-hardening behavior up to vertical strains of about 1%.

Table 5.2 Parameters of the CWFS model for the case studies

Mine	σ_c (MPa)	E (GPa)	ν	c_i (MPa)	c_r (MPa)	$\varepsilon_{c,r}^p$ (%)	φ_i (deg)	φ_r (deg)	$\varepsilon_{\varphi,r}^p$ (%)
Elliot Lake	230	75	0.25	38.0	3.8	0.5	0	35	0.5
Selebi-Phikwe	94	71	0.25	15.7	1.6	0.5	0	34	0.5
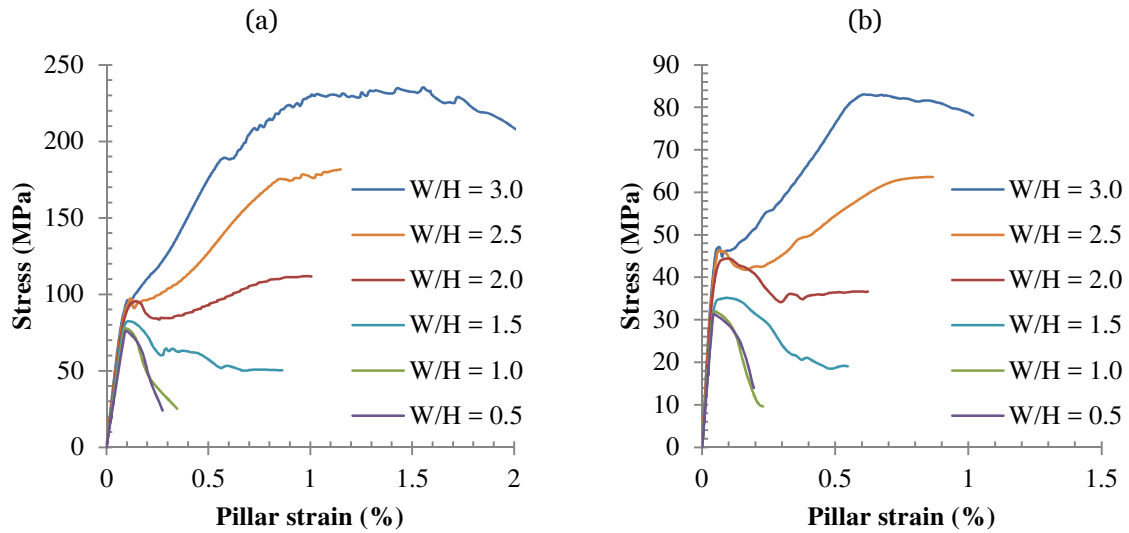
Fig. 5.7 Average vertical stress-strain curves for pillars at (a) the Elliot Lake mine, and (b) the Selebi-Phikwe mine

In order to explore the effect of the CWFS model on the evolution of stresses at the core of pillars, stress path at the core for pillars with W/H ratios of 1 and 2 at the Elliot Lake mine are shown in Fig. 5.8. The initial cohesive strength and ultimate frictional strength envelopes are also shown. From Fig. 5.8, it is clear that for a pillar with a W/H=1, the strength is dominated by the cohesive strength component and there is significant loss in strength while the frictional strength is being mobilized. Such behaviour would be clearly classed as strain weakening and could lead to sudden pillar collapse. This is also illustrated in Fig. 5.9 which illustrates the rapid failure of the pillar W/H=1 as the peak strength is reached.

The location of yielded elements in Fig. 5.9 shows that the CWFS model has captured the progressive nature of failure in hard rock pillars. When average pillar stress reaches about 70% of the peak stress, the first signs of yield are observed at the corners of the pillar. This is

in keeping with the observations of Wagner (1974) who reported the initiation of non-linear behavior of pillars occurred at 70% of peak stress. As loading continues, the process of yielding propagates inside the pillar towards the core. At about 95% of the peak stress, the upper and lower yield zones coalesce and form two distinct break outs on both sides of the pillar. In reality, the two yield zones detach from the pillar leaving an hour glass shaped pillar. Very slight increase in loading after this point causes the two yield zones in both sides to connect and form a through-going shear band. These failure mechanism i.e., initiation of slabbing at the corners, continued spalling and formation of hour glass shaped pillars and finally shear failure of the pillar, are in close agreement with the observations of Pritchard and Hedley (1993) on failure of hard rock pillars.
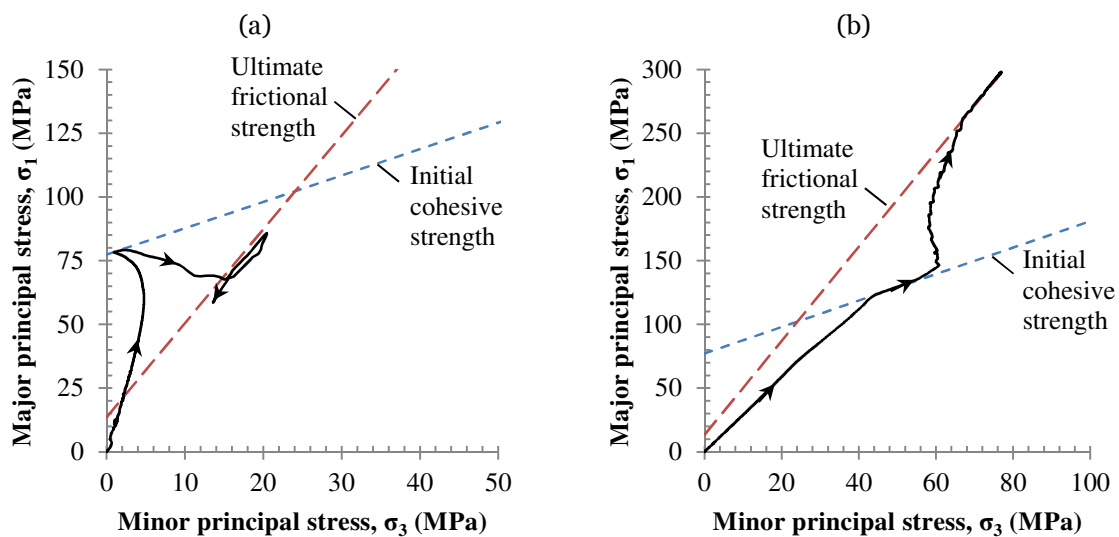
Fig. 5.8 Stress path at the core of pillars at the Elliot Lake mine with (a) $W/H=1$, and (b) $W/H=2$

Fig. 5.10a shows the condition of 28 pillars at the Elliot Lake mines documented by Hedley and Grant (1972). It is worth noting that only 2 pillars were classed as unstable (partially failed) and 3 pillars were noted as failed. The Elliot Lake pillars were analyzed using the CWFS model. The results of the pillar strength formula proposed by Hedley and Grant (1972) as well as the numerical analysis using the CWFS model are also shown in Fig. 5.10a.

In the case of Selebi-Phikwe mine, a total of 57 pillars were documented among which 20 were noted as unstable and 22 were classed as failed. Fig. 5.10b shows the condition of the documented pillars at the Selebi-Phikwe mine, the empirical pillar strength curve proposed by von Kimmelmann et al (1984), and the results of the numerical analysis using the CWFS models.

It can be observed from Fig. 5.10a that both the empirical formulae proposed by Hedley and Grant (1972) and the CWFS model predict similar values of pillar strength for W/H ratios between 0.5 and 2.5. In addition, both models properly separate the stable and unstable/failed pillars at the Elliot Lake mine. However, the empirical formula is concave

downward while the curve corresponding to the CWFS model shows an upward trend. Unfortunately, there are no failed cases with W/H> 1.5 for the Elliot Lake mines to help in determining the right trend.

70% of peak stress

85% of peak stress

95% of peak stress

Post peak
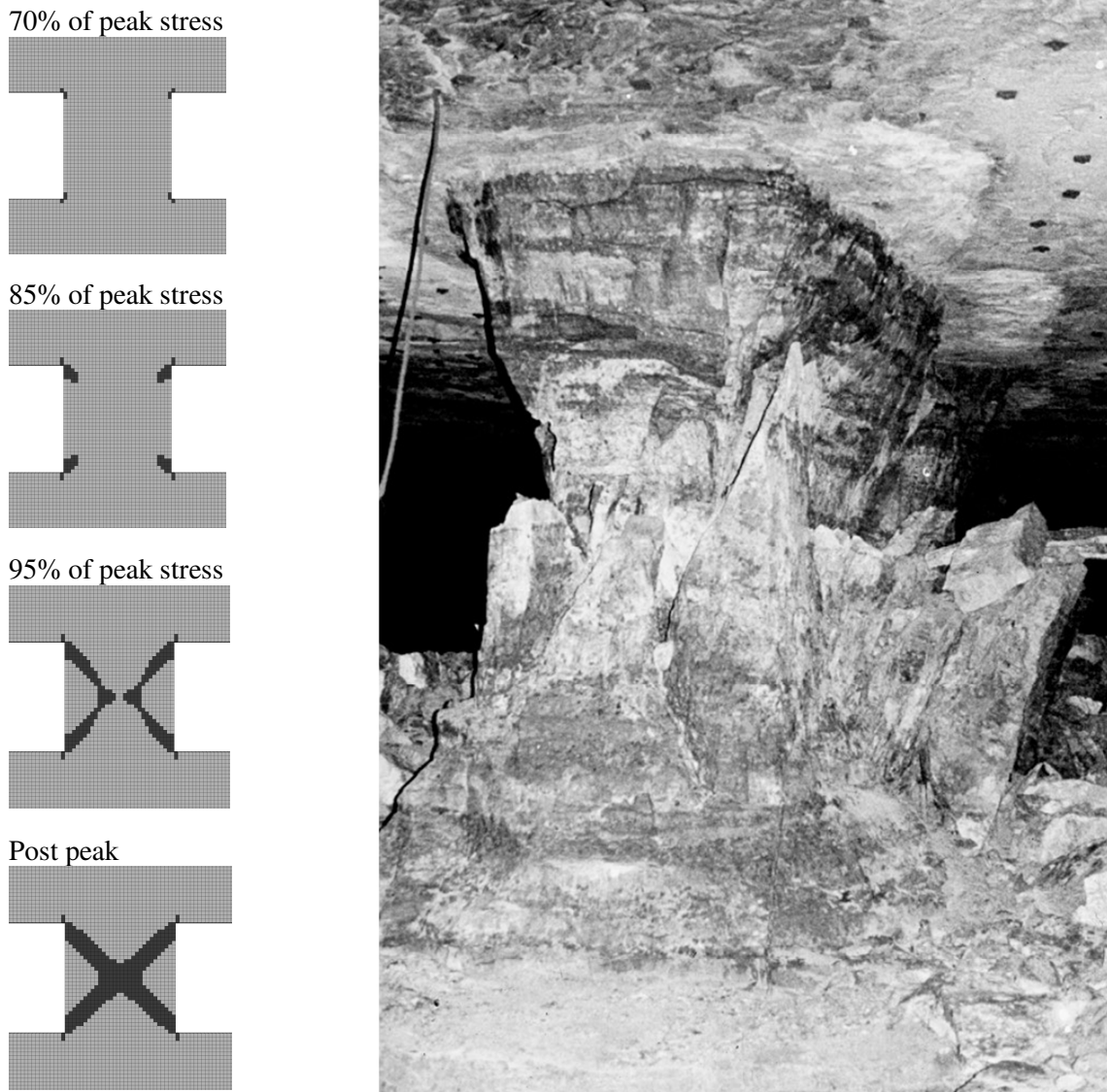
Fig. 5.9 Location of yielded elements for a pillar with *W/H*=1 at the Elliot Lake mine and photo of a crushed pillar, courtesy of Mr. C. Pritchard

Fig. 5.10b shows that the total number of documented pillars and also the percentage of unstable/failed pillars at the Selebi-Phikwe mine are significantly higher than those at the Elliot Lake mine. Hence, it can be more helpful in evaluating different models. It should be noted, however, that there is more scatter in this data set and the boundary between stable and unstable/failed pillars is not as well defined as for the Elliot Lake mine. It can be seen from Fig. 5.10b that the empirical pillar strength curve proposed by von Kimmelmann et al (1984) passes through the cluster of unstable/failed pillar date points. Hence, it overestimates the strength of many unstable/failed pillars. The CWFS model, on the other hand, separates the stable and unstable/failed pillars more effectively. In other words, it

contains almost all the unstable/failed pillars date points. Again, the empirical equation shows a concave downward trend while the curve corresponding to the CWFS model follows an upward trend.
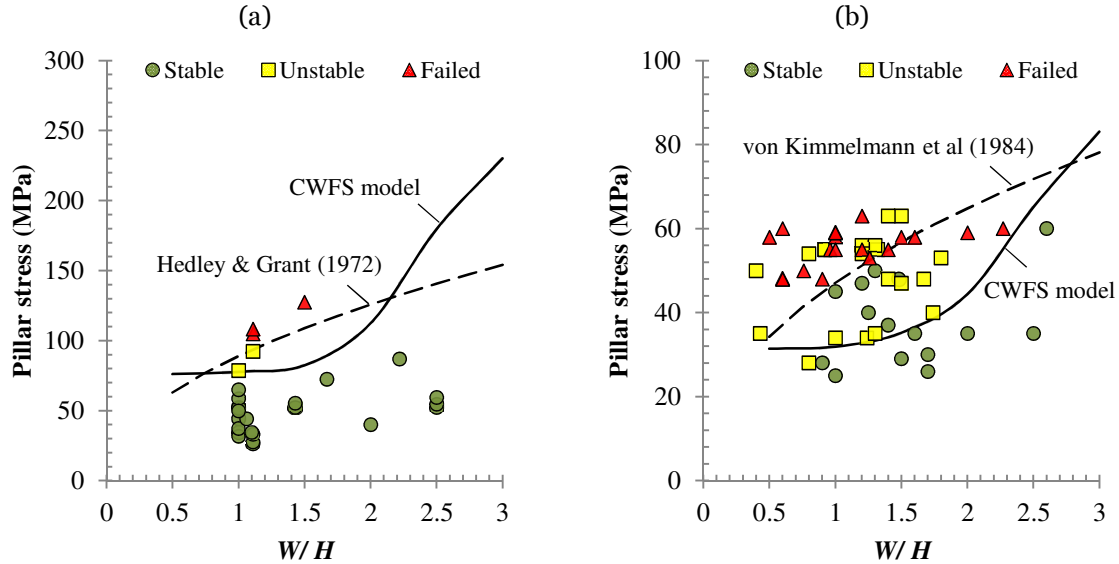
Fig. 5.10 Pillar behavior and predicted strength at (a) the Elliot Lake mine and (b) the Selebi-Phikwe mine

It is useful to express the results of the case studies using the CWFS model in a simple formula by normalizing the pillar stress to the laboratory intact uniaxial compressive strength. The CWFS curves shown in Fig. 5.10 can be approximated by:

$$\frac{\sigma_p}{\sigma_c} = 2.5 - \frac{2.2}{1 + \left(0.22\frac{W}{H}\right)^{2.5}}$$

(5.8)

The CWFS-based pillar strength formula given in Eq. (5.8) can be used for hard rock pillars with W/H>0.5. The equation is applicable to good quality rock masses with GSI greater than 70.

5.7. Discussion

The results of the numerical analysis using the CWFS model presented in Fig. 5.7 capture the fact that wider pillars have higher strength than narrow pillars. In addition, it illustrates that the post-peak strength of narrow pillars (W/H≤1) is significantly lower than the peak strength implying that failure of such pillars can be potentially violent. On the other hand, wider pillars with W/H>2 can maintain their strength and even exhibit strain-hardening behavior after initial yielding. It suggests that the failure of such pillars tend to be more

90

gradual and less violent. In terms of displacements, Fig. 5.7 shows that narrow pillars may lose their load bearing capacity at axial strains as low as 0.1% whereas wide pillars can sustain strains of up to 1% before losing their load bearing capacity. It supports the importance of accurate displacement monitoring for narrow pillars.

Fig. 5.8 illustrates one of the most important aspects of the CWFS model applicable to hard rock pillars. For a pillars with W/H=1, the stress path at the core reaches the initial cohesive strength envelope and then relaxes and follows the ultimate frictional strength envelope corresponding to residual values of cohesion and friction angle. This stress path for low confinement is characteristic of strain-softening ground behavior at the pillar core. When the pillar W/H is increased to 2, on the other hand, the stress path continually moves upward passing the initial cohesive envelope until the ultimate strength envelope is reached. This clearly captures the strain-hardening behavior at the core of wide pillars under high confinements.

It is also worth noting that the major principal stress at the core of pillars can reach much higher values than the overall average pillar strength. Fig. 5.11 shows the comparison between pillar strength (peak average vertical stress across the mid-height of pillar) and peak major principal stress at the core of pillars with different W/H ratios. It can be observed that the peak major principal stress at the core is always higher than the overall pillar strength because the confinement and thereby strength at the centre of pillars is higher than that at the wall of the pillar. As the width to height ratio of pillars increases, the difference between the pillar strength and peak stress at the core becomes more dramatic. It is the result of higher induced confinements inside the wide pillars (Fig. 5.4a) which involves higher potential for strain-hardening behavior at the core (Fig. 5.6b).

In order to better explore the trend of pillar strength curves, it is useful to look at empirical and numerical results in general. Fig. 5.2 shows the empirical pillar strength curves and Fig. 5.12 shows the pillar strength curves obtained from numerical analyses carried out by various researchers. Martin and Maybee (2000) adopted the finite element method and carried out elastic analysis using the brittle parameters to predict the strength of pillars. Mortazavi et al (2009) used the finite difference method and a strain-softening model to capture the behavior of hard rock pillars. Elmo and Stead (2010) used a hybrid finite element/discrete element method to explicitly model the fracture network inside the pillars. The results of this study using the finite difference method and the CWFS model for the Elliot Lake mine is also shown in Fig. 5.12. The strength curve proposed by Lunder and Pakalnis (1997) is also shown in Fig. 5.12 to represent empirical pillar strength formulas.

It can be seen that while empirical pillar strength curves are linear or concave downward (Fig. 5.2), all pillar strength curves from numerical analysis show an upward trend (Fig. 5.12). As pointed out by Martin and Maybee (2000) and Kaiser et al (2011), a vast majority of failed pillars in the empirical dataset have a W/H ratio of less than 2 and there are no failed cases beyond W/H ratio of 2.3. Considering the fact that empirical pillar strength formulas are entirely based on the pillar dataset, the strength values and the concave downward trend of empirical formulas beyond W/H of 2.5 may not be reliable. On the other hand, numerical methods are governed by physical laws and relationships such as

equilibrium and compatibility and incorporate material models which are supported by experimental results. Hence, it seems that the upward trend obtained from numerical models may be more reliable. It is also in keeping with the notion that strength of wide pillars is underestimated by the empirical pillar strength formulas (Kaiser et al, 2011).
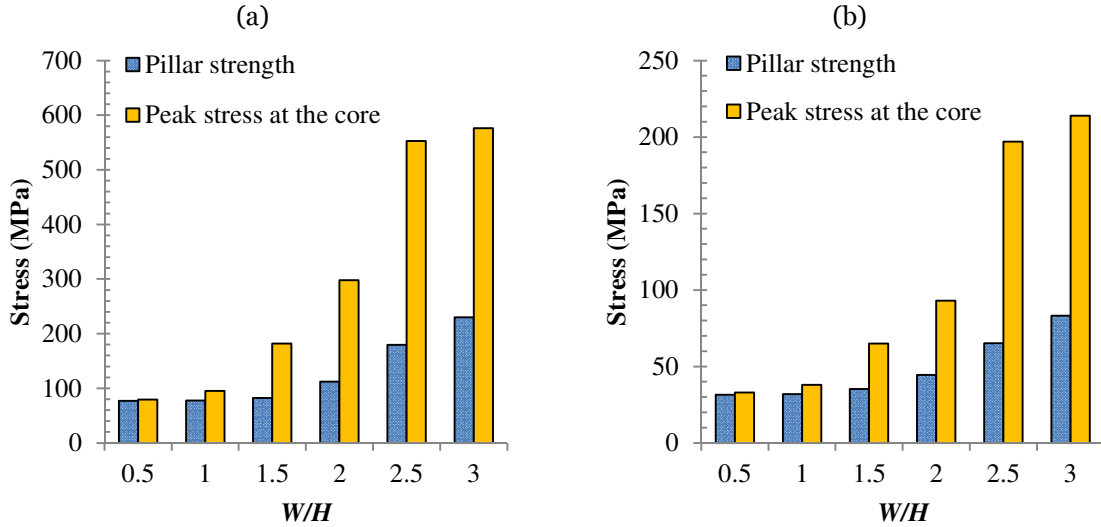
Fig. 5.11 Overall pillar strength and peak major principal stress at the core of pillars at (a) the Elliot Lake mine and (b) the Selebi-Phikwe mine
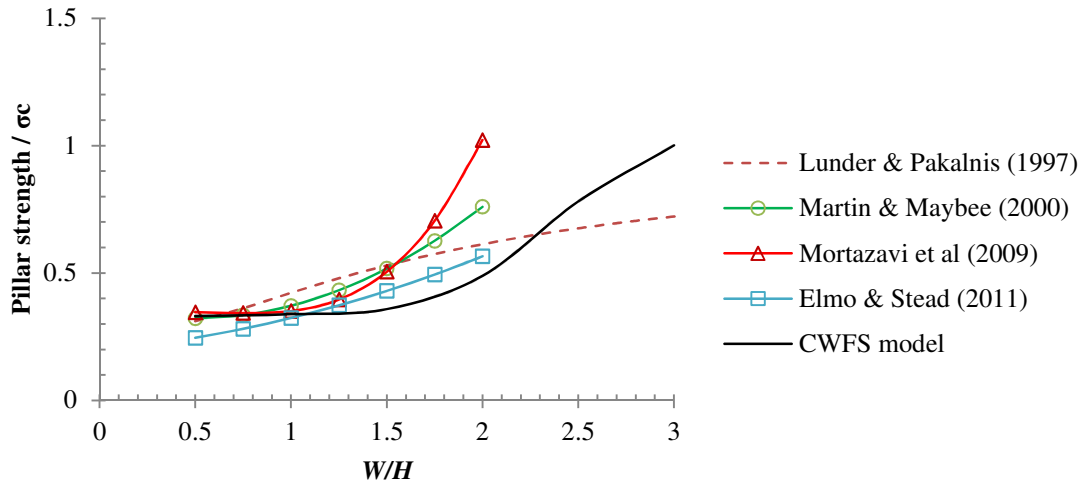
Fig. 5.12 Pillar strength curves from numerical analysis (solid lines) and empirical formula (dashed line)

The numerical simulations in the case studies were carried out using only CWFS model and under plane strain condition. However, the geometry and loading condition of pillars used in mining operations are more complex. It is also instructive to compare the results of the CWFS models with other well-established constitutive models. In order to examine the effect of complex geometries and different constitutive models, a three-dimensional model

of a typical block caving pillar at a depth of 1 km was analyzed. As shown in Fig. 5.13a, the pillar is 10 m wide, 3.8 m high and 32 m long. The access drifts are 4.3 m wide and have horseshoe cross sections.

The CWFS model and Mohr-Coulomb model with perfectly-plastic and strain-softening behavior were used for the analysis. For this example, material parameters representative of rock mass at the Elliot Lake mine were determined for each constitutive model (Table 5.3). The parameters for the CWFS model are the same as those used in the case studies (Table 5.2). Parameters for the perfectly-plastic Mohr-Coulomb model were obtained using the guidelines by Hoek et al (2002) as implemented in the RocLab software (RocScience Inc., 2007). For the strain-softening model, similar guidelines were used where the peak strength parameters were obtained using the initial GSI value of 80 and residual strength parameters were obtained using a residual GSI value of 27 as suggested by Cai et al (2007).

Table 5.3 Parameters and results of different constitutive models used in the three-dimensional analysis

Model	c_{ini} (MPa)	c_{ult} (MPa)	φ_{ini} (deg)	φ_{ult} (deg)	Pillar strength (MPa)
CWFS	38.0	3.8	0	35	181
Perfectly-plastic	11.4	11.4	56	56	N/A
Strain-softening	11.4	3.5	56	42	N/A
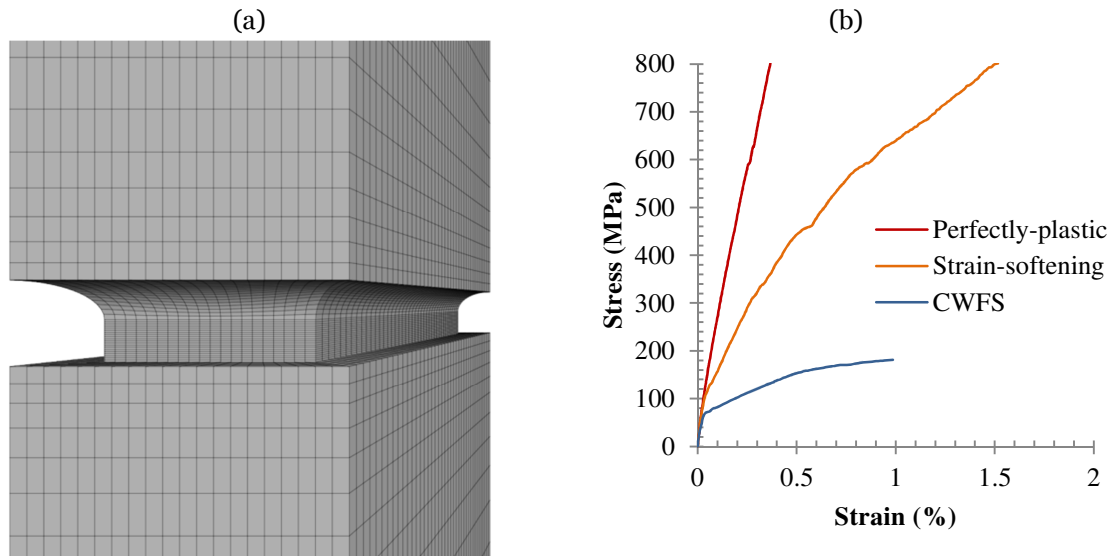
Fig. 5.13 Three-dimensional analysis of a typical block caving pillar (a) FLAC3D mesh and (b) stress-strain curves using different constitutive models

Stress-strain curves for the three-dimensional pillar using different constitutive models are shown in Fig. 5.13b. The CWFS model gives a pillar strength value of 181 MPa which is in reasonable agreement with the empirical formula and numerical results plane strain analysis shown in Fig. 5.10a. The Mohr-Coulomb perfectly-plastic and strain-softening models, on the other hand, show no finite strength even after 800 MPa. This is clearly unrealistic and inconsistent with empirical observations shown in Fig. 5.10a. Hence, well-established models such as Mohr-Coulomb perfectly-plastic and strain-softening models

may grossly overestimate the strength of wide pillars. This highlights the importance of using a representative constitutive model in numerical analysis of hard rock pillars.

5.8. Conclusions

The behavior of hard rock pillars was addressed using empirical, theoretical, and numerical analysis. The effect of size and shape on the strength of pillars was quantified using empirical evidence and numerical simulations. Using a failure criterion and considering the effect of size and shape, a semi-analytical strength formula for hard rock pillars was derived.

In order to further explore the behavior of hard rock pillars, numerical simulations using the CWFS model were carried out. Equations were proposed to describe the gradual degradation of cohesion and mobilization of friction with increasing damage. Two case studies namely the Elliot Lake mine and Selebi-Phikwe mine were used to verify the merits of the proposed modelling approach for hard rock pillars.

In both cases, the numerical models were able to successfully separate the unstable/failed pillars from the stable pillars. The numerical models also captured the mechanism of progressive failure observed in hard rock pillars. The overall pillar stress-strain curves indicated that while pillars with W/H<2 exhibit strain-softening behavior at relatively low strains, those with W/H>2 show strain-hardening behavior and continue to carry higher loads up to much higher strain levels. Monitoring the stress path at the core of pillars showed that for pillars with W/H≤1 the peak major principal stress at the core drops after reaching the initial cohesive yield envelope while it continues to increase and follow the ultimate frictional envelope for pillars with W/H≥2. A CWFS-based pillar strength formula was presented to summarize the results of numerical simulations.

Finally, a typical block caving pillar was analyzed using the well-established Mohr-Coulomb perfectly-plastic and strain-softening models. It was shown that such models can drastically overestimate the strength of wide pillars. On the other hand, comparing the results of numerical analysis and empirical pillar strength formulas suggest that empirical formulas may systematically underestimate the strength of wide pillars.

References

ASTM (2004). Designation: D 7012 – 04: Standard Test Method for Compressive Strength and Elastic Moduli of Intact Rock Core Specimens under Varying States of Stress and Temperatures, American Society for Testing and Materials, Philadelphia, PA, USA.

Bieniawski, Z. T. (1968). The effect of specimen size on compressive strength of coal. International Journal of Rock Mechanics and Mining Sciences, 5, 325-335.

Bieniawski, Z. T. (1992). A method revisited: coal pillar strength formula based on field investigations, In: proceedings of the workshop on the coal pillar mechanics and design, Bureau of Mines; p 158-165.

Cai, M., Kaiser, P.K., Tasakab, Y., Minamic, M. (2007). Determination of residual strength parameters of jointed rock masses using the GSI system. International Journal of Rock Mechanics and Mining Sciences, 44, 247–265.

Coates DF, Gyenge M. (1981). Incremental design in rock mechanics. Monograph, vol. 880. Ottawa: Canadian Government Publishing Centre.

Elmo, D., Stead, D. (2010). An integrated numerical modelling discrete fracture network approach applied to the characterization of rock mass strength of naturally fractured pillars. Rock Mechanics and Rock Engineering, 43, 3–19.

Hajiabdolmajid, V., Kaiser, P.K., Martin, C. D. (2002) Modelling brittle failure of rock. International Journal of Rock Mechanics and Mining Sciences, 39, 731-741.

Hawkes, I., Mellor, M. (1970) Uniaxial testing in rock mechanics laboratories. Engineering Geology, 4(3), 177–285.

Hedley, D. G. F., Grant, F. (1972). Stope-and-pillar design for the Elliot Lake Uranium Mines. Bulletin of Canadian Institute of Mining and Metallurgy, 65, 37-44.

Hoek, E., Brown, E. T. (1997). Practical estimates of rock mass strength. International Journal of Rock Mechanics and Mining Sciences, 34, 1165-1186.

Hoek, E., Carranza-Torres, C.T., Corkum, B. (2002) Hoek-Brown failure criterion-2002 edition. In: Proceedings of the fifth North American rock mechanics symposium, Toronto, Canada, vol. 1, p. 267–73.

Itasca Inc. (2009). FLAC3D, Fast Lagrangian Analysis of Continua in 3 Dimensions. Version 4.00. Minneapolis.

Kaiser, P. K., Kim, B., Bewick, R. P., Valley, B. (2011). Rock mass strength at depth and implications for pillar design. Mining Technology, 120 (3), 170-179.

Krauland, N., Soder, P. E. (1987). Determining pillar strength from pillar failure observations. Engineering and Mining Journal, 8:34-40.

Lunder, P. J., Pakalnis, R. (1997). Determination of the strength of hard- rock mine pillars. Bulletin of Canadian Institute of Mining and Metallurgy, 90, 51-55.

Martin, C. D. (1997). Seventeenth Canadian Geotechnical Colloquium: the effect of cohesion loss and stress path on brittle rock strength. Canadian Geotechnical Journal. 34, 698-725.

Martin, C. D., Chandler, N. A. (1994). The progressive fracture of Lac du Bonnet granite. International Journal of Rock Mechanics and Mining Sciences and Geomechanics Abstracts, 31, 643-659.

Martin, C. D., Lu, Y., Lan, H. (2012). Scale effects in a synthetic rock mass. In: Harmonising Rock Engineering and the Environment, p. 257-258, Taylor & Francis Group, London.

Martin, C.D., Maybee, W.G. (2000). The strength of hard-rock pillars, International Journal of Rock Mechanics and Mining Sciences, 37, 1239-1246

Mortazavi, A., Hassani, F.P., Shabani, M. (2009). A numerical investigation of rock pillar failure mechanism in underground openings. Computers and Geotechnics, 36, 691–697.

Nareetsile, S. M. (1998) The modified creeping cone mining method, M.Sc. thesis, Department of Civil & Environmental Engineering, Univ. of Alberta, Canada.

Potvin, Y., Hudyma, M. R., Miller, H. D. S. (1989). Design guidelines for open stope support. Bulletin of Canadian Institute of Mining and Metallurgy, 82:53-62.

Pratt, H. R., Black A. D., Brown W. S., Brace W. F. (1972). The effect of specimen size on the mechanical properties of unjointed diorite. International Journal of Rock Mechanics and Mining Sciences, 9, 513-529.

Pritchard, C. J., Hedley, D. G. F. (1993). Progressive pillar failure and rock bursting at Denison Mine. In: Proc. 3rd International Symposium on Rock bursts and Seismicity in Mines, Kingston, ed. R. P. Young, pp. 111–116, Rotterdam. A.A. Balkema.

RocScience Inc. (2007). RocLab Version 1.032, Rock mass strength analysis using the Hoek-Brown failure criterion. Toronto, Canada.

Salamon, M. D. G., Munro, A. H. (1967). A study of the strength of coal pillars. Journal of the South African Institute of Mining and Metallurgy, 68, 55-67.

Sjoberg, J. (1992). Failure modes and pillar behaviour in the Zinkgruvan mine. In: Tillerson JA, Wawersik WR, editors. Proceedings of 33rd U.S. Rock Mechanics Symposium, pp. 491-500, Rotterdam: A.A. Balkema.

Swan, G. (1985). Strength distribution and potential for multiple pillar collapse. Divisional Report MRL 85-127 (TR), CANMET, Energy Mines and Resources, Canada.

von Kimmelmann, M. R., Hyde, B., Madgwick, R. J. (1984). The use of computer applications at BCL Limited in planning pillar extraction and design of mining layouts. In: Brown ET, Hudson JA, editors. Proceedings of ISRM Symposium: Design and Performance of Underground Excavations, pp. 53-63, London: British Geotechnical Society.

Wagner, H. (1974). Determination of the complete load-deformation characteristics of coal pillars. In Proceedings of 3rd ISRM Conference, pp. 1076-1081, Denver. Colorado.

Chapter 6

Summary and conclusions

This thesis was focused on the behavior of good quality to massive rock masses with geological strength index, GSI greater than 60. Different approaches have been proposed for modelling the behavior of excavations in such rock masses. In this thesis, the results of laboratory tests and in situ measurements and observations were used to examine applicability of the current models for each class of rock masses. Limitations and shortcomings of the existing models were discussed and improvements modelling approaches were proposed. The following is a summary of conclusions drawn from this thesis.

6.1. Christensen and Hoek-Brown criteria for intact rock

The first part of this study was dedicated to comparing the well-established Hoek-Brown criterion and the recently proposed Christensen criterion when applied to failure of intact rock. The Christensen criterion was proposed as a comprehensive model for all materials and has attractive characteristics including simple equations with uniaxial compressive and tensile strength as parameters and inclusion of the intermediate principal stress in the failure criterion. The components of the Christensen criterion including the main parabolic envelope, tension cut-off and brittle-to-ductile were explained in detail. Explicit equations were derived for application of the Christensen criterion to failure of rocks under biaxial compression, triaxial compression, triaxial extension, and polyaxial compression.

The results of laboratory tests on a synthetic rock, chert dyke, Carrara marble and Westerly granite were used for quantitative comparison of the Hoek-Brown and Christensen criteria. It was shown that application of the Christensen criterion results in 65% higher prediction errors compared to the Hoek-Brown criterion. Mathematical evaluation of the Christensen criterion revealed that there are theoretical limits for the slopes of the failure envelopes. Regardless of the parameters, the slope of the Christensen envelopes cannot exceed 2.5 in triaxial extension and 4.0 in triaxial compression. This is the main characteristics of the Christensen criterion which limits its application for hard rocks which typically show much steeper experimental envelopes.

While the Christensen criterion included the intermediate principal stress in the equations, it failed to adequately capture the effect of intermediate principal stress on strength of intact

97

rock. In fact, the Hoek-Brown criterion which ignores the effect of intermediate principal stress provided a better fit to the results of polyaxial compression tests on Westerly granite than the Christensen criterion. This interesting phenomenon is due to the fact that the π-plane representation of the Christensen criterion is circular while the Hoek-Brown criterion gives an asymmetrical hexagonal shape which more closely follows the trend of experimental results.

The brittle-to-ductile transition limit predicted by the Christensen criterion was also shown to be inconsistent with the observed behavior of intact rocks. While the transition in the Christensen criterion is a function of volumetric stress, laboratory observations show that transition from brittle to ductile behavior depends on the ratio of major to minor principal stress. As a result, the Christensen criterion predicts ductile failure for intact rocks under uniaxial and triaxial compression while laboratory observations show brittle failure under low to moderate confinements and ductile failure under high confining stresses.

6.2. Shaft displacements in a rock mass with GSI≈60

Measured displacements around a deep shaft excavated in an average quality rock mass with GSI of 62 were used to examine the accuracy of existing modelling approaches. According to empirical guidelines, strain softening models was used for the back analysis.

Three-dimensional numerical models could explicitly replicate the effect of excavation sequence of extensometer measurements. Using the estimated parameters from empirical guidelines provided a reasonable fit to the measurements of two extensometers. The measurements of the third extensometer could only be reproduced using weaker material parameters which caused overestimation of displacements for other extensometers. Nonetheless, the possible range of input parameters were obtained for analyzing the behavior of future excavations using strain softening model.

Two-dimensional numerical models were also used along with longitudinal displacement profile (LDP) for taking into account the three-dimensional effects around an advancing excavation face. Interestingly, two-dimensional models could provide a better overall match to the results of all extensometers. Upon further investigation, it was shown that apparently better overall fits from the two-dimensional model is due to the fact that three-dimensional effects were compromised in this approach. Comparing the results of two- and three-dimensional models showed that convergence around the excavation perimeter under anisotropic in situ stress field is not constant and LDPs fail to adequately capture the variation of convergence especially near the excavation face.

6.3. Progressive failure of brittle rocks with GSI≈100

In order to explore the process of progressive failure in hard brittle rocks, the results of uniaxial and triaxial damage-controlled tests on samples of Lac du Bonnet granite and

Indiana limestone were analyzed. Each loading-unloading cycle in the tests causes an increment of damage within the sample.

Analysis the stress-strain response of the samples during each cycle showed that increasing damage leads to degradation of cohesion and mobilization of friction angle. Comparison of the results at different confining stresses showed that while cohesion degradation process is essentially independent of confinement, mobilization of friction angle is strongly affected by the confinement level. At low confinement, friction angle can reach higher values while elevated confinement supresses the maximum mobilized friction angle.

Theoretical cohesion-weakening friction strengthening (CWFS) models were proposed to capture the process of cohesion degradation and friction mobilization at different confinement level. Application of the proposed model to the laboratory test results showed a close agreement between the measured and predicted stress-strain curves. The model was then implemented in FLAc3D to predict the stability of four tunnels excavated in a massive granite rock mass at the Underground Research Laboratory (URL) in Manitoba. The proposed model eliminated the fundamentally problematic characteristics of the current CWFS model and gave a reasonable match to the observed zone of brittle failure around the URL excavations.

One of the key characteristics of the proposed CWFS model is capturing the transition from strain-softening to strain-hardening behavior with increasing confinement. Analyzing the stress-path at different points around the excavations showed that moving from the excavation boundary deeper inside the zone of in situ brittle failure restrains the strain-softening behavior due to increased induced confinement.

In order to evaluate the effect of model parameters on the predicted behavior, a series of parametric studies were carried out. It was shown that increasing the initial and residual values of cohesion and friction angle reduces the depth and angular extent of zone of failure. Based on experience gained from application of the proposed CWFS model to several excavations, general guidelines were proposed for estimation of the model parameters for preliminary analysis.

6.4. Modelling the progressive failure of rock pillars with GSI≈80

Hard rock pillars usually found in good quality rock masses provide an opportunity to examine different modelling approaches. Empirical pillar strength formulas were examined to determine the effect of pillar size and shape on pillar strength. It was shown that the in situ strength of a hard rock pillar with width-to-height ratio (W/H) of 0.5 excavated in a good quality rock mass (GSI≈80) is about 1/3 of the uniaxial compressive strength of intact rock. The effect of pillar shape on induced confinement within the pillar was quantified using numerical analysis and subsequently used in a failure criterion to derive a semi-analytical pillar strength formula.

The proposed CWFS model implemented in FLAC3D was used to predict the strength of pillars in the Elliot Lake and Selebi-Phikwe mines. Model parameters were estimated from the proposed general guidelines. The results of numerical analysis in both case studies successfully separated stable pillars from unstable/failed pillars. Furthermore, the observed in situ mechanism of pillar failure starting from minor spalling at 70% peak strength to formation of hour glass shaped pillar and final shear failure was also captured in the models.

Overall pillar stress-strain curves showed that pillars with W/H<2 reach peak strength at relatively low strains followed by strain softening behavior. Wider pillars, on the other hand, can continue to sustain increased stress levels at higher strains. Investigation of stress-path at the core of pillars showed that for a pillar with W/H=1 stress drops after reaching the initial cohesive strength envelope while it continues to increase and follow the ultimate frictional strength envelope for a pillar with W/H=2. The results of the proposed CWFS model for hard rock pillars were given in a simple pillars strength formula for practical applications.

For comparison purposes, a deep block caving pillar was analyzed using the proposed CWFS model and the currently used perfectly-plastic and strain-softening models. It was shown that the currently used models can significantly overestimate the strength of deep pillars. On the other hand, comparing the results of empirical pillar strength formulas and different numerical models indicate that the strength of wide pillars can be systematically underestimated by the empirical formulas developed for narrower pillars.

6.5. Future research

In this thesis, the results of laboratory and in situ measurements and observations in good to massive quality rock masses were used to develop improved modelling methods. Currently, damage-controlled test appears to be the only test to properly capture the effect of damage evolution on cohesive and frictional components of strength. In its current form, the test is technically difficult, time consuming, and costly and has been done on a handful of rocks in the world. Enhancements to the damage-controlled test without compromising the essential aspects of the test can be of great interest. As simpler versions of the test develop, more and more rocks can be tested and the findings presented in this thesis and elsewhere can be re-evaluated for other rock types.

The behavior of a deep shaft, two underground mines, and four tunnels excavated in rock masses with GSI ≥60 was discussed in this work. In order to find the merits and possible limitations of the discussed modelling approaches, it is important to apply the models to other in situ problems with different geometries, depths, and rock mass qualities. While some general equations and guidelines were proposed for estimating the model parameters, further studies are required to fine tune such estimations. The more case studies used to validate a model and its parameters, the more confidence can be gained in its application to future projects.

Bibliography

Al-Ajmi, A. M., Zimmerman, R. W. (2005), Relation between the Mogi and the Coulomb failure criteria, Int. J. Rock. Mech. Min. Sci., 42, 431–439.

ASTM (2004). Designation: D 7012 – 04: Standard Test Method for Compressive Strength and Elastic Moduli of Intact Rock Core Specimens under Varying States of Stress and Temperatures, American Society for Testing and Materials, Philadelphia, PA, USA.

Barton, N., Choubey, V. (1977). The shear strength of rock joints in theory and practice. Rock Mechanics 10:1-54. Vienna: Springer.

Benz, T., Schwab, R. (2008), A quantitative comparison of six rock failure criteria, Int. J. Rock. Mech. Min. Sci., 45, 1176–1186.

Benz, T., Schwab, R., Kauther, R. A., Vermeer, P. A. A. (2008), Hoek–Brown criterion with intrinsic material strength factorization, Int. J. Rock. Mech. Min. Sci., 45(2), 210–22.

Bieniawski ZT (1967) Mechanism of brittle fracture of rock, parts I, II and III. Int J Rock Mech Min Sci Geomech Abstr. 4(4):395–430.

Bieniawski, Z. T. (1968). The effect of specimen size on compressive strength of coal. International Journal of Rock Mechanics and Mining Sciences, 5, 325-335.

Bieniawski, Z. T. (1992). A method revisited: coal pillar strength formula based on field investigations, In: proceedings of the workshop on the coal pillar mechanics and design, Bureau of Mines; p 158-165.

Brown E. T. (1981). Rock Characterization Testing and Monitoring, ISRM Suggested Methods. pp. 107-127. Pergamon Press, Oxford.

Cai, M., Kaiser, P.K., Tasaka, Y., Minami, M., (2007). Determination of residual strength parameters of jointed rock masses using the GSI system. Int. J. Rock. Mech. Min. Sci. 44, 247-265.

Carranza-Torres. C., Fairhurst, C., (2000). Application of the convergence–confinement method of tunnel design to rock masses that satisfy the Hoek–Brown failure criterion. Tunn. Undergr. Space. Technol. 15, 187–213.

Coates DF, Gyenge M. (1981). Incremental design in rock mechanics. Monograph, vol. 880. Ottawa: Canadian Government Publishing Centre.

Christensen, R. M. (1997), Yield functions/failure criteria for isotropic materials, In: Proceedings of Mathematical, Physical and Engineering Sciences, Vol. 453, London: The Royal Society, p. 1473-1491.

Christensen, R. M. (2000), Yield functions, damage states and intrinsic strength, Math. Mech. Solids, 5,285-300.

Christensen, R. M. (2004), A two property yield, failure (fracture) criterion for homogeneous, isotropic materials, J. Eng. Mater. Tech., 126, 45-52.

Christensen, R. M. (2005), Exploration of ductile, brittle failure characteristics through a two parameter yield/failure criterion, Mater. Sci. Eng. A, 394, 417-424.

Christensen, R. M. (2006a), Yield Functions and Plastic Potentials for BCC Metals and Possibly Other Materials, J. Mech. Mater. Structs.,1,183-200.

Christensen, R. M. (2006b), A comparative evaluation of three isotropic, two property failure theories, J. Appl. Mech., 73, 852-859.

Christensen, R. M. (2007), A comprehensive theory of yielding and failure for isotropic materials, J. Eng. Mater. Tech., 129, 173-181.

Cividini, A., Jurina, L., Gioda, G., (1981). Some aspects of characterization problems in geomechanics. Int. J. Rock. Mech. Min. Sci. 18, 487–503.

Colmenares, L. B., Zoback, M. D. (2002), A statistical evaluation of intact rock failure criteria constrained by polyaxial test data for five different rocks, Int. J. Rock. Mech. Min. Sci., 39, 695–729.

Diederichs, M.S. (2007). The 2003 Canadian Geotechnical Colloquium: Mechanistic interpretation and practical application of damage and spalling prediction criteria for deep tunnelling. Can Geotech J, 44:1082-1116.

Drucker, D., Prager, W. (1952), Soil mechanics and plastic analysis or limit design. Quart Appl Math, 10:157–165.

Edelbro C, Sjoberg C, Malmgren L, Dahner-Lindqvist C (2012) Prediction and follow-up of failure and fallouts in footwall drifts in the Kiirunavaara mine, Can Geotech J, 49:546-559.

Elmo, D., Stead, D. (2010). An integrated numerical modelling discrete fracture network approach applied to the characterization of rock mass strength of naturally fractured pillars. Rock Mechanics and Rock Engineering, 43, 3–19.

Gioda, G., Maier, G., (1980). Direct search solution of an inverse problem in elastoplasticity: identification of cohesion, friction angle and in situ stress by pressure tunnel tests. Int. J. Numer. Meth. Eng. 15, 1823–1848.

Haimson, B., Chang, C. (2000), A new true triaxial cell for testing mechanical properties of rock, and its use to determine rock strength and deformability of Westerly granite, Int. J. Rock. Mech. Min. Sci., 37, 285–296.

Hajiabdolmajid, V., Kaiser, P.K., Martin, C. D. (2002) Modelling brittle failure of rock. International Journal of Rock Mechanics and Mining Sciences, 39, 731-741.

Hammah, R. E. Carvalho, J. L. (2011), An introduction to the Christensen criterion – An answer to true, representative modelling of intact rock yielding/failure?, In: CD-Rom Proceedings of the International Symposium on Rock Slope Stability in Open Pit Mining and Civil Engineering, Vancouver, BC.

Hawkes, I., Mellor, M. (1970) Uniaxial testing in rock mechanics laboratories. Engineering Geology, 4(3), 177–285.

Hedley, D. G. F., Grant, F. (1972). Stope-and-pillar design for the Elliot Lake Uranium Mines. Bulletin of Canadian Institute of Mining and Metallurgy, 65, 37-44.

Hoek, E. (1965), Rock fracture under static stress conditions, Ph.D. thesis, The Faculty of Engineering, Univ. of Cape Town, South Africa.

Hoek, E. Brown, E. T. (1980), Empirical strength criterion for rock masses, J. Geotech. Eng. Div., ASCE 106(GT9), 1013-1035.

Hoek, E. (1983), Strength of jointed rock masses, 23rd Rankine Lecture, Géotech, 33(3), 187-223.

Hoek, E. (1990), Estimating Mohr-Coulomb friction and cohesion values from the Hoek-Brown failure criterion, Int. J. Rock Mech. Min. Sci. Geomech. Abst, 12(3), 227-229.

Hoek, E. Wood, D. Shah, S. (1992), A modified Hoek-Brown criterion for jointed rock masses, In: Proc. Rock Characterization Symp., Int. Soc. Rock Mech.: Eurock '92, J. Hudson ed, 209-213, London: British Geotechnical Society.

Hoek, E. Brown, E. T. (1997), Practical estimates of rock mass strength, Int. J. Rock. Mech. Min. Sci., 34, 1165-1186.

Hoek, E. Carranza-Torres, C. Corkum, B (2002), Hoek-Brown failure criterion – 2002 Edition, In: Proceedings of NARMS-TAC Conference, Toronto, ON, p. 267-273.

Hoek, E., Carranza-Torres, C., Diederichs, M.S., Corkum, B,. (2008). Integration of geotechnical and structural design in tunnelling – 2008 Kersten Lecture. In: Proceedings University of Minnesota 56th Annual Geotechnical Engineering Conference. Minneapolis, pp 1-53.

Hoek, E., Diederichs, M.S., (2006). Empirical estimation of rock mass modulus. Int. J. Rock. Mech. Min. Sci. 43, 203–215.

Howarth, D. F. Rowlands, J. C. (1987), Quantitative assessment of rock texture and correlation with drillability and strength properties, Rock. Mech. Rock. Eng., 20, 57-85.

Itasca Inc,. (2009). FLAC- Fast Lagrangian Analysis of Continua, Version 3.3, Minneapolis, United States.

Jaeger, J. C. Cook, N. G. W. (1979). Fundamentals of rock mechanics. 3rd edition, London: Chapman and Hall.

Johnson, B. Friedman, M. Hopkins, T. W. (1987), Strength and microfracturing of Westerly granite extended wet and dry at temperatures to 800°C and pressures to 200 MPa, In: Proceedings of the 28th U.S. Symposium on Rock Mechanics (USRMS), Tucson, AZ, p. 399-412.

Kaiser, P. K., Kim, B., Bewick, R. P., Valley, B. (2011). Rock mass strength at depth and implications for pillar design. Mining Technology, 120 (3), 170-179.

Kim, M. K., Lade, P. V. (1984), Modelling Rock Strength in Three Dimensions, Int. J. Rock Mech. Min. Sci., 21, 21-33.

Krauland, N., Soder, P. E. (1987). Determining pillar strength from pillar failure observations. Engineering and Mining Journal, 8:34-40.

Krech, W. W. Henderson, F. A. and Hjelmstad, K. E. (1974), A standard rock suite for rapid excavation research, Bureau of Mines Report of Investigations No. 7865, 29 p.

Lajtai E. Z. Gadi A. M. (1989). Friction on a granite to granite interface. Rock Mech. Rock Eng, 22, 25-49.

Lunder, P. J., Pakalnis, R. (1997). Determination of the strength of hard- rock mine pillars. Bulletin of Canadian Institute of Mining and Metallurgy, 90, 51-55.

Martin CD (1993) The strength of massive Lac du Bonnet granite around underground opening. Ph.D. thesis, Dept of Civil & Geological Engineering, University of Manitoba, Winnipeg.

Martin, C. D. (1997). Seventeenth Canadian Geotechnical Colloquium: the effect of cohesion loss and stress path on brittle rock strength. Canadian Geotechnical Journal. 34, 698-725.

Martin CD, Chandler N. (1994) The progressive fracture of Lac du Bonnet granite. Int J Rock Mech Min Sci, 31(6):643–59.

Martin, C. D., Lu, Y., Lan, H. (2012). Scale effects in a synthetic rock mass. In: Harmonising Rock Engineering and the Environment, p. 257-258, Taylor & Francis Group, London.

Martin, C.D., Maybee, W.G. (2000). The strength of hard-rock pillars, International Journal of Rock Mechanics and Mining Sciences, 37, 1239-1246.

Martin CD, Stimpson B (1994) The effect of sample disturbance on laboratory properties of Lac du Bonnet granite. Can Geotech J, 31:692–702.

Miranda, T., Dias, D., Eclaircy-Caudron, S., Gomes Correia, A., Costa, L., (2011). Back analysis of geomechanical parameters by optimisation of a 3D model of an underground structure. Tunn. Undergr. Space. Technol. 26, 659–673.

Mogi, K. (1971), Fracture and flow of rocks under high triaxial compression, J. Geophys. Res., 76, 1255–1269.

Mortazavi, A., Hassani, F.P., Shabani, M. (2009). A numerical investigation of rock pillar failure mechanism in underground openings. Computers and Geotechnics, 36, 691–697.

Nareetsile, S. M. (1998) The modified creeping cone mining method, M.Sc. thesis, Department of Civil & Environmental Engineering, Univ. of Alberta, Canada.

Nguyen, Si-H., Chemenda, A. I., Ambre, J. (2011), Influence of the loading conditions on the mechanical response of granular materials as constrained from experimental tests on synthetic rock analogue material, Int. J. Rock Mech. Min. Sci., 48, 103-115.

Pan, X. D., Hudson, J. A. (1988), A simplified three dimensional Hoek–Brown yield criterion. In: Romana M (ed) Rock mechanics and power plants. Rotterdam: Balkema, , pp 95–103.

Panet, M., (1995). Le calcul des tunnels par la me´thode convergenceconfinement. Presses de l'Ecole Nationale des Ponts et Chausse´es, Paris, France, p. 177.

Potvin, Y., Hudyma, M. R., Miller, H. D. S. (1989). Design guidelines for open stope support. Bulletin of Canadian Institute of Mining and Metallurgy, 82:53-62.

Pratt, H. R., Black A. D., Brown W. S., Brace W. F. (1972). The effect of specimen size on the mechanical properties of unjointed diorite. International Journal of Rock Mechanics and Mining Sciences, 9, 513-529.

Priest, S. D. (2005), Determination of shear strength and three-dimensional yield strength for the Hoek–Brown yield criterion. Rock. Mech. Rock. Eng. 38(4), 299–327.

Pritchard, C. J., Hedley, D. G. F. (1993). Progressive pillar failure and rock bursting at Denison Mine. In: Proc. 3rd International Symposium on Rock bursts and Seismicity in Mines, Kingston, ed. R. P. Young, pp. 111–116, Rotterdam. A.A. Balkema.

Rafiei, H. (2011), New empirical polyaxial criterion for rock strength, Int. J. Rock. Mech. Min. Sci., 48, 922–931.

Rafiei Renani, H., Martin, CD., Modelling the progressive failure of hard rock pillars, Rock Mechanics and Rock Engineering, Under review.

Ramsey, J. M. Chester, F. M. (2004), Hybrid fracture and the transition from extension fracture to shear fracture, Nature, 428, 63-66.

Read, RS, Chandler, NA, Dzik, EJ. (1998). In situ strength criteria for tunnel design in highly-stressed rock masses. International Journal of Rock Mechanics and Mining, 35(3), 261-278.

Read, RS, Chandler, NA. (2002) An approach to excavation design for a nuclear fuel waste repository -the thermal-mechanical stability study final report, Ontario Power Generation, Nuclear Waste Management Division Report No: 06819-REP-01200-10086-R00.

RocScience Inc. (2007). RocLab Version 1.032, Rock mass strength analysis using the Hoek-Brown failure criterion. Toronto, Canada.

Rocscience Inc., (2010). 3D tunnel simulation using the core replacement technique. Phase2 Version7.0 Tutorial Manual, Toronto, Canada.

Sakurai, S., Takeuchi, K., (1983). Back analysis of measured displacements of tunnels. Rock. Mech. Rock. Eng. 16, 173-180.

Salamon, M. D. G., Munro, A. H. (1967). A study of the strength of coal pillars. Journal of the South African Institute of Mining and Metallurgy, 68, 55-67.

Schmidtke R. H. Lajtai E. (1985) The long-term strength of Lac du Bonnet granite. Int. J. Rock Mech. Min. Sci. & Geomech. Abstr. 22, 461-465.

Sjoberg, J. (1992). Failure modes and pillar behaviour in the Zinkgruvan mine. In: Tillerson JA, Wawersik WR, editors. Proceedings of 33rd U.S. Rock Mechanics Symposium, pp. 491-500, Rotterdam: A.A. Balkema.

Swan, G. (1985). Strength distribution and potential for multiple pillar collapse. Divisional Report MRL 85-127 (TR), CANMET, Energy Mines and Resources, Canada.

Unlu, T., Gercek, H., (2003). Effect of Poisson's ratio on the normalized radial displacements occurring around the face of a circular tunnel. Tunn. Undergr. Space. Technol. 18, 547–553.

Vardakos, S.S., Gutierrez, M.S., Barton, N.R., (2007). Back-analysis of Shimizu Tunnel No. 3 by distinct element modeling. Tunn. Undergr. Space. Technol. 22, 401–413.

Vlachopoulos, N., Diederichs, M.S., 2009. Improved longitudinal displacement profiles for convergence-confinement analysis of deep tunnels. Rock. Mech. Rock. Eng. 42, 131-146.

von Kimmelmann, M. R., Hyde, B., Madgwick, R. J. (1984). The use of computer applications at BCL Limited in planning pillar extraction and design of mining layouts. In: Brown ET, Hudson JA, editors. Proceedings of ISRM Symposium: Design and Performance of Underground Excavations, pp. 53-63, London: British Geotechnical Society.

Wagner, H. (1974). Determination of the complete load-deformation characteristics of coal pillars. In Proceedings of 3rd ISRM Conference, pp. 1076-1081, Denver. Colorado.

Walton, G., Diederichs, M. (2015) Dilation and post-peak behaviour inputs for practical engineering analysis. Geotech Geol Eng, 33: 15–34.

Walton, G., Diederichs, M., Punkkinen, A. (2015) The influence of constitutive model selection on predicted stresses and yield in deep mine pillars – A case study at the Creighton mine, Sudbury, Canada. Geomech Tunnelling, 8: 441–449.

Yazdani, M., Sharifzadeh, M., Kamrani, K., Ghorbani, M., (2012). Displacement-based numerical back analysis for estimation of rock mass parameters in Siah Bisheh powerhouse cavern using continuum and discontinuum approach. Tunn. Undergr. Space. Technol. 28, 41–48.

Zhang, L., Zhu, H. (2007), Three-dimensional Hoek–Brown strength criterion for rocks, J. Geotech. Geoenvir. Eng. ASCE. 133(9), 1128–1135.

Zhao, XG, Cai, M. (2010). Influence of plastic shear strain and confinement-dependent rock dilation on rock failure and displacement near an excavation boundary. Int J Rock Mech Min Sci, 47: 723-738.

Appendix A

Three dimensional back analysis using ABAQUS

Commercial numerical software, while providing user convenience, can implement limitations that the user may not be aware of. This is particularly true for constitutive models. In order to evaluate the results obtained by FLAC3D, the analyses were repeated using the FEM code ABAQUS. The explicit integration scheme along with the Mohr-Coulomb strain softening behavior was adopted. Linear tetrahedral elements were used in the modeling. The shaft periphery was discretized by 64 elements to get the accuracy 98% for elastic solutions as for the FLAC3D models. The excavation stages were similar to those modelled by FLAC3D and the mechanical parameters were identical to those given in Table 3.3 for model II.

Fig. A.1 shows the displacement profiles and the contour of equivalent plastic strains. In comparison with the results obtained from the FLAC3D model II, the displacements at the reference head obtained from ABAQUS were 1.0-2.8 mm higher. Significant discrepancies were observed for the radial extent of plastic zone where ABAQUS predicts 3.5-4.2 m while FLAC3D gives 2.2-2.8 m. It worth mentioning that the displacements were found to be mesh dependent so that using a courser mesh could result in lower displacements more similar to those obtained from FLAC3D model II. The extent of plastic zone, however, was not significantly mesh dependent.
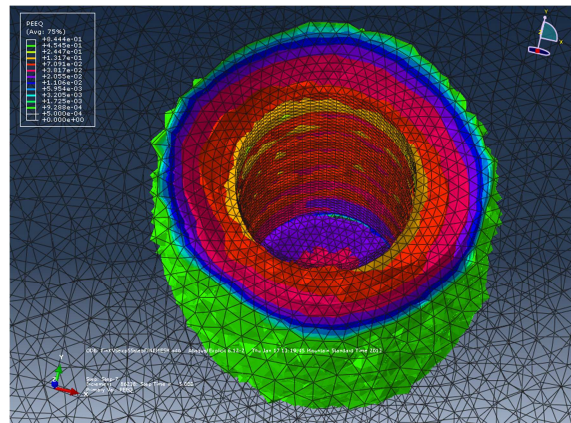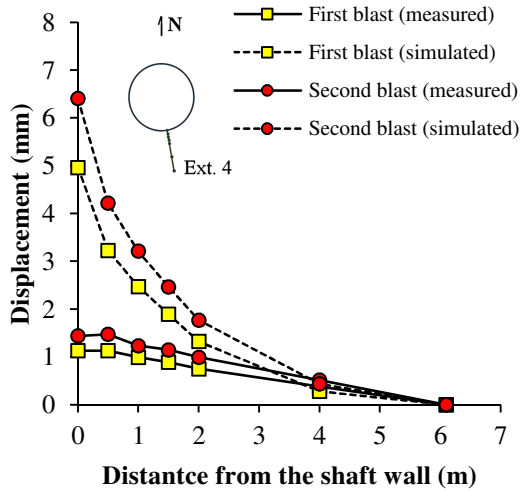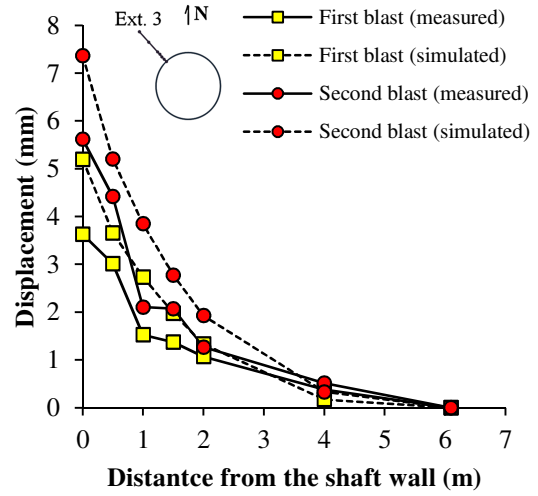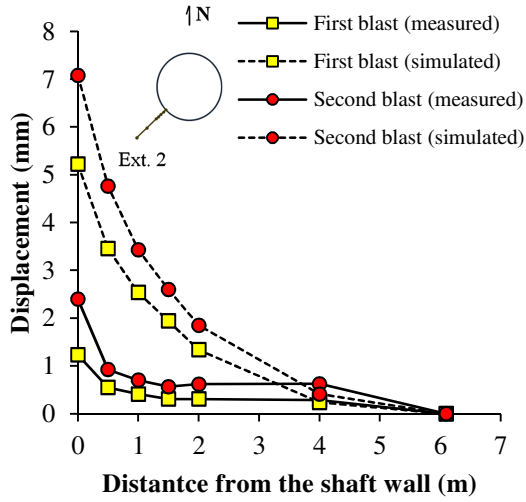
Fig.A.1 Displacement profiles and plastic strains for the ABAQUS model

Appendix B

Volumetric strain curves for the CWFS model

While several complex dilation models have been proposed in the literature to specify the variation of dilation angle with plastic strain and confining stress, simple dilation models are more practical and sufficiently accurate for practical estimation of plastic zone around excavations. A constant dilation angle of 30° was used in this study. Fig. B.1 shows the experimental and simulated axial stress-volumetric strain curves. It can be observed that the model underestimates post-peak dilation of Lac du Bonnet granite especially at lower confining stresses. It is not surprising as failure planes develop inside the laboratory samples leading to the collapse of the specimen and volumetric expansions too large to be captured by any continuum model. Hence, the proposed CWFS model is mostly useful for estimating the extent of failure zone around excavations and may underestimate the displacements inside the failure zone where slabs and pieces of rock are detached from the rock mass.
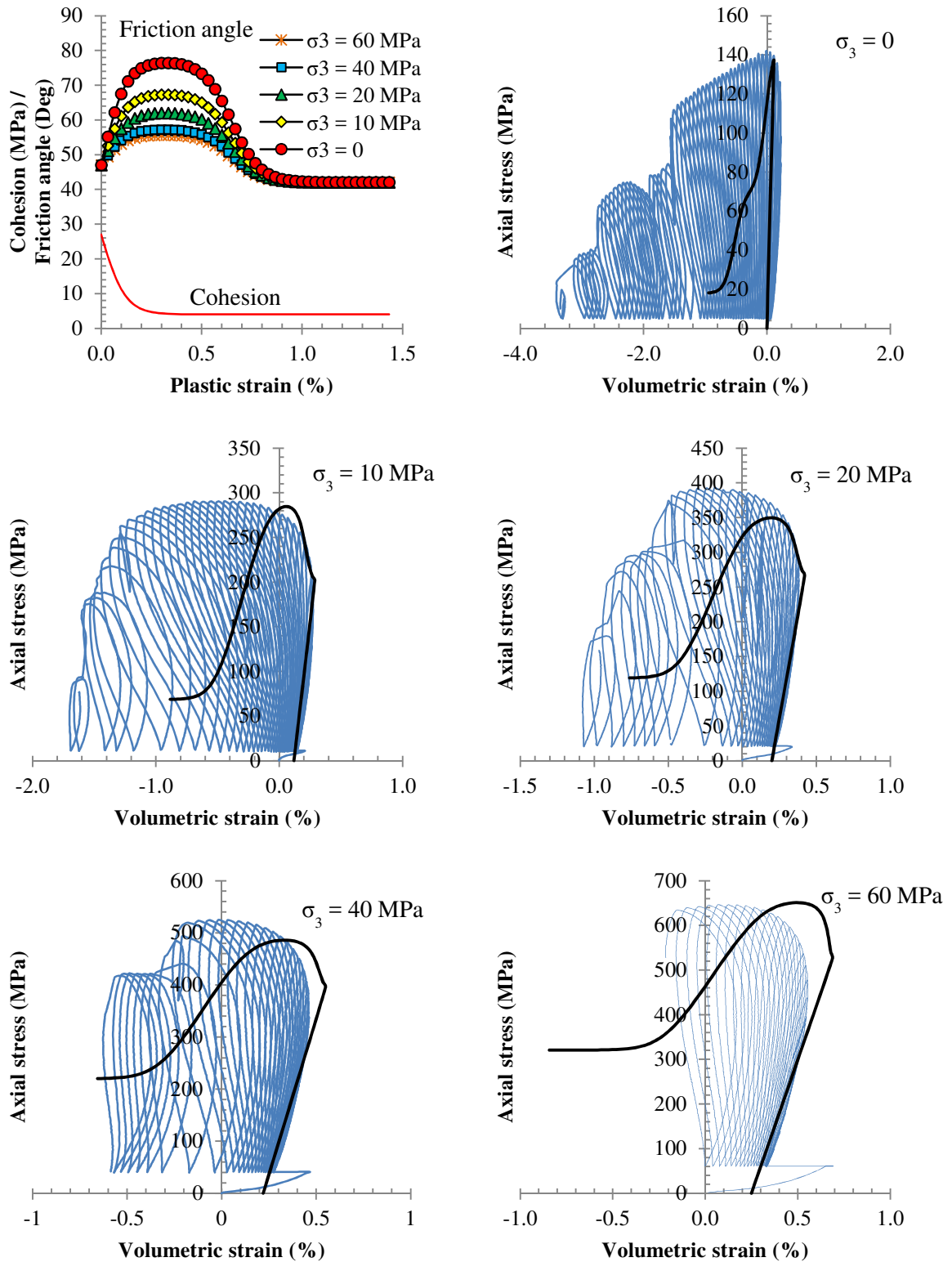
Fig.B.1 Cohesion degradation and friction mobilization in the proposed model and comparison of experimental (fine line) and simulated (bold line) axial stress- volumetric strain curves